Politecnico di Torino

ScuDo
Scuola di Dottorato ~ Doctoral School
WHAT YOU ARE, TAKES YOU FAR

Doctoral Dissertation
Doctoral Program in Physics (37^{th}cycle)

Integration of Photovoltaic Systems and Electrochemical Technologies Toward Carbon Neutrality

Experimental and Modeling Study

By

Matteo Agliuzza

******

Supervisor(s):
Prof. F.C. Pirri, Supervisor
Dr. A. Sacco, Co-Supervisor

Doctoral Examination Committee:
Prof. Francesca Toma, Referee, Helmholtz-Zentrum Hereon
Prof. Deepak Pant, Referee, Flemish Institute for Technological Research
Prof. Giancarlo Cicero, Polytechnic University of Turin
Dr. Nicolò Santi Vasile, Polytechnic University of Turin
Dr. Marco Etzi Coller Pascuzzi, Italian Institute of Technology

Politecnico di Torino
2025

Declaration

The doctoral thesis was prepared upon completion of the PhD programme funded by the PON REACT-EU 2014-2020 initiative-Action IV.4 “Doctorates and Research Contracts on Innovation Themes” and Action IV.5 “Doctorates on Green Themes”- pursuant to Ministerial Decree No. 1061 of 10 August 2021.

I hereby declare that, the contents and organization of this dissertation constitute my own original work and does not compromise in any way the rights of third parties, including those relating to the security of personal data.

Matteo Agliuzza
2025

* This dissertation is presented in partial fulfillment of the requirements for **Ph.D. degree** in the Graduate School of Politecnico di Torino (ScuDo).

Chi sa fare, sa capire.

Acknowledgements

Everyone in my life has helped me shaping who I am, giving me the strength to move forward throughout all the difficulties… and occasionally giving me the patience to finally finish this thesis.

To my family,
my closest friends,
my mentors,
to the places I hold dear,

I dedicate this thesis
-with gratitude, admiration, and a bit of love-
to all of you.

Abstract

Addressing climate change requires innovative decarbonization approaches, as rising CO_2 levels drive global warming, impacting food security, water availability, and ecosystem stability. Among the promising solutions, electrochemical CO_2 conversion has gained attention for its potential to produce value-added products in a safe and scalable way, thanks to its mild operational conditions: if the process is further powered by renewable energy sources, the system is completely sustainable. In this framwork, the present work investigates the solar-driven CO_2 reduction, both optimizing the experimental setup and developing a suitable mathematical model for the device. The model investigates the cell performance by varying parameters such as applied voltage, electrolyte flow rate, and reactor size, enabling prediction and optimization of critical operational conditions. Additionally, the chemical environment at the electrode surfaces, including species concentration and pH gradients within the diffusive boundary layers, can be analyzed. This work also integrates the electrochemical setup with Dye-Sensitized Solar Cells (DSSCs) to simulate operation under solar irradiance, exploring a sustainable energy source for CO_2 reduction. By offering insights into performance across conditions and guiding the scaling-up process, this thesis offers powerful tools for advancing CO_2 electroreduction technology and its integration into broader renewable energy systems, both in experimental and modeling point of views.

.

Contents

List of Figures

List of Tables

Chapter 1

Introduction

1.1 Content and Motivation

The growing concentration of carbon dioxide (CO_2) in the atmosphere, primarily due to anthropogenic activities, has emerged as one of the most pressing environmental challenges of the 21st century. As a potent greenhouse gas, CO_2 contributes significantly to global warming and climate change, necessitating urgent measures to mitigate its impact [1]. CO_2 is a stable molecule with an average residence time in atmosphere of 5-6 years, and its radiative forcing of 1.66 $\frac{W}{m^2}$ (*i.e*, a parameter which quantifies the instantaneous greenhouse effect of a substance) is the highest among all the compounds present in atmosphere [2].
CO_2 emission is primarily associated to the combustion of fossil fuels (which currently fulfills the 80% of the worldwide energy demand), heat generation and electricity [3]. Growing demand in energy market speeds up the global energy consumption, leading to an increasing trend of the CO_2 concentration in air: in the last 3 years, in fact, its presence in atmosphere has grown from 413.39 ppm in 2020 up to 418.96 ppm in January 2022. In summary, the anthropogenic carbon emissions are changing the carbon-cycle balance of release/absorption from vegetation, lands and oceans (Fig. 1.1), leading to a positive net balance and therefore drastic greenhouse effects.
In recent years, numerous policies and international agreements have been introduced to address the pressing challenge of global warming. A pivotal moment in this effort was the 2015 United Nations Climate Change Conference (COP21), where the landmark Paris Agreement was adopted. This accord aimed to limit global

temperature rise to well below 2°C above pre-industrial levels, with efforts to cap the increase at 1.5°C. Achieving this goal requires substantial reductions in greenhouse gas emissions and a global commitment to sustainable practices.
In 2020, the European Union took a step forward with the introduction of the European Green Deal. This policy framework outlined an ambitious target to reduce greenhouse gas emissions by at least 55% by 2030 compared to 1990 levels. The Green Deal not only addresses climate change but also promotes economic growth through a transition to renewable energy and a circular economy [4].
The urgency of these targets was further reinforced in 2021 during the COP26 summit held in Glasgow. At this event, global leaders revisited and strengthened their commitments to combat climate change. The focus shifted more decisively towards limiting the temperature increase to 1.5°C, recognizing the catastrophic consequences of surpassing this threshold. This reaffirmation emphasized the need for accelerated action and international collaboration to meet the objectives set by the Paris Agreement [5].

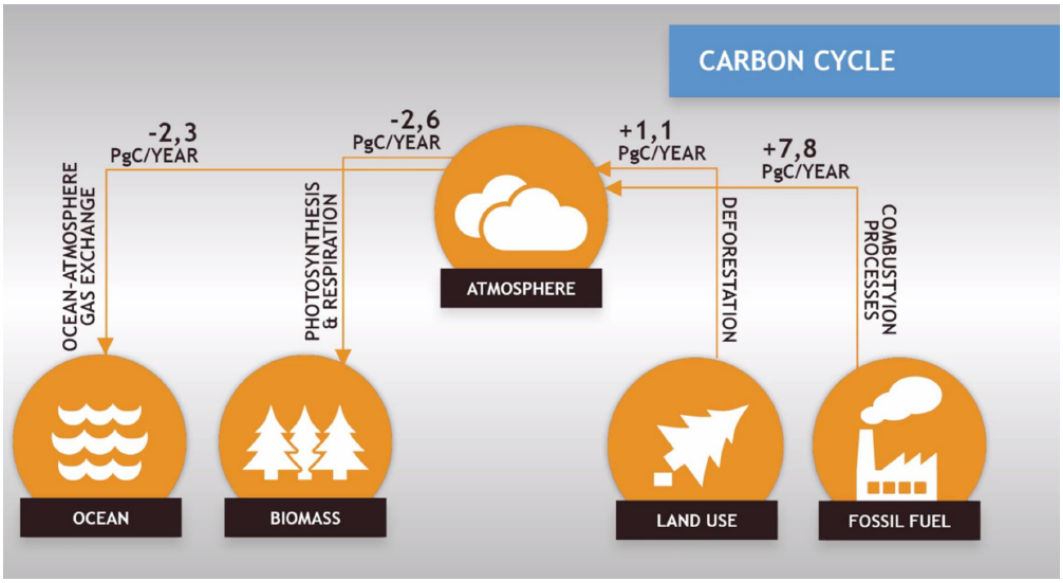

Fig. 1.1 Human interference with planetary carbon-cycle balance. The net balance due to combustion processes is +4 PgC (Petagrams of carbon) released in atmosphere per year.

In order to contain the irreversible damages to the environment, it is important to focus the attention and research on carbon recycling techniques which allow to lower the net carbon emissions with sustainable and green processes. For this purpose, three

scenarios have been proposed for the next 30 years (Fig. 1.2a): business-as-usual, rapid-transition, and net-zero [6].

- The business as usual is the worst case scenario, in which the same policies of the past years will be applied to technologies and energy-use preferences: in this possible scenario, it is expected that the carbon emission would be reduced less that 10% of the actual values.
- In the rapid transition case it has been simulated a system in which efforts have been made, such as increase of carbon prices/taxes, sponsorship of research initiatives for CO_2 recycling and investment in renewable energies (Fig. 1.2b). In this case, it can be expected a decrease of 70% in carbon emissions by 2050.
- The net-zero transition expectation is the best case, in which the rapid-transition policies are strengthened and made more efficient. Following this possibile trend, global CO_2 emissions decrease by 90% by 2050. This is also the scenario which foresees the highest demand of renewable sources.

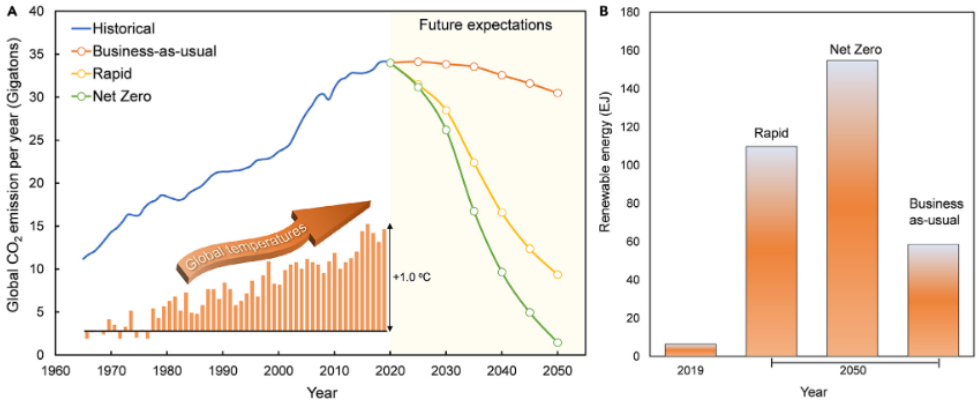

Fig. 1.2 Future expectations of global carbon dioxide emissions (a), and increase of renewable energy demand for each possible scenario (b). Reprinted with permissions from [6].

Among the various strategies under investigation, the electrochemical reduction of CO_2 (eCO_2RR) offers a promising pathway to convert this waste product into value-added chemicals and fuels, thereby addressing both environmental and energy challenges [7–9]. Electrochemical CO_2 conversion stands out among various CO_2 utilization technologies due to its energy efficiency, scalability, and direct integration with renewable energy sources. It is important to distinguish between CO_2 capture

(i.e., the extraction of CO_2 from industrial or atmospheric sources) and CO_2 conversion, which transforms the captured CO_2 into valuable chemicals and fuels.
Several technologies have already reached industrial scale, though they differ in their approach, operating conditions, and working principles. For instance, thermochemical methods [10] use high temperatures and pressures along with catalysts to drive reactions (similar to Fischer-Tropsch processes) that convert CO_2 into syngas or hydrocarbons, making them robust but energy-intensive. Photocatalytic conversion [11–13] employs semiconductor materials that absorb sunlight to generate electron-hole pairs, which then drive the reduction of CO_2; however, this method often suffers from low efficiency and selectivity, which hinders scalability at industrial level. Biological conversion [14] uses microorganisms or enzymes under ambient conditions to selectively convert CO_2 into organic compounds, though the process is slower and more complex to maintain at a large scale. Mineralization [15] involves the chemical reaction of CO_2 with alkaline minerals to form stable carbonates, effectively sequestering CO_2 without producing value-added products. Plasma-assisted technologies [16, 17] utilize ionized gases to generate reactive species that interact with CO_2, enabling rapid conversion; however, this approach is generally more energy-intensive and less selective than electrochemical processes. Electrochemical conversion, by contrast, operates under mild conditions where CO_2 is reduced at the electrode surface by transferring electrons to form chemicals and fuels, offering precise control over product distribution. These advantages position eCO_2RR as a versatile and sustainable solution for the utilization of CO_2 in a circular economy.
To drive the electrochemical CO_2 reduction efficiently and sustainably, the integration of renewable energy sources into electrochemical systems is essential. This ensures that the process remains environmentally viable by minimizing reliance on fossil-derived electricity, reducing the overall carbon footprint, and enhancing energy efficiency. Furthermore, coupling renewable energy with electrochemical CO_2 conversion can facilitate continuous and cost-effective operation, making the technology more scalable and practical for industrial applications. In this context, dye-sensitized solar cells (DSSC) have garnered significant attention as potential power sources for photoelectrochemical (PEC) and photovoltaic-electrochemical (PV-EC) systems. DSSCs combine cost-effectiveness, ease of fabrication, and adaptability to a wide range of light conditions, making them suitable for coupling with eCO_2RR devices. However, challenges related to the energy matching, stability, and overall efficiency of such integrated systems remain to be addressed.

1.2 Thesis objective

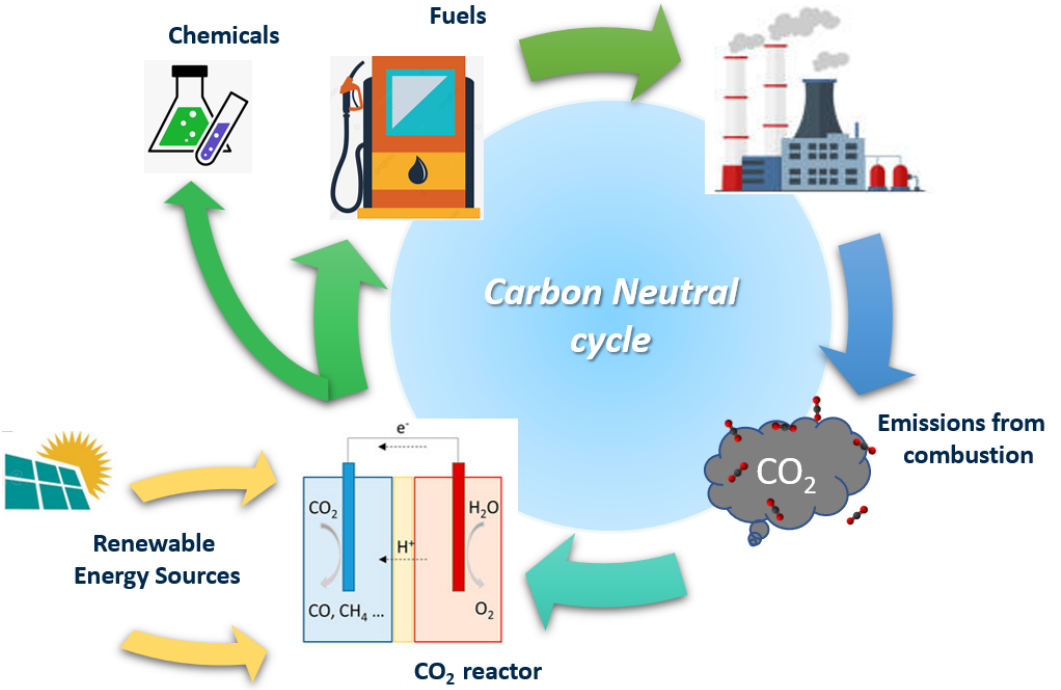

Fig. 1.3 Circular economy scheme for the Carbon Cycle in atmosphere, through solar-driven carbon dioxide reduction.

The term "Carbon Neutrality" relates to a state in which the CO_2 emissions in a system is set to zero. Although at present avoiding the use of Carbon is nearly impossible for energy-intensive industries, the best solution for decarbonization is the conversion of the CO_2 into valuable molecules for chemical or energy applications, such as: CO (carbon monoxide) for industrial fuels, CH_4 (methane) as refrigerated liquid or fuel for ovens/automobiles, CH_3OH (methanol), HCOOH (formic acid) and so on. The main implication concerns a step forward towards a circular economy, in which it can be minimized the creation of waste, pollution and carbon emissions typical of a linear economy system. In this context, the primary goal of this thesis is to explore the integration between DSSCs and an electrochemical cell for CO_2 conversion, in the field of solar-driven CO_2 reduction.
Among the various products derived from the eCO_2RR, techno-economic analyses have identified CO as the most profitable option [18, 19]. This is primarily because CO can be efficiently produced at relatively low overpotentials through a straightforward two-electron reduction pathway. Its significance in the chemical industry

is unparalleled, as CO serves as a highly versatile C_1-building block with a broad range of applications [20]. Furthermore, when combined with hydrogen (H_2), it forms synthesis gas, or syngas. Syngas is a critical feedstock for several large-scale industrial processes, including the Fischer-Tropsch synthesis of hydrocarbons [21], or it can be utilized directly in internal combustion engines as a fuel [22]. In this context, while the hydrogen evolution reaction (HER) often competes with eCO_2RR in water-based electrolytes, the simultaneous operation of both reactions can actually be beneficial. By coupling eCO_2RR with HER, it is possible to generate syngas with a tunable CO-to-H_2 ratio, thereby expanding its industrial applicability. This synergistic approach underscores the potential of electrochemical CO_2 reduction to CO as a sustainable and economically viable pathway for addressing both chemical production and carbon management challenges.

In this framework, the present work involves a dual approach: (1) experimental investigation of the performance of DSSCs and the electrochemical cell and (2) the development of mathematical models to describe and optimize the operation of the individual components and the integrated PV-EC system.

This thesis is structured to systematically address these objectives, starting with a review of the fundamental principles and state of the art in the field. It then details the experimental methods and materials employed, followed by the development and validation of a comprehensive mathematical model. The results and their implications for the design and operation of efficient, scalable PV-EC systems are discussed in detail, culminating in recommendations for future research directions. A part related to the integration of PV with bicarbonate electrolyzers is added as well, thanks to the collaboration with the work of a previous thesist, in order to address the possibility to create a system that is capable of converting captured CO_2 with solar energy.

Through this work, it is hoped to contribute to the advancement of sustainable technologies for CO_2 utilization and renewable energy integration, providing a foundation for further innovation in the field.

Chapter 2

eCO_2RR: Fundamentals, Solar Driven Conversion and Numerical Modeling

This chapter provides a comprehensive overview regarding the field of eCO_2RR. In section 2.1, it is introduced the electrochemical CO_2 reduction reaction, detailing the key parameters and components such as catalysts, electrolytes, anodes, membranes, and overall cell design. Section 2.2 focuses on solar-driven CO_2 conversion, discussing the coupling of solar cell technology with CO_2 reduction processes and reviewing the state-of-the-art in this field. Finally, in section 2.3, it is examined the numerical modeling approaches used to simulate and optimize CO_2 reduction, offering insights into recent advancements and emerging trends. Together, these sections outline an interdisciplinary framework that drives innovation in CO_2 reduction technologies. Part of the review shown in this chapter (specifically, in Section 2.2) has been previously published [97].

2.1 Electrochemical CO_2 Reduction Reaction Overview

Generally, the eCO_2RR mechanism involves a Proton-Coupled Electron multi-Transfer (PCET, Eq. 2.1),where a multi-electron transfer occurs between the electrode's surface and the CO_2 molecules, thus reducing them. In particular, H^+ are provided by water oxidation at the anode by means of the Oxygen Evolution Reaction

(OER, Eq. 2.2), and are transferred to the cathode's side through an ion-exchange membrane. At the cathode, Hydrogen Evolution Reaction (Eq. 2.3) occurs, which is a competitive reaction for which protons and electrons recombine to produce H_2.

$$CO_2 + nH^+ + ne^- \rightarrow Product + H_2O \tag{2.1}$$

$$2H_2O \rightarrow O_2 + 4H^+ + 4e^- \tag{2.2}$$

$$2H^+ + 2e^- \rightarrow H_2 \tag{2.3}$$

As shown in Table 2.1, which lists the main products obtainable from CO_2 reduction, each reaction is accompanied by a standard electrode potential (E^0) [23–25]. While it provides insights into the thermodynamic feasibility of a reaction, the actual product distribution in CO_2 reduction is governed by a complex interplay of kinetics, catalyst properties, and reaction conditions. Optimizing these factors is crucial for steering the reaction toward the desired products.

Table 2.1 Main aqueous and gaseous products obtainable from the eCO$_2$RR with theoretical electrochemical potentials vs. Reversible Hydrogen Electrode (RHE), at 25 °C, pH = 7, 1 atm and 1.0 M concentration of other solutes.

Reaction	**E^0 (V vs. RHE)**	**Product Name**
$CO_2 + 2H^+ + 2e^- \rightarrow CO_{(g)} + H_2O$	-0.10	carbon monoxide
$CO_2 + 2H^+ + 2e^- \rightarrow HCOOH_{(aq)}$	-0.12	formic acid
$CO_2 + 6H^+ + 6e^- \rightarrow CH_3OH_{(aq)} + H_2O$	0.03	methanol
$CO_2 + 8H^+ + 8e^- \rightarrow CH_{4(g)} + 2H_2O$	0.17	methane
$2CO_2 + 8H^+ + 8e^- \rightarrow CH_3COOH_{(aq)} + 2H_2O$	0.11	acetic acid
$2CO_2 + 12H^+ + 12e^- \rightarrow C_2H_{4(g)} + 4H_2O$	0.08	ethylene
$2CO_2 + 12H^+ + 12e^- \rightarrow C_2H_5OH_{(g)} + 3H_2O$	0.09	ethanol
$2CO_2 + 14H^+ + 14e^- \rightarrow C_2H_{6(g)} + 4H_2O$	0.14	ethane
$3CO_2 + 18H^+ + 10e^- \rightarrow C_3H_7OH_{(aq)}$	0.10	propanol

The reduction of CO_2 to CO, for instance, involves a relatively simple two-electron transfer process, whereas forming hydrocarbons or alcohols requires multiple electrons and protons (e.g. 8 for methane), leading to more complex reaction pathways and intermediates. Multi-carbon products also involve C-C coupling, which presents a high kinetic barrier, and the stabilization of key intermediates such as CHO, COH,

or C_2 species, which may not be favored on many catalyst surfaces. In the following sections, a general description of the main factors that influence the CO_2RR is reported.

2.1.1 Parameters of interest

The important parameters for the characterization of the eCO_2RR performance are now highlighted. This facilitates a fair comparison between the various devices and systems proposed in the literature, while also providing a quantitative evaluation of their performance.

Current Density (J_{tot}) is defined as total current (I_{tot}) flowing over the cathode's surface area (S):

$$J_{tot} = \frac{I_{tot}}{S} \tag{2.4}$$

It is one of the most important figures of merit of an electrochemical cell, since it is directly proportional to the eCO_2RR rate: in other words, it is a direct evaluation of the number of electrons involved in the chemical reaction. The partial current density can also be defined, which is the current density related to a particular product reaction rate: it gives important reaction kinetics and mechanistic insights, along with hints about catalyst selectivity and goodness of the reaction environment (Fig. 2.1).
The research pushes towards higher current density for economical perspectives as well: higher J (typically above 200 - 300 mA/cm^2) leads to lower production costs, higher profits and higher possibilities for industrial applications [27].

Faradaic Efficiency (FE) is a key parameter that quantifies how effectively the electric charge is utilized in driving a specific electrochemical reaction, such as the production of carbon monoxide: in particular, it represents the proportion of the total electric charge that directly contributes to the formation of the desired product. Mathematically, FE is expressed as the ratio of the charge used in product formation to the total charge passing through the electrochemical system:

$$FE = \frac{\chi nF}{Q} \tag{2.5}$$

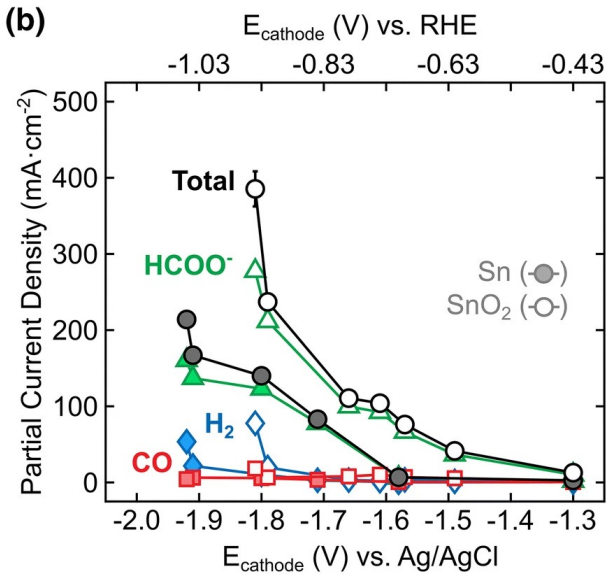

Fig. 2.1 Example of partial current density plotted against the iR-corrected cathodic potential for both Sn and SnO_2 catalysts. Reproduced with permission from Springer Nature [26].

where χ denotes the number of moles of the target product, n represents the number of electrons required to produce one mole of the product, F is the Faraday constant (approximately 96,485 C/mol) and Q is the total charge that flows through the electrodes. The Faradaic Efficiency is crucial for assessing the selectivity of the catalyst, which contributes to the performance of the electrochemical device. It provides insight into how well the system favors the formation of the desired product over competing side reactions. A high FE indicates that the majority of the electrical energy is being used for the intended electrochemical conversion, making it a valuable metric for optimizing reaction conditions and evaluating device performance. From the FE, it is possible to obtain the partial current density j_{par}:

$$j_{par} = J_{tot} \times FE \tag{2.6}$$

Overpotential (η) is defined as the potential that must be added to the thermodynamic requirement, in order for a reaction to occur at a certain rate. It depends on the type of cell design and operational conditions, and it can be calculated by looking at the experimental potential required to drive a reaction at a given current density. The total overpotential is composed by three main terms related to different reaction

steps [28]: mass-transfer overpotential (η_{mt}), charge-transfer overpotential (η_{ct}) and reaction overpotential (η_{rxn}). The η_{mt}, also referred as concentration overpotential [29], is related to the mass transfer limitations of dissolved CO_2 from the bulk of the electrolyte to the electrode and products from the catalyst surface to the bulk. In aqueous media, in fact, the solubility of CO_2 is relatively low at standard conditions, leading to low diffusion rates of reactants. The best strategies to avoid this problem are the employments of non-aqueous solvents, lower temperatures and higher pressures, or by exploiting gas-diffusion electrodes (GDE) in flow cell configuration: first demonstrated by Mahmood et al. [30], in fact, GDEs improve the transport of gaseous CO_2 molecules to the electrode thanks to lower diffusion lengths, achieving higher current densities. The charge-transfer potential η_{ct} (also referred as activation overpotential) is related to the activation energy barrier for the transfer of electrons at the electrode-electrolyte interface, while the reaction overpotential η_{rxn} describes the activation overpotential associated to previous reactions. In addition, the ohmic potential drop related to the solution should not be considered as an overpotential, since it is not dependent on the electrode reaction [28].

2.1.2 eCO_2RR Catalyst

The eCO_2RR is significantly enhanced by the presence of a catalyst, which serves as the cornerstone for determining the selectivity and efficiency of the final product. Catalysts play a dual role in this process: they lower the activation energy barrier required for CO_2 reduction and provide active sites where specific reaction pathways can be favored. The catalytic activity toward a particular product is governed by two key factors: the binding strength of the catalyst to critical intermediates and its ability to adsorb CO_2 molecules onto vacant coordination sites on the reduced catalyst surface [31]. These properties are influenced by the material composition, electronic structure, and surface morphology of the catalyst.
Extensive research in the literature has demonstrated that the formation of carbon-bound intermediates is a pivotal step in determining the reaction pathway and the ultimate product distribution. For instance, in the conversion of CO_2 to CO, the reaction pathway is largely dictated by the initial formation of hydrogenated intermediates such as *COOH or *OCHO [32]. The binding energies of these intermediates must be carefully balanced: they should be strong enough to stabilize the intermediates but not so strong as to inhibit their further transformation into the desired

products.

To gain deeper insights into these complex processes, various advanced in-situ and operando techniques have been developed and widely employed. Techniques such as surface-enhanced infrared absorption spectroscopy (SEIRAS), Raman spectroscopy, X-ray absorption spectroscopy (XAS), and scanning tunneling microscopy (STM) have provided valuable information about the dynamic behavior of catalyst surfaces under operating conditions. These methods allow researchers to identify intermediate species, monitor their evolution, and elucidate the sequence of elementary steps in the reaction mechanism [33]. Such insights are instrumental in guiding the design of catalysts with improved selectivity, activity, and durability.

Furthermore, the nature of the catalyst (whether it is a metal, alloy, molecular complex, or heterogeneous material) plays a critical role in shaping the reaction outcomes. For example, metals such as Au [34], Ag [35] and Sn [36] are highly selective for CO production due to their optimal binding energy with *COOH intermediates, while Cu is unique in its ability to produce hydrocarbons and alcohols through multi-step reduction pathways by stabilizing intermediates needed for C-H and C-C bonding [37]. Additionally, Metal alloys have emerged as a versatile class of catalysts, offering enhanced performance through the synergistic interaction of multiple metals. Among the most studied classes, Sn-based alloys [38, 39] and Cu-based alloys [40, 41] emerge, for improvements in both stability of the catalyst and suppression of HER.

On the other hand, molecular catalysts and metal-organic frameworks (MOFs) offer tunable active sites and structural flexibility, opening avenues for precise control over the reaction environment. They consist of metal nodes coordinated with organic linkers, creating porous, crystalline frameworks that can be engineered to optimize CO_2 adsorption and activation, with low amounts of metals exploited. For further details, recent reviews are available for the current status of MOFs [42, 43].

The role of the catalyst extends beyond its surface properties; the local reaction environment, including the electrolyte composition [44], pH [45–47], and eventual poisoning [48–50], also interacts with the catalyst to influence reaction kinetics and selectivity. Designing catalysts that can operate efficiently under realistic and scalable conditions remains a key challenge in advancing eCO$_2$RR technologies.

2.1.3 Electrolyte

The choice of electrolyte plays a critical role in the electrochemical reduction of carbon dioxide, significantly influencing the efficiency, selectivity, and stability of the reaction. Electrolytes, in fact, serve multiple functions in CO_2 reduction systems, including facilitating ion transport, maintaining charge balance, and affecting the local chemical environment near the electrode surface [51]. They can be broadly categorized into aqueous and non-aqueous, each with its advantages and challenges.

Aqueous Electrolyte

Aqueous electrolytes are among the most commonly used, due to their high ionic conductivity, environmental friendliness and ease of handling, despite suffering from low CO_2 solubility (0.034 M at 25°C and 1 atm [52]). Due to equilibrium reactions occurring with water (more insights will be present in Chapter 4), the introduction of CO_2 in the liquid forms mainly carbonate (CO_3^{2-}) and bicarbonate ions (HCO_3^-) [53]. The solubility, and consequent anions concentration, depends mostly on the balance between pH, temperature and pressure of the electrolyte (as shown in Fig. 2.2).

It can be observed that CO_2 solubility in aqueous solutions decreases as temperature increases, primarily due to the reduced gas dissolution capacity of water at higher temperatures. As a consequence, the equilibrium concentrations of CO_3^{2-} and HCO_3^- decrease, which in turn influences the speciation of dissolved carbon species. Furthermore, the distribution of CO_2 species in solution is strongly pH-dependent. At acidic pH values (below approximately 6.3), the majority of dissolved CO_2 remains in its molecular form or as carbonic acid (H_2CO_3), with only a small fraction dissociating into bicarbonate. In the near-neutral pH range, HCO_3^- becomes the predominant species, playing a crucial role in buffering the solution. At alkaline pH values (above approximately 10.3), carbonate dominates due to the further deprotonation of bicarbonate. This shifting equilibrium is highly relevant for eCO_2RR, as bicarbonate and carbonate ions are the active species that facilitate the transport of CO_2 in solution and directly participate in the reaction mechanism [55]. The availability of these species influences the reaction kinetics, local pH stability, and overall efficiency of CO_2 conversion.

In water-based reactors, the selected electrolytes must be highly water-soluble and

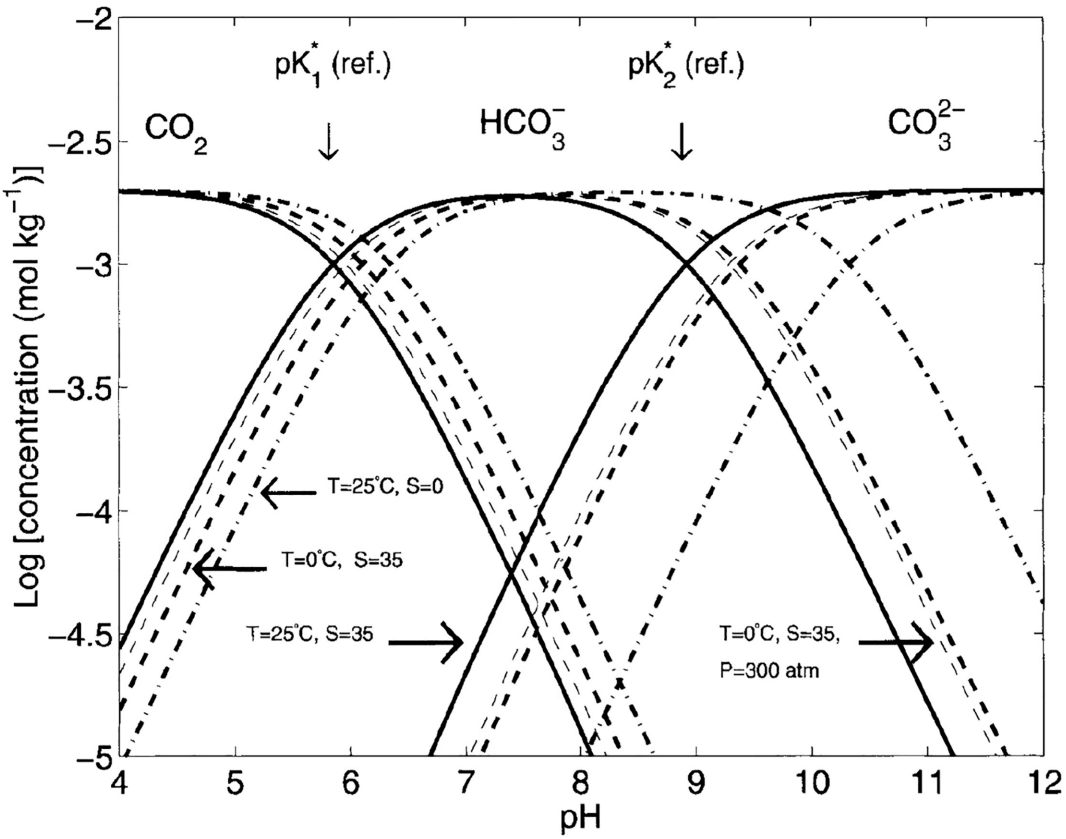

Fig. 2.2 CO_2 solubility in water as a function of pH, temperature, salinity, and pressure. Reprinted with permissions under the Creative Commons Attribution (CCA) 4.0, from [54].

stable within the applied potential range, ensuring efficient ionic transport and facilitating electrode reactions [54]. Common electrolytes include carbonates/bicarbonates (*e.g*, $KHCO_3$, $NaHCO_3$) [56] and hydroxides (*e.g*, KOH, NaOH) [57], with varying concentration. The performance dependency on the electrolyte's molarity is difficult to unravel, since it influences eCO$_2$RR by altering its intrinsic properties, which in turn affect the reaction environment. For instance, a more concentrated KOH solution raises the pH, while a higher $KHCO_3$ concentration enhances the buffer capacity. Although increasing concentration leads to higher conductivity, lower ohmic losses and higher partial current densities [58], direct consequence on the Faradaic Efficiency of the process is not straightforward: as an example, Pinto *et al.* [59] found that the HCOOH production rate was heavily influenced by electrolyte composition, while having a low impact on CO production.

Non Aqueous Electrolyte

While most of the research on the eCO_2RR is centered on aqueous media, nonaqueous electrolytes offer advantages, such as: minimizing hydrogen evolution reaction, regulating proton-assisted reduction pathways, promoting C–C bond formation for C_{2+} products [60], and enabling higher CO_2 solubility (up to 0.31 M) [61]. In nonaqueous environments, the choice of solvent plays a crucial role in determining the reaction mechanism and product distribution. For example, aprotic solvents such as Acetonitrile [62] and Dimethyl Sulfoxide [63], are frequently employed to minimize proton availability and favor pathways leading to CO and oxalate. Nevertheless, the relationship between the type of organic solvent, water content, cathode material, and cathode potential in eCO_2RR within aprotic solvents remains insufficiently explored, limiting its practical implementation [64].
Ionic liquids (ILs), namely salts in liquid phase, have also been extensively studied as electrolytes [65]. Studies have shown that ILs such as [Emim][BF_4] form stable complexes with CO_2 [66], thereby facilitating its reduction with minimal energy input. Additionally, the ILs ability to capture CO_2 molecules is useful when dealing with real flue gases, where the carbon dioxide concentration is low (from 4% up to 15%) [67]. In this framework, Sun *et al.* [68] exploited [Bmim][PF_6] IL for eCO_2RR under diluted CO_2 conditions with good performance: the ILs were impregnated into porous Ni-N-C (nickel-nitrogen-carbon) single-atom catalysts, forming a solid/liquid interface with high CO_2 concentration. However, challenges such as cost, viscosity, toxicity, and large-scale applicability must be addressed before ILs can be widely adopted in industrial settings.

2.1.4 Membrane

Membranes play a crucial role in electrochemical systems by serving three fundamental functions. First, they act as an electronic insulator between the cathode and anode, preventing direct contact and thus avoiding electrical short circuits. Second, they serve as a selective physical barrier, minimizing the crossover of species between compartments, which helps maintain the purity of reactants and products in electrochemical cells. Third, they facilitate ion transport, ensuring continuous ionic conductivity between the catholyte and anolyte to maintain charge balance and sustain electrochemical reactions [69].

A key category of membranes used in these applications is ion-exchange membranes (IEMs), which are composed of polymeric materials functionalized with immobilized ion-exchange groups. These fixed charge sites attract and transport mobile counterions through the membrane matrix, enabling selective ion movement while blocking unwanted species.
Depending on the nature of the ionic groups embedded within the membrane, IEMs are classified into three main types: cation exchange membranes (CEMs), anion exchange membranes (AEMs) and bipolar membranes (BPMs). CEMs contain negatively charged functional groups, such as sulfonates or carboxylates, which selectively allow the passage of positively charged ions (cations) like H^+, Na^+, or K^+. Conversely, AEMs possess positively charged functional groups, such as quaternary ammonium groups, facilitating the transport of anions like OH^-, Cl^-, or CO_3^{2-}. BPMs are hybrid types of membranes, containing both CEM and AEM layers. The choice between CEMs, AEMs and BPMs is dictated by the specific electrochemical process, the desired ion selectivity, and the operating pH conditions.

Cation Exchange Membranes

CEMs are a crucial component in eCO$_2$RR, where they serve to separate the anodic and cathodic compartments in both batch-type (H-cell) and flow reactors (see section 2.1.6). Their primary function is to facilitate the transport of cations while blocking anions, thereby maintaining ionic connectivity and influencing the reaction environment. This selective transport plays a significant role in controlling product distribution and overall system efficiency.
The key factor associated with CEMs is cation crossover, which affects the process selectivity. Alkali metal cations, such as K^+, have been shown to enhance CO_2 reduction by modifying the local electric field density and strengthening CO_2 adsorption [70, 71]. Additionally, although crossover is largely prevented, crossover of some neutral products (*e.g.*, methanol) remains a concern, as it leads to contamination of the anolyte and reduces selectivity [72, 73].
Membrane stability is another critical factor in determining the long-term viability of CEM-based systems. Perfluorosulfonated ionomers, such as Nafion^{tm}, are widely used due to their high proton conductivity, but they are also prone to degradation under anodic electrochemical conditions, where produced H_2 and O_2 react [74]. Other concerns are raised regarding their swelling in presence of alcohols, and toxicity

of the membranes [75]. In terms of applications, CEMs are commonly employed in H-cell reactors, where they enable high Faradaic efficiencies for CO (>97%) [76] and HCOOH (>98%) [77] production. They are also used in flow reactors, where they help minimize anionic product crossover and optimize proton transport. Recent advancements have leveraged CEMs to mediate bicarbonate conversion into electrochemically active CO_2, leading to improvements in CO production efficiency at lower full cell voltage (due to lower overpotentials for water splitting) [78] .

Anion Exchange Membranes

A key drawback of CEMs is their tendency to create acidic environments at the cathode, which enhances the unwanted HER reaction. To counter this, AEMs are often employed, as they facilitate the transport of OH^- from cathode to anode, maintaining an alkaline environment favorable for CO_2 reduction reactions. Additionally, the high pH at the anode enables the use of cost-effective, non-noble metal catalysts for the OER reaction, reducing material expenses [79].
AEMs have been utilized in both batch-type (H-cells) and flow reactors, with the latter showing greater efficiency and selectivity. However, AEM-based systems face stability issues, primarily due to anion crossover, which leads to CO_2 pumping (a process where CO_2 reacts with OH^- to form carbonate ions that migrate to the anolyte), reducing pH and overall efficiency [80, 81]. To mitigate these challenges, frequent anolyte replacement is necessary, as carbonate buildup can cause precipitation, potentially leading to cell failure. In addition to reactant crossover, AEMs could suffer from important products crossover, which may be detrimental to the FEs. For instance, negatively charged products, such as formate ($HCOO^-$), may migrate through AEMs at high current densities [82].

Bipolar Exchange Membranes

BPMs consist of a cation-exchange layer and an anion-exchange layer, which create separate pH environments on either side by facilitating water dissociation at their interface under an electric field. Their operation varies based on the applied voltage, functioning in either reverse or forward bias, each with unique benefits and limitations [83], as shown in Fig. 2.3. In reverse bias, water splitting produces protons and hydroxide ions, which are essential for ionic conductivity, though significant

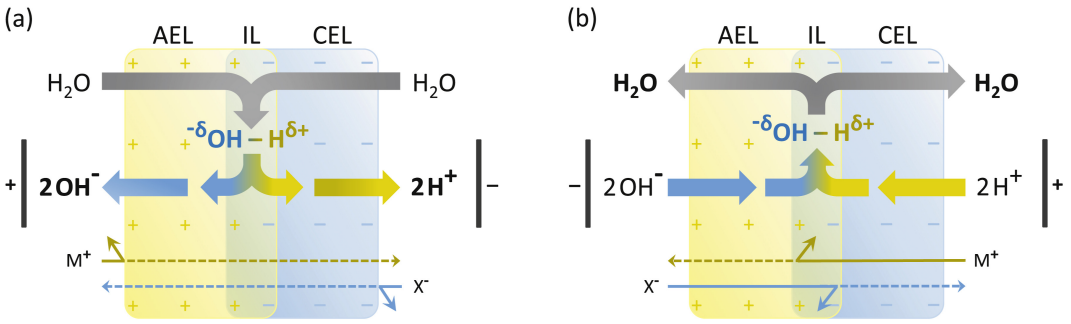

Fig. 2.3 Diagram illustrating the operational mechanism of a bipolar membrane. In reverse bias (a), the junction is initially stripped of ions, which subsequently triggers the dissociation of water into H^+ and OH^- ions. In forward bias (b), ions are drawn into the membrane, resulting in the formation of water at the bipolar interface. Reprinted with permissions under the CCA 4.0, from [85].

overpotentials can arise at high current densities, requiring effective catalysts to improve efficiency. A key advantage of BPMs is their ability to restrict anionic species like bicarbonate and carbonate from crossing over, thus optimizing CO_2 capture and maintaining higher Faradaic efficiency [84]. However, in forward bias, accumulation of neutral products and CO_2 at the interface can lead to structural instability. Mechanical degradation, including delamination of the CEL and AEL, poses another challenge, especially under harsh operating conditions [85]. Despite their potential, BPMs still face hurdles like high cell voltages, parasitic hydrogen evolution, and mechanical wear. Addressing these issues through improved catalysts, optimized membrane structures, and better reactor designs is crucial for making BPMs a viable option for large-scale eCO$_2$RR applications

2.1.5 Anode

In eCO$_2$RR, the anode catalyst plays a crucial role in driving the oxidation reaction necessary to maintain charge balance in the system, usually the OER. The most commonly used anode catalysts include iridium, nickel, platinum, and nickel-based alloys [86]. Among these, iridium is the most frequently employed due to its stability, even under the near-neutral pH conditions that develop over time during prolonged electrolysis. Although iridium is not stable in highly alkaline environments, it remains effective in CO_2 electrolyzers where the anolyte gradually becomes neutral [87]. Nickel and its alloys, on the other hand, are widely utilized in alkaline conditions because of their strong activity in the OER [88]. However, they tend to dissolve in

near-neutral or acidic environments, limiting their long-term stability [89]. Platinum, despite not being among the most active OER catalysts, appears in many studies due to its robustness in laboratory-scale experiments and its resistance to degradation [90, 91].

As anticipated, the primary function of the anode catalyst is to facilitate the oxidation reaction that takes place at the anode, complementing the reduction of CO_2 at the cathode. While OER is well understood and has been extensively studied, it presents certain challenges in the context of CO_2 electrolysis. The reaction requires a high thermodynamic potential (1.23 V vs. RHE) and additional overpotential due to slow kinetics, leading to significant energy consumption [92]. Furthermore, the oxygen produced has relatively low economic value, which reduces the overall efficiency and cost-effectiveness of the system.

To overcome these limitations, researchers have explored alternative anodic reactions that require lower potentials and produce valuable byproducts. One promising approach involves the oxidation of alcohols or other organic compounds, such as glycerol, ethanol, and methanol [93]. These reactions can proceed at lower potentials compared to OER, reducing the overall energy demand of the electrolysis process. Additionally, they yield value-added products, such as formate or carboxylates, which can be used in the chemical industry.

2.1.6 Cell design

Various electrolyzer configurations exist (as illustrated in Fig. 2.4), each influencing operational conditions and electrochemical performance differently [94–96]. The single-compartment cell (Fig. 2.4a) represents the most basic design, where the anode and cathode share the same electrolyte without any separation. In contrast, the H-type cell (Fig. 2.4b) incorporates an ion exchange membrane that separates the anodic and cathodic compartments to prevent liquid-phase products from migrating between the two chambers. The flow cell (Fig. 2.4c) utilizes Gas Diffusion Layers (GDLs) to facilitate the transport of CO_2 gas to the electrode, mitigating mass transport limitations. Finally, the zero-gap cell (Fig. 2.4d) eliminates the physical distance between the catalysts (both anodic and cathodic) and the membrane, further enhancing mass transport efficiency.

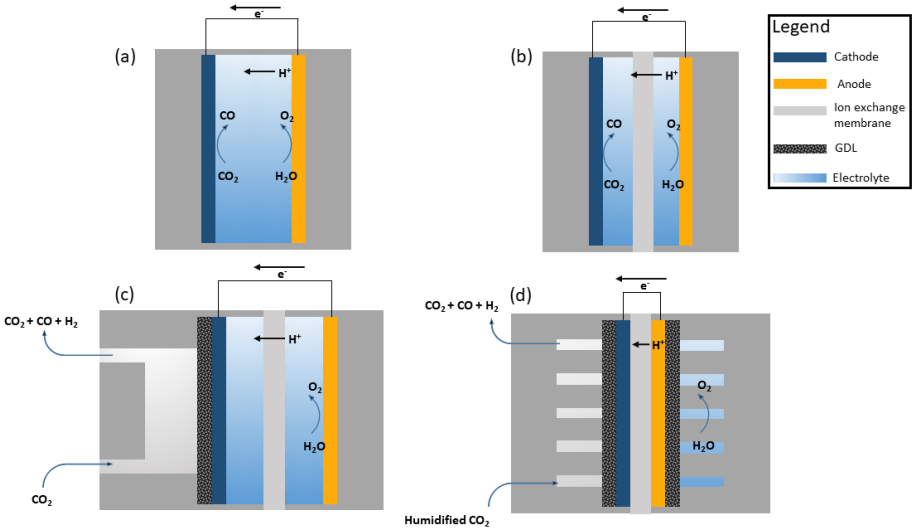

Fig. 2.4 Electrochemical reactors for CO_2 reduction: a) single cell, b) H-type cell, c) flow cell, d) zero-gap cell. Reprinted with permissions under the CCA 4.0, from [97].

Batch Cell

The batch cell is the easiest electrochemical setup for eCO$_2$RR. In these systems, both without (single cell) and with membrane (H-type cell), CO_2 is bubbled inside the water-based electrolyte, and only the molecules dissolved are reduced on the catalyst surface. Although widely used in literature to screen catalyst performance and for mechanistic studies, this type of reactor presents low current densities (below tens of mA/cm^2), due to CO_2 mass transport limitations. Furthermore, low CO_2 utilization efficiency hinders their applications at industrial scale.

Flow Cell

To overcome the mass transport limitation problems of the batch cell, flow cell systems have been developed, in which CO_2 reacts in the gaseous phase rather than being dissolved in the electrolyte: this has been made possible thanks to the GDL applied before the catalyst (as depicted in Fig. 2.5) [98].
The GDL, made of porous and hydrophobic materials like carbon paper or carbon cloth treated with polytetrafluoroethylene (PTFE) [100], allows reactant gases to diffuse towards the catalyst layer (CL) while maintaining electrical conductivity. The

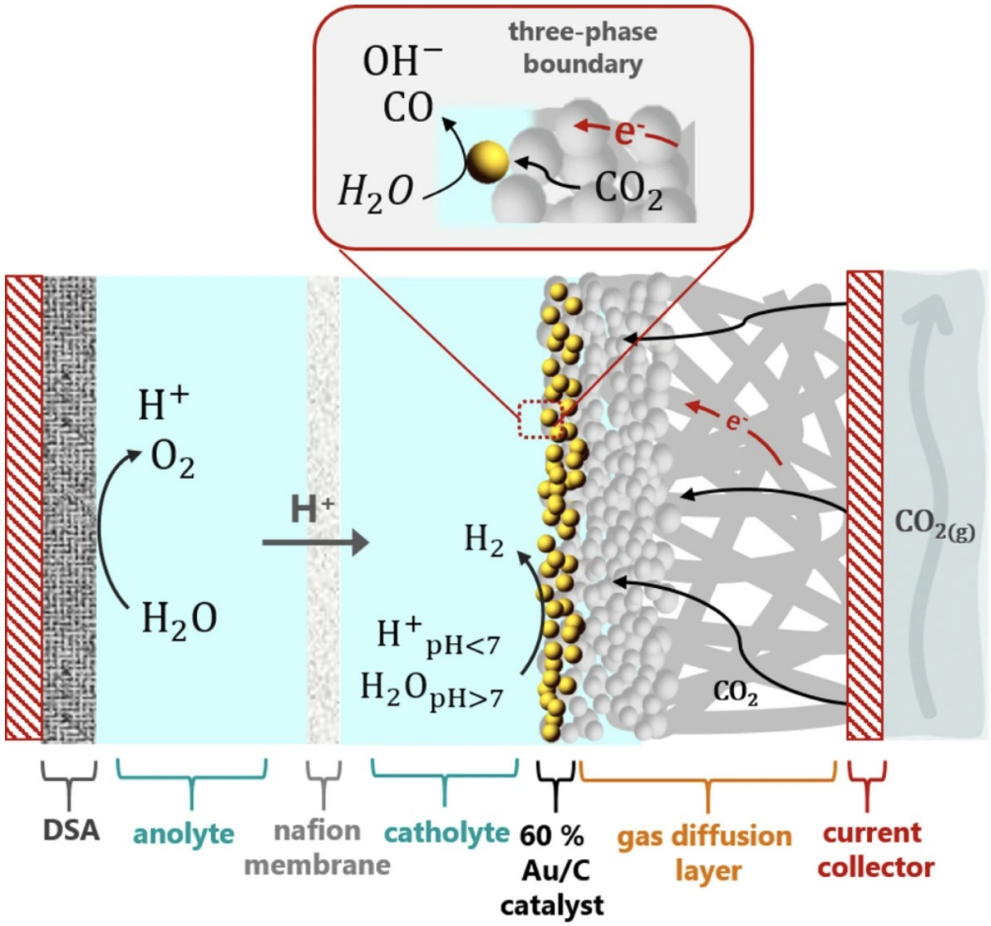

Fig. 2.5 Working principle of a GDE in flow cell reactors. Reprinted with permissions under the CCA 4.0, from [99].

CL, deposited on the GDL through methods like spray coating or ink deposition, contains electrochemically active materials such as metal nanoparticles (Ag, Cu, Pt) or carbon-supported catalysts, where the electrochemical reaction takes place. Lastly, the microporous layer, often composed of carbon black mixed with PTFE, is positioned between the GDL and catalyst layer to improve gas distribution while prevent excessive flooding. This structure enables eCO_2RR in the so-called triple-phase boundary (TPB): this interface enables the simultaneous presence of reactants (gas), charge carriers (liquid), and catalysts (solid), thus driving the electrochemical reactions efficiently. The TPB is established within the microporous structure of the catalyst layer, where carefully tuned hydrophobic and hydrophilic properties control the distribution of reactants and electrolyte. The hydrophobicity of the GDL plays a critical role in preventing excessive water ingress, while hydrophilic regions within

the CL ensure sufficient ionic contact with the electrolyte.
To optimize GDE performance, various design considerations must be addressed. The porosity and wettability of the GDL are crucial in ensuring proper gas and electrolyte transport, with an ideal balance required to prevent flooding while maintaining effective reactant delivery [101]. Additionally, the structural integrity and electrical conductivity of the GDE are key parameters that influence long-term stability and efficiency [102]. Although promising for the higher current densities, a major (and unsolved) issue in flow cells is the unintended intrusion of the liquid electrolyte into the electrode's gas channels. This flooding occurs when the electrode's initial water-repellent properties diminish, often due to phenomena like electrowetting, imbalanced pressures within the structure, and the buildup of salt deposits from reactions between CO_2 and the electrolyte [103]. As the liquid invades the porous network that is meant to ensure effective gas transport, it blocks the pathways needed for CO_2 to reach the catalytic sites, thereby reducing the efficiency of the reduction reaction. The resulting salt precipitation further exacerbates the problem by clogging the pores, ultimately leading to a decline in both the performance and the long-term stability of the system.

Zero-Gap Cell

A zero-gap cell is a key architecture for the eCO$_2$RR, offering advantages in terms of mass transport, energy efficiency, and scalability. This design eliminates the presence of a liquid electrolyte between the cathode and the anode, positioning them in direct contact with a membrane that acts as both an ion-conducting medium and a separator. The absence of a liquid electrolyte in the main reaction zone significantly reduces ohmic losses, enabling lower cell voltages and enhancing overall energy efficiency. Additionally, the direct proximity of reactants to the catalytic surfaces minimizes transport limitations and facilitates higher reaction rates, enhancing the operational current density.
In the typical setup (Fig. 2.6), a proton exchange membrane commonly serves as the electrolyte, allowing gaseous reactants such as CO_2 to be introduced without the presence of an aqueous electrolyte between the electrodes. Unlike conventional catholyte-based systems, zero-gap cells do not rely on a bulk liquid electrolyte, although the catalyst-membrane interface must still facilitate ion transport across the ion-exchange membrane. While the fundamental reactions occurring at the cathode

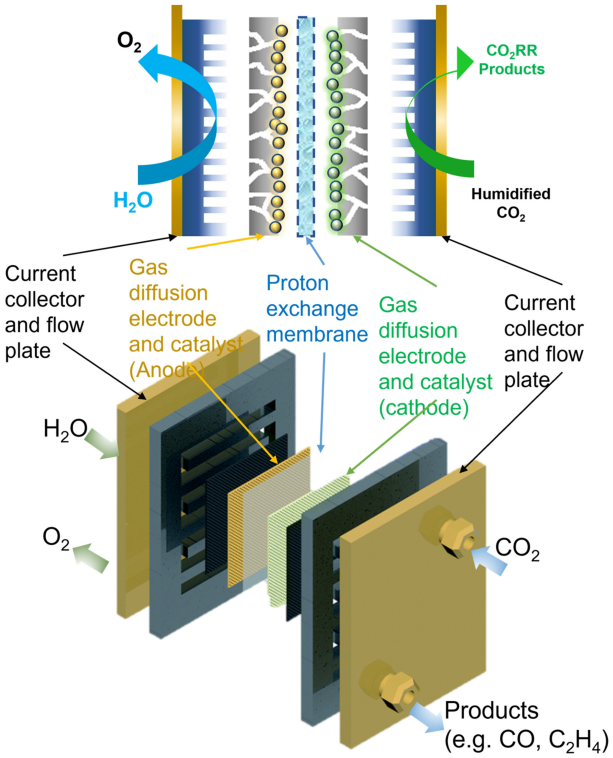

Fig. 2.6 Typical setup for a zero-gap cell. Reprinted with permissions from Elsevier [104].

and anode remain comparable to other reactor technologies, a key distinction lies in the integration of the GDE with the ion-exchange membrane, forming a solid-state catholyte. In this configuration, gas and liquid products are collected on the feed side, eliminating the need for a flowing catholyte between the CL and the ion-exchange membrane.

One of the main challenges associated with zero-gap cells is the management of water availability at the cathode. Since the reaction often requires protons for the formation of products such as CO, formate, or hydrocarbons, the hydration of the membrane and the maintenance of optimal water levels are crucial for sustained operation. Insufficient hydration can lead to increased resistance and degradation of the membrane, while excessive water can flood the gas diffusion layer, limiting CO_2 access to the catalyst. Strategies to control water balance include careful optimization of humidification conditions, modification of the catalyst layer structure, and the use of hydrophobic or hydrophilic materials within the electrode assembly [105–107]. Another critical aspect is the salt precipitation: hydroxide ions generated at the cathode, in fact, react with CO_2, forming bicarbonate and carbonate species that can

precipitate with the cations present in the electrolyte, leading to electrode blocking, membrane degradation, and performance decay [108].

2.1.7 Bicarbonate Electrolyzer

Electrochemical technologies that convert captured carbon dioxide into value-added products are central to sustainable energy and chemical strategies, and bicarbonate electrolyzers have emerged as a compelling approach by integrating CO_2 capture with *in situ* conversion [109]. Instead of feeding highly pure CO_2 gas, these cells feed aqueous bicarbonate directly to the cathode, where protonation and decomposition reactions release CO_2 at the reaction interface and enable immediate electrochemical reduction. In this case, the bicarbonate originates from an alkaline solution that simulates CO_2 capture from flue gases. This approach enables the use of bicarbonate electrolyzers to both capture and electrochemically convert CO_2, thereby eliminating the need for initial gas separation and the supply of pure CO_2.
Within the cathode compartment, protons (supplied either through a bipolar or cation-exchange membrane) react with bicarbonate or carbonate ions to form carbonic acid, which rapidly decomposes:

$$HCO_3^- + H^+ \rightarrow H_2CO_3 \rightarrow CO_2 + H_2O \tag{2.7}$$

$$2CO_3^{2-} + 4H^+ \rightarrow 2CO_2 + 2H_2O \tag{2.8}$$

This localized generation of gaseous CO_2 at the catalyst surface circumvents bulk gas handling and ensures a high concentration of reactant precisely where reduction occurs.
Immediately after release, the CO_2 undergoes electrochemical reduction on catalysts. The predominant two-electron pathway is represented by:

$$\mathrm{CO_2 + H_2O + 2}e^- \rightarrow \mathrm{CO + 2OH^-}, \tag{2.9}$$

which produces carbon monoxide and hydroxide ions. The accumulation of hydroxide ions locally basifies the solution, which can be further utilized to capture CO_2 producing bicarbonate ions:

$$OH^- + CO_2 \rightarrow HCO_3^- \tag{2.10}$$

Optimizing bicarbonate electrolyzers for CO production requires careful control of mass transport and reaction kinetics. Catalyst selection and membrane stability in alkaline conditions are critical to achieving high current densities and faradaic efficiencies. Typically, zero-gap cells are used for this application, with flow fields that bring the bicarbonate solution on the catalyst (Fig. 2.7).
By combining CO_2 capture and electrochemical conversion into a single cell, bicarbonate electrolyzers eliminate separate regeneration steps, reduce energy demands, and produce pure CO suitable for downstream synthesis of fuels and chemicals.

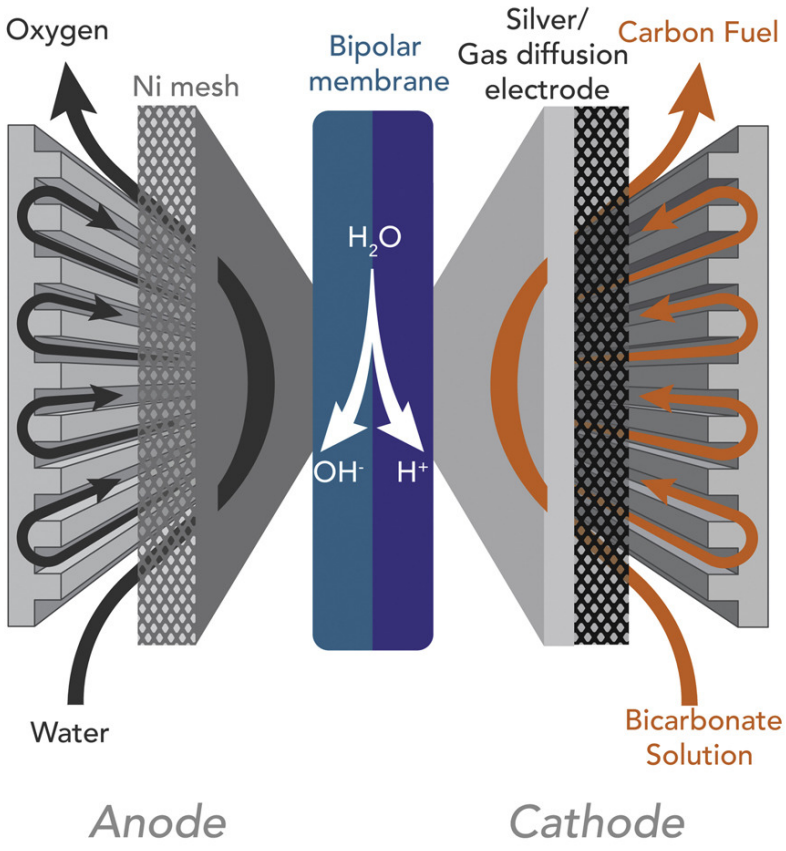

Fig. 2.7 Schematic representation of a typical bicarbonate electrolyzer, in MEA configuration. Reprinted with permissions from Springer nature [110].

2.2 PV-EC Devices

2.2.1 Coupling Mechanism

Photovoltaic-Electrochemical cells (PV-ECs) are peculiar systems that combine photovoltaic (PV) modules with electrochemical (EC) cells designed for CO_2 reduction (Fig. 2.8a). The high technological maturity of both PV and EC components [111] makes these hybrid devices promising for large-scale deployment, ensuring long-term stability and enhanced control over the efficiency of individual elements. However, a critical challenge in PV-EC integration lies in achieving an optimal electrical operating point. To prevent energy losses and suboptimal performance, the current and voltage characteristics of the PV and EC systems must be precisely matched.

This alignment is accomplished by designing the components so that their current–voltage (I-V) characteristics intersect at the desired operating point (Fig. 2.8b). Several parameters influence this matching: for the PV module, the number and configuration of solar cells determine the output voltage and current, while for the EC module, key factors include the electrode surface area, the choice of catalyst, the volume of the reaction cell, and the concentration of the electrolyte. By carefully tuning these variables, the system can be engineered to operate efficiently.

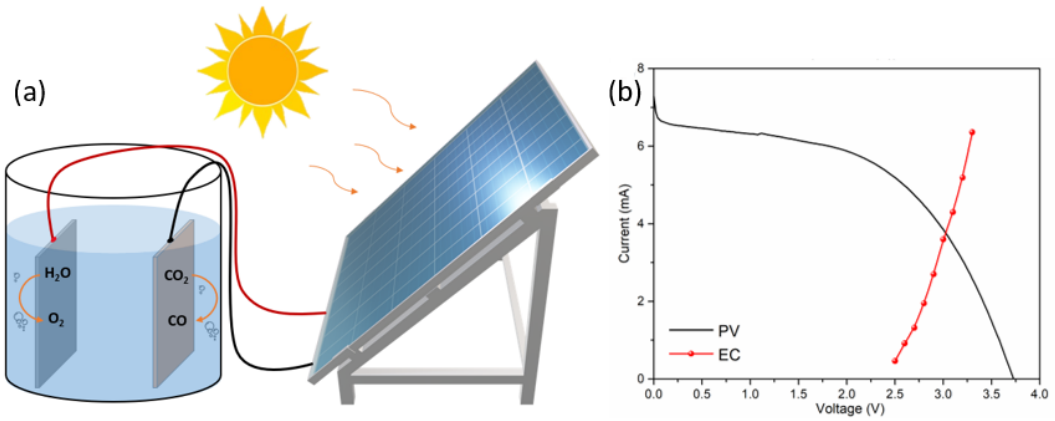

Fig. 2.8 (a) Depiction of a PV-EC system. (b) I-V characteristic of the solar cell (black) and electrochemical cell reactor (red). Reprinted with permissions under the CCA 4.0, from [97].

To achieve the highest possible solar-to-fuel efficiency, it is essential to position the operating point such that the PV module functions near its maximum power point

(MPP), where it delivers the highest power output, while the EC cell maintains peak selectivity for the targeted reaction products. This delicate balance ensures that the system not only captures solar energy effectively but also directs it toward the most efficient chemical conversion process, ultimately maximizing the overall energy conversion efficiency.

2.2.2 Solar Cell J-V Characteristics

A solar cell operates as a specialized semiconductor diode, where the absorption of light generates charge carriers (electrons and holes), introducing an additional "light-induced current" (I_L) to the intrinsic “dark current” present in the absence of illumination. The overall current flowing through the solar cell can be approximated by the following equation:

$$I \approx I_L - I_0 \left[exp\left(\frac{qV}{gkT}\right) - 1 \right] \tag{2.11}$$

where q represents the elementary charge of an electron, k is the Boltzmann Constant, V denotes the voltage applied across the cell, I_0 corresponds to the dark saturation current, which is a measure of recombination losses, and g is the ideality factor, indicating how closely the diode follows an ideal behavior.
When the solar cell is exposed to light, the generated photocurrent effectively shifts the diode’s I-V curve downward, enabling the extraction of electrical power. A qualitative representation of this I-V characteristic is shown in Fig. 2.9.
To assess the performance of a photovoltaic (PV) device, several key electrical parameters must be considered:

- **Open-Circuit Voltage (V_{OC})**: The maximum voltage the solar cell can generate when no external load is connected (I=0).
- **Short-Circuit Current (I_{SC})**: The maximum current produced by the cell when the terminals are shorted (V=0).
- **Fill Factor (FF)**: A measure of the cell’s quality and efficiency in converting the available power. It is defined as the ratio between the actual maximum power output (P_{MP}) and the theoretical maximum power derived from the

product of V_{OC} and I_{SC}:

$$FF = \frac{P_{MP}}{P_{max}} = \frac{V_{MP}I_{MP}}{V_{OC}I_{SC}} \tag{2.12}$$

where I_{MP} and V_{MP} are the current and voltage at the maximum power point, respectively. A high fill factor indicates an efficient and well-designed solar cell.

- **PhotoConversion Efficiency (*PCE*)**: The percentage of incident solar power converted into electrical power. It is calculated as:

$$PCE = \frac{FF \times V_{OC} \times I_{SC}}{P_{in}} \tag{2.13}$$

where P_{in} is the incident optical power per unit area.

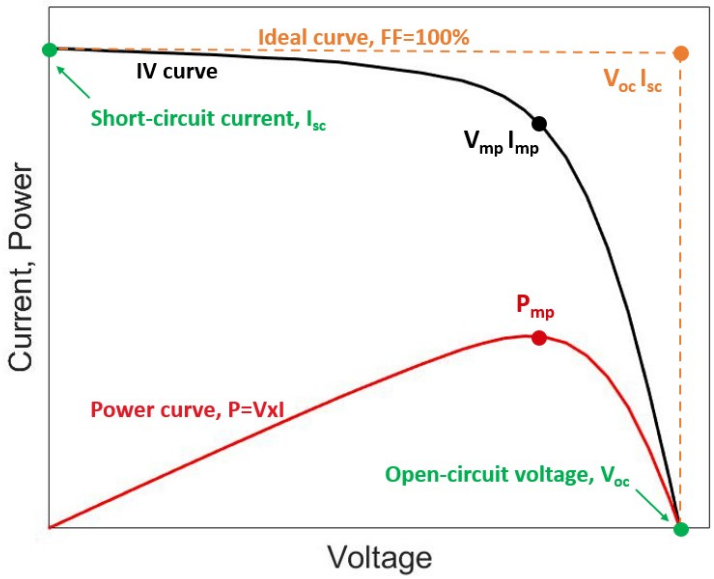

Fig. 2.9 Current–voltage characteristic for an illuminated solar cell. Reprinted with permissions under the CCA 4.0, from [97].

For consistency in evaluating solar cell performance, measurements are typically conducted under Standard Test Conditions (STC), which include:

- An air mass (AM) of 1.5, corresponding to the spectral distribution of sunlight after passing through the atmosphere at a 48° zenith angle.

- A reference irradiance P_{in} of 1000 W/m^2 (commonly referred to as 1-sun illumination)
- A cell temperature of 25°C under controlled environmental conditions.
- Minimal wind influence to prevent additional cooling effects.

By analyzing these parameters, researchers and engineers can determine the efficiency and suitability of a solar cell for practical applications, optimizing both its material properties and device architecture to enhance energy conversion.

2.2.3 Solar Cell Generations

The PV sector has undergone significant advancements over the past five decades, benefiting from continuous technological improvements and refinements [112]. While a variety of PV technologies are now available, selecting the appropriate PV component for a PV-EC system is crucial, as its performance directly influences the solar-to-carbon conversion efficiency (see Eq. 2.14 below) of the overall device. Wafer-based solar cells, commonly categorized as first-generation PVs, include single and multi-crystalline silicon (Si) cells. These technologies remain the most commercially widespread due to their high efficiency in large-scale production. However, the fabrication of silicon wafers involves considerable costs, which increases the dollar-per-watt ($/W) metric [113], which is a critical factor when aiming for cost-effective PV-EC integration. Additionally, the V_{OC} of a single-junction silicon cell typically ranges between 0.5 V and 0.6 V, necessitating the series connection of multiple cells to meet the voltage requirements of eCO_2RR.
Second-generation PV technologies eliminate the need for bulk silicon wafers by adopting a thin-film architecture. These solar cells utilize materials such as amorphous or polycrystalline silicon (a-Si, p-Si), cadmium telluride (CdTe), and copper indium gallium diselenide (CIGS) [114], which are deposited onto substrates including low-cost glass, flexible plastics, or transparent conductive oxides (TCOs). Due to their reduced material consumption, thin-film PVs enable lower production costs in large-scale manufacturing. Furthermore, their flexible nature and lightweight design make them attractive for applications where aesthetics and adaptability are essential considerations.
The third generation of PV technologies aims to overcome the efficiency limitations

inherent to single-junction devices by introducing innovative concepts such as heterojunctions, tandem cells, perovskite solar cells (PSCs), and dye-sensitized solar cells (DSSCs). Tandem cells, for instance, incorporate multiple stacked photoactive layers with progressively decreasing bandgaps from the top to the bottom, thereby enabling broader absorption of the solar spectrum and achieving superior efficiency. In contrast, DSSCs operate on a fundamentally different principle compared to conventional semiconductor-based cells: in particular, as photoelectrochemical devices, they are capable of decoupling the processes of charge photogeneration and charge transport. First introduced in 1988 by Brian O'Regan and Michael Grätzel, DSSCs have garnered attention due to their cost-effective manufacturing and the use of environmentally friendly materials such as titanium dioxide (TiO_2) and organic dyes [115–117].

Among the most rapidly evolving solar technologies is the perovskite solar cell (PSC). Named after the mineralogist L.A. Perovski, these cells utilize perovskite-structured crystals as the primary energy-harvesting material. The general formula for these crystals is ABX_3, where A represents cations occupying a cubo-octahedral site coordinated with 12 X anions, while B cations are positioned within an octahedral site shared with six X anions. A widely studied class of perovskites includes organic-inorganic metal halide compounds such as $CH_3NH_3PbX_3$, where X denotes halogen ions like bromine (Br), chlorine (Cl), or iodine (I) [118–120]. Figure 2.10 presents an overview of the evolution of PV technologies since 1975 alongside their respective cell efficiencies, as reported by the National Renewable Energy Laboratory [121].

In PV-EC devices, the solar cell strongly impacts the solar-to-carbon efficiency η_{stc}, defined as [122]:

$$\eta_{stc} = \frac{\mu_{th} \times J_{op}}{P_{in}} \times FE \tag{2.14}$$

where J_{op} refers to the operational current density and μ_{th} the thermodynamic potential (0.11 V for CO). The solar-to-carbon efficiency is a figure of merit which describes how efficient is the PV-EC system to utilize solar energy for the chemical fuels production: to maximize this parameter, both photogeneration of carriers and the right PV technology impact in the overall efficiency. As a practical example, research conducted by Gurudayal et al. [123] investigated the influence of different PV configurations on photoelectrochemical CO_2 conversion. Two PV systems were tested to assess their impact on overall performance. In the first setup (TD1), two commercial silicon solar cells were connected in series, yielding a V_{OC} of 1.1 V

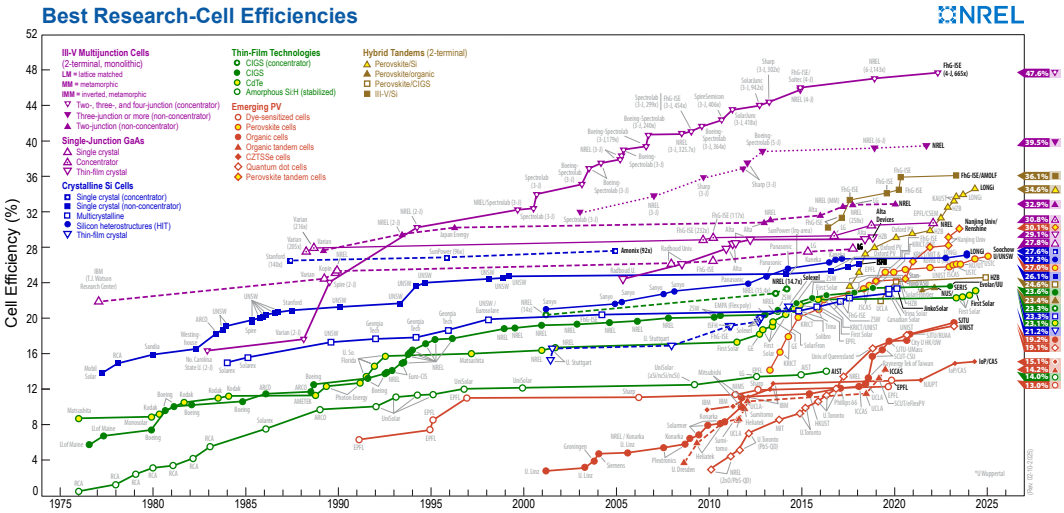

Fig. 2.10 Current state of the art of the different solar cell technologies available [121].

and an I_{SC} of 61.3 mA under standard 1-sun illumination. The second configuration (TD2) employed two custom-fabricated III-V Si tandem cells, achieving a higher V_{OC} of 1.4 V but a lower I_{SC} of 33.4 mA under the same illumination conditions. Both systems incorporated a maximum power point tracker to ensure optimal power matching. The electrochemical CO_2 reduction process took place in an EC module utilizing IrO_2 nanotubes as the anode, a CuAg cathode, and a $CsHCO_3$ electrolyte with varying concentrations (0.1 M to 0.5 M). The study revealed that the PV architecture significantly influenced η_{stc}: the TD1 system achieved an efficiency of 3.9%, whereas the TD2 configuration demonstrated a higher η_{stc} of 5.6%. These findings underscore the critical role of PV selection in optimizing the performance of integrated PV-EC systems.

Dye-Sensitized Solar Cells

As already introduced in Chapter 1, the present work exploits a module of DSSCs for energy harvesting in the PV-EC device. The fundamental working principle of DSSCs revolves around a photoactive dye, which absorbs sunlight and generates electron-hole pairs, a mesoporous semiconductor layer that facilitates electron transport, and an electrolyte that completes the circuit by regenerating the dye. In a typical DSSC configuration utilizing titanium dioxide as the semiconductor, a ruthenium (Ru)-based dye as the photosensitizer, and platinum as the counter electrode, the

operation follows a sequence of charge generation, separation, and transport, as shown in Fig. 2.11.

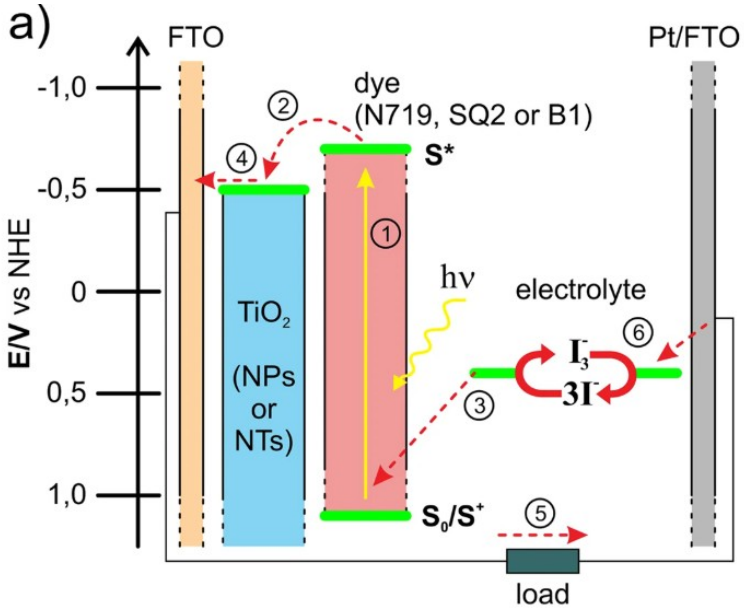

Fig. 2.11 Scheme of the working principle of a dye-sensitized solar cell. Reprinted with permissions under the CCA 4.0, from [124].

When sunlight strikes the DSSC, the Ru-based dye molecules anchored to the TiO_2 surface absorb photons, exciting electrons from the ground state to an excited state (S^*):

$$S \rightarrow S^* \tag{2.15}$$

The high-energy electrons are then injected into the conduction band of TiO_2, which acts as an electron transport medium:

$$S^* \rightarrow S^+ + e^- \tag{2.16}$$

Due to its mesoporous structure, TiO_2 provides a large surface area for dye adsorption, enhancing the efficiency of light harvesting. The injected electrons diffuse through the TiO_2 network towards the transparent conducting oxide layer, typically fluorine-doped tin oxide (FTO), which serves as a current collector. Meanwhile, the oxidized Ru-based dye must be regenerated to sustain continuous electron injection. This process is facilitated by the electrolyte, which contains a redox couple, usually iodide/triiodide (I^-/I_3^-). The electrolyte donates electrons to the oxidized dye,

restoring it to its ground state while itself undergoing oxidation:

$$S^+ + \frac{3}{2}I^- \rightarrow S + \frac{1}{2}I_3^- \tag{2.17}$$

To close the circuit, the platinum counter electrode catalyzes the reduction of triiodide back to iodide, allowing the redox cycle to continue without significant losses

$$\frac{1}{2}I_3^- + e^- \rightarrow \frac{3}{2}I^- \tag{2.18}$$

Platinum is chosen for this role due to its high catalytic activity and excellent electrical conductivity, ensuring efficient charge transfer and maintaining the cell's overall performance.

The efficiency of DSSCs is influenced by several factors, including the energy alignment between the dye and TiO_2, the electron lifetime in the semiconductor, the recombination rate of charge carriers, and the stability of the electrolyte. Ru-based dyes are particularly effective due to their strong light absorption in the visible spectrum, high charge-transfer efficiency, and chemical stability. TiO_2, as the semiconductor, plays a critical role in controlling the electron transport dynamics, while the platinum counter electrode ensures a rapid and efficient redox reaction, minimizing internal resistance.

DSSCs have garnered interest due to their relatively low production costs, flexibility, and potential for large-scale deployment. However, challenges such as the degradation of the electrolyte and the reliance on expensive ruthenium-based dyes and platinum counter electrodes remain areas of active research. Efforts to enhance the efficiency and stability of DSSCs involve the exploration of alternative dye molecules, novel semiconductor materials, and cost-effective counter electrodes.

2.2.4 Solar-Driven CO production

The most fundamental configuration for a PV-EC system is the single-cell setup, as illustrated in Fig. 2.4a. One of the earliest investigations in this field was conducted by Schreier et al. [125] in 2015. Their study utilized a series of three perovskite solar cells, which together provided a V_{OC} of 3.1 V and a I_{SC} of 1.65 mA, serving as the energy harvesting unit. This system was connected with an electrochemical single cell designed to operate at a I_{op} of approximately 1.65 mA. The schematic of

the PV-EC device and the corresponding energy diagram are illustrated in Fig. 2.12. One of the primary challenges encountered in this configuration is the crossover of dissolved products. To circumvent this issue while minimizing additional energy losses, the researchers opted for a single-cell design without an ion-exchange membrane, thereby avoiding the overpotentials that typically arise from pH gradients at membrane interfaces. A CO_2-saturated 0.5 M $NaHCO_3$ solution was employed as the electrolyte to facilitate ion conduction. For the electrochemical reactions, IrO_2 served as the anode material for the OER, while a gold electrode functioned as the catalyst for the eCO$_2$RR at the cathode. The experimental results demonstrated that the system achieved a FE of approximately 90% and a solar-to-chemical conversion efficiency exceeding 6.5% when operated at an applied voltage of 2 V for 18 hours. These findings provided compelling evidence that such PV-EC systems exhibit stable long-term performance under continuous operation, laying the foundation for further advancements in this technology.

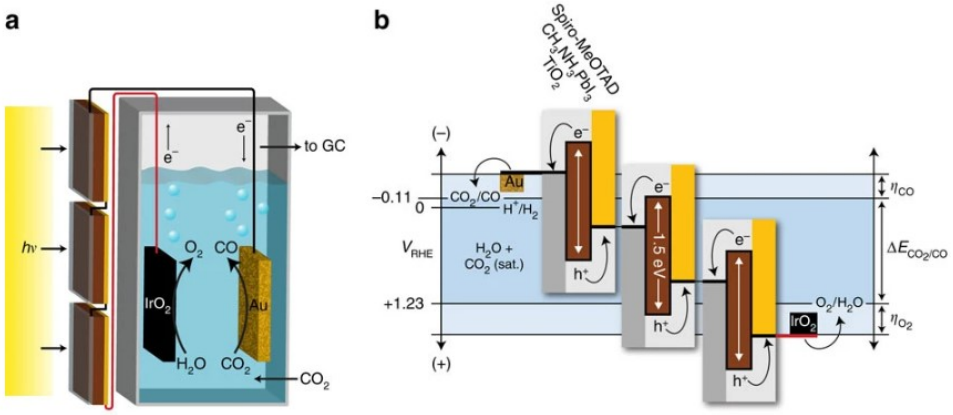

Fig. 2.12 (a) Scheme of the PV-EC device. (b) Overpotentials and reaction free energies of the series-connected perovskite cells and the CO_2-CO conversion. Reprinted with permissions under the CCA 4.0, from [97].

Arai et al. [126] demonstrated a solar-to-CO conversion efficiency of 3.4% by connecting six polycrystalline silicon photovoltaic cells with earth-abundant catalysts for CO_2 reduction. A manganese-complex polymer ([Mn-MeCN]) supported on multi-wall carbon nanotubes, with an active area of 3.24 cm^2, exhibited high selectivity for CO production, achieving a Faradaic efficiency above 80% at an approximate current of 5 mA in a single-cell configuration. Additionally, a triple-junction amorphous silicon solar cell was incorporated into the photocathode, showcasing the potential for future monolithic artificial photosynthesis systems.

In 2021, the same research group [127] investigated alternative support materials for the Mn-complex polymer previously studied [126]. Utilizing the same poly-Si solar cells and maintaining identical electrical conditions, they found that carbon nanohorns (CNHs) provided superior support compared to carbon nanotubes for [Mn-MeCN]. The study indicated that CNHs enabled an η_{stc} of 3.3%, nearly matching the previously reported performance, while requiring a smaller electrode area (1 cm^2 versus 3.24 cm^2).

In a pioneering effort, Sacco et al. [128] experimentally demonstrated the first fully integrated PV-EC device. Their system consisted of a module of five DSSCs (V_{OC}= 3.73 V, I_{SC} = 7 mA), where the platinum electrode served as both the cathode for the DSSCs and the anode for the electrochemical cell, facilitating the OER. The device achieved unassisted CO_2 reduction to CO, catalyzed by a Cu-Sn cathode, with a Faradaic efficiency of 78% and an η_{stc} of 0.79%. Although the overall performance was lower than other reported systems, this work demonstrated the feasibility of fully integrated stand-alone PV-EC systems.

Regarding PV-EC systems utilizing H-type cells (as illustrated in Fig. 2.4b), Schreier et al. [129] employed a triple-junction GaInP/GaInAs/Ge solar cell with a power conversion efficiency of 28.5% at 2.24 V. This photovoltaic unit was coupled with SnO_2-modified CuO nanowires, serving as catalysts in both the cathodic and anodic compartments. An ion-exchange membrane was used to separate the anodic and cathodic chambers, with 0.1 M $CsHCO_3$ and 0.25 M CsOH solutions acting as catholyte and anolyte, respectively. Their PV-EC system achieved a Faradaic efficiency of approximately 81% and a solar-to-carbon efficiency of 13.4%.

Chung et al. [130] investigated a system in which three perovskite solar cells were linked to Cobalt-phosphate (Co-Pi) and Au dendrite electrodes, tailored for the OER and CO_2 reduction reaction, respectively. Operating at a current of 2.1 mA, their configuration achieved a Faradaic efficiency of 80% and a solar-to-carbon efficiency exceeding 8% for CO production.

Similarly, Bae et al. [131] employed a setup comprising three triple-junction silicon photovoltaic cells connected to IrO_2 and nanoporous Au catalysts for OER and eCO_2RR, respectively. This design reached a FE of 100% and an η_{stc} of 5.3%.

In a bid to reduce production costs and develop environmentally sustainable devices using earth-abundant electrocatalysts, Zhang et al. [132] utilized a custom-built, large-area perovskite solar cell based on $[Cs_{0.05}(FA_{0.85}MA_{0.15})_{0.95}]Pb_{0.9}(I_{0.85}Br_{0.15})_3$ (CsFAMA) with a operational voltage V_{op} of 4.6 V and a I_{SC} of 4.3 mA. They paired

this with a low-cost catalyst featuring single-atom cobalt anchored on Zr_6-cluster-porphyrin framework hollow nanocapsules (Co-SAs/Zr-CPF) and utilized RuO_2 on carbon paper for the OER. Owing to the hollow morphology and well-dispersed Co single atoms, the catalyst exhibited remarkable activity in converting CO_2 to CO, achieving an η_{stc} of 12.5%.

Expanding the versatility of PV-EC systems, ion exchange membranes and multi-stage components have been incorporated to enable more sophisticated applications. In 2018, Wang et al. [133] introduced a redox-medium-assisted system that mimics the light and dark reactions of green plants. In their design, photogenerated electrons from an InGaP/GaAs/Ge photovoltaic cell (with V_{OC} = 2.54 V and I_{SC} = 4.38 mA) are stored in a zinc/zincate (Zn/Zn(II)) redox pair, which allows for controlled electron release to drive the spontaneous reduction of CO_2. By employing nano-gold and nickel–iron hydroxides as catalysts for eCO$_2$RR and OER, respectively, the system attained a FE of approximately 92% and an η_{stc} of 15.6% at a fixed current of 3.2 mA. A schematic representation of this innovative system is provided in Fig. 2.13 .

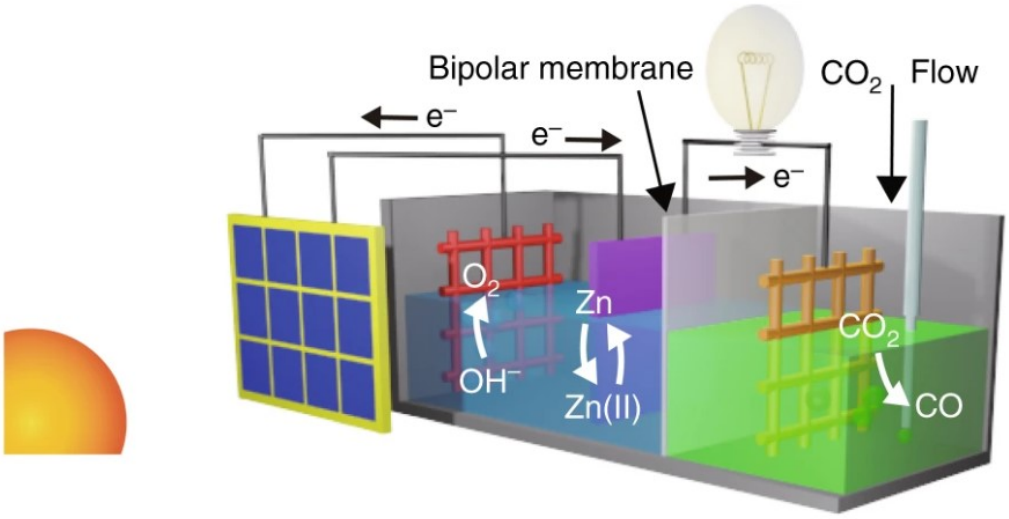

Fig. 2.13 Solar-driven CO_2 reduction in redox medium. Reprinted with permissions under the CCA 4.0, from [97].

A novel approach to the simultaneous electrochemical conversion of CO_2 and H_2S into CO and elemental sulfur has been demonstrated through the design of a photovoltaic-electrochemical (PV-EC) system [134]. This system is powered by a single three-junction silicon solar cell and operates by facilitating CO_2 reduction at the cathode, generating CO as the primary product. Meanwhile, in the anodic compartment, an iron-based redox couple (EDTA-Fe^{2+}/EDTA-Fe^{3+}) undergoes elec-

trolysis. The chemical energy accumulated in the solution is subsequently utilized to drive the conversion of H_2S into sulfur and protons. The protons migrate across the bipolar membrane, completing the electrical circuit and ensuring continuous operation.

Significant research efforts have been dedicated to improving the efficiency of PV-EC devices, particularly in enhancing solar-to-carbon conversion efficiencies through the implementation of GDEs in flow-type cells, as illustrated in Fig. 2.4c. One such study, conducted by Kim et al. [135], explored the use of Au clusters anchored onto the microporous layer of a GDE, facilitating the electrochemical reduction of gaseous CO_2 to CO. The system was designed with an inverse opal (IO) structured NiFe catalyst for the OER in a 3 M KOH electrolyte. When coupled with a GaInP/GaAs solar cell, the device achieved remarkable FEs exceeding 90%, with a η_{stc} of 18% under a pure CO_2 gas stream. Even when operating under conditions resembling industrial flue gas compositions (10% CO_2), the system maintained an η_{stc} of 15.9%. The researchers emphasized the necessity of employing larger photovoltaic areas to support high CO partial current densities (>200 mA/cm^2), capitalizing on the higher current densities attainable with GDEs.

Cheng et al. [136] further advanced the PV-EC concept by employing a flow cell structure integrated with a GaInP/GaInAs/Ge multi-junction solar cell (V_{OC} = 2.6 V, I_{SC} = 4.37 mA). In their configuration, a nickel anode was used in a 1 M KOH electrolyte, while silver nanoparticles (Ag-NPs) were incorporated into the GDE at the cathode. To mitigate electrode flooding (a common challenge in gas-fed electrochemical systems) the authors adopted a reverse-assembled configuration in which the Ag-NPs directly faced the CO_2 gas stream. This optimized design allowed the system to achieve an impressive FE of 99% and a η_{stc} of 19.1% under simulated AM 1.5G solar illumination at one sun. Under real outdoor lighting conditions at midday, the efficiency slightly decreased to 18.7%, demonstrating the robustness of the system in practical environments.

More recently, in 2022, Wang et al. [137] explored the potential of single-atom catalysts for CO_2 electroreduction in PV-EC systems. Their study focused on a Co-based catalyst featuring CoN_4 active sites supported on a carbon black matrix (CoN_4-CB), which served as the GDE material in a flow cell. When paired with a commercial amorphous silicon (a-Si) photovoltaic module (V_{OC} = 3.51 V, I_{SC} = 103 mA) and a nickel foam catalyst in the OER compartment, the system demonstrated a high faradaic efficiency (≈92.1%) and a solar-to-carbon efficiency of 4.9%, operating

at an optimal current of 99.2 mA. To provide a comprehensive understanding of the device performance and the key operational parameters, Fig. 2.14 presents the experimental setup, I-V characteristics, and efficiency data for the PV-EC system.

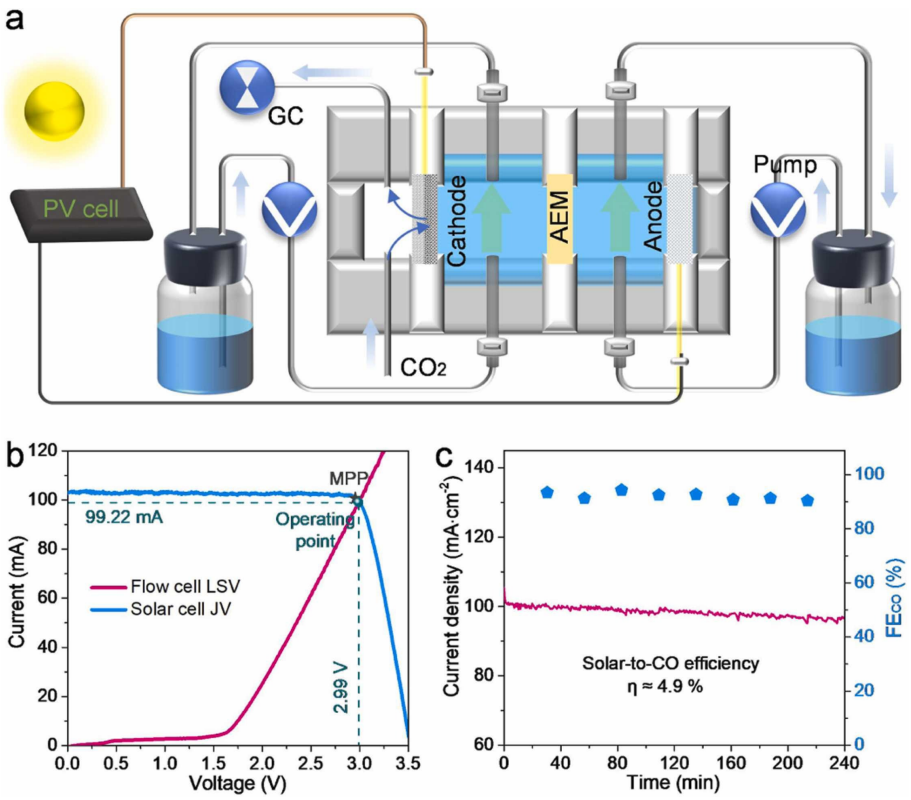

Fig. 2.14 (a) Flow cell and PV-EC connection scheme. (b) I-V characteristics at 1 SUN illumination. (c) Stability test representing FE and current density vs. time. Reprinted with permissions under the CCA 4.0, from [97].

Finally, leveraging zero-gap electrolysis technology (illustrated in Fig. 2.4d), Lee et al. [138] successfully developed a large-scale PV-EC system integrated with silicon-based solar cells, featuring a substantial active area of 120 cm^2. This configuration demonstrated a η_{stc} of 12.1% and an exceptionally high FEs of 99%, operating at a remarkable current of approximately 1.1 A. When normalized to the illuminated photovoltaic surface, the J_{op} reached approximately 9.2 mA/cm^2.

To accommodate the high current output generated by the photovoltaic module, the researchers employed a zero-gap electrochemical cell as the CO_2 electrolyzer. This cell was designed with a tungsten-seeded silver dendrite catalyst (W@AgD/C) to facilitate CO_2 eCO$_2$RR at the cathode, while a Fe-doped cobalt foam catalyst was utilized for the OER at the anode, with 1 M KOH serving as the electrolyte. The

zero-gap configuration enables improved mass transport and enhanced reaction kinetics, optimizing the system's performance under high-current operating conditions. A key aspect of this study was the evaluation of the device's viability in real-world settings. The researchers deployed the PV-EC system on the rooftop of a building, exposing it to natural solar radiation. Under outdoor conditions, the device exhibited current fluctuations that directly correlated with variations in solar irradiance, highlighting the system's adaptability to environmental changes. This behavior suggests that the proposed design holds significant promise for practical and commercial applications, where efficiency and scalability are essential. A schematic representation of the PV-EC device incorporating the zero-gap electrochemical cell is provided in Fig. 2.15.

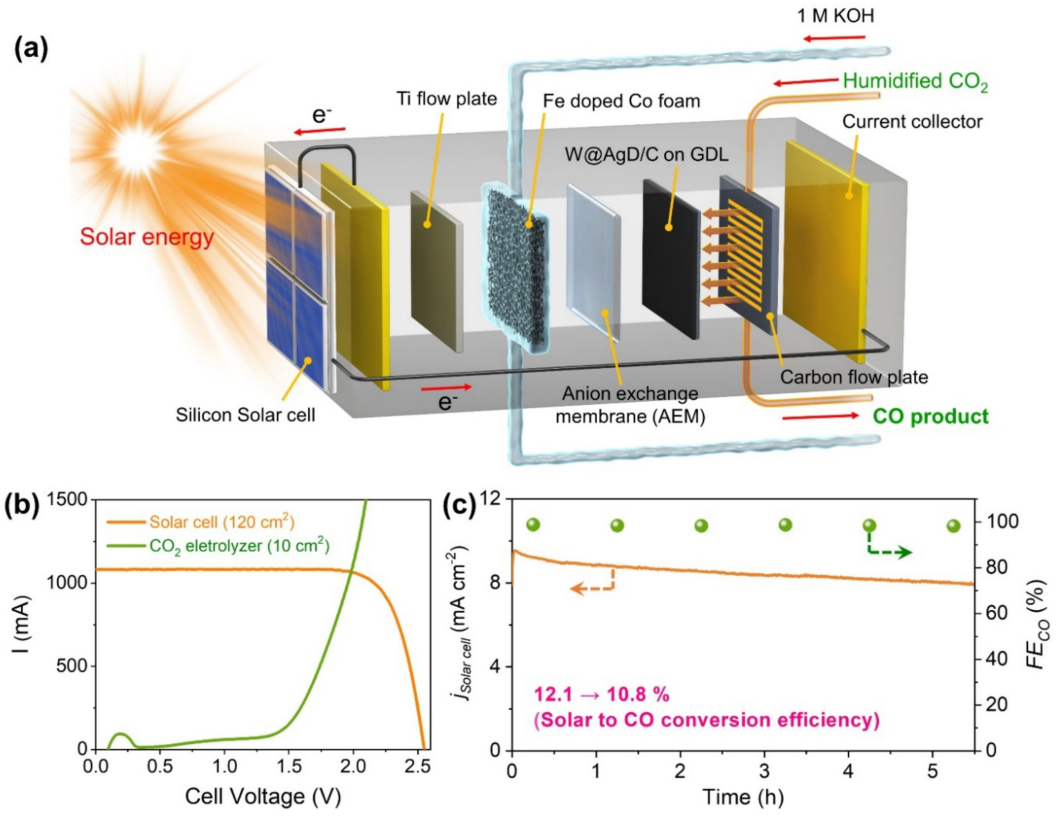

Fig. 2.15 (a) Flow cell and PV-EC connection scheme. (b) I-V characteristics at 1 SUN illumination. (c) Stability test representing FE and current density vs. time. Reprinted with permissions under the CCA 4.0, from [97].

Table 2.2 provides a comprehensive summary of the key parameters characterizing the PV-EC devices reviewed in this study. It outlines critical aspects such as the PV technology utilized, the electrical operating conditions (specifically, the operating

voltage V_{op} and current I_{op}) as well as the configuration of the electrochemical cell and its electrode materials. Additionally, it presents the faradaic efficiency and the solar-to-CO conversion efficiency, offering a comparative perspective on the performance of different systems.

Table 2.2 Literature report of PV-EC devices for CO production. The "-" sign replaces unreported data. Reprinted with permissions under the CCA 4.0, from [97].

PV (Active Area)	V_{op} **[V]**	I_{op} **[mA]**	**EC Type**	**OER Catalyst (Area)**	**CO$_2$RR Catalyst (Area)**	**FE [%]**	η_{stc} **[%]**	**Ref.**
3 series-connected Perovskite (0.285 cm^2)	2.00	1.6	Single	IrO$_2$ (4.5 cm^2)	Au (1 cm^2)	90	>6.5	[125]
6 series-connected poly-Si (1.6 cm^2)	2.19	5.1	Single	β-FeOOH:Ni/a-Ni(OH) (2 cm^2)	[Mn-MeCN] (3.24 cm^2)	82	3.4	[126]
Poly-Si (1.6 cm^2)	2.12	5.1	Single	Ni-doped β-FeOOH (2 cm^2)	CP/CNH/[Mn-MeCN] (1 cm^2)	–	3.3	[127]
DSSC module – integrated (-)	3.00	3.6	Single	Pt (-)	Cu-Sn (1 cm^2)	78	0.8	[128]
GaInP/GaInAs/Ge (0.563 cm^2)	2.38	6.5	H-type	CuO NW (20 cm^2)	CuO NW (20 cm^2)	81	13.4	[129]
3 series-connected Perovskite (0.282 cm^2)	2.68	2.1	H-type	Co-Pi (6.25 cm^2)	Au (0.025 cm^2)	80	>8.0	[130]
3 triple-junction Si (18 cm^2)	2.70	72.0	H-type	IrO$_2$ (-)	Au (1 cm^2)	100	5.3	[131]
CsFAMA-based perovskite (0.48 cm^2)	3.20	3.2	H-type	RuO$_2$/C (-)	Co-SAs/Zr-CPF (-)	–	12.5	[132]
InGaP/GaAs/Ge (0.25 cm^2)	1.96	3.2	H-type	NiFe hydroxide (0.3 cm^2)	Au (0.3 cm^2)	92	15.6	[133]
Triple-Junction Si (-)	-	-	H-type	Graphene (-)	Graphene - encapsulated ZnO (-)	-	7.5	[134]
GaInP/GaAs (1 cm^2)	1.63	14.1	Flow	NiFe IO (-)	Au (2 cm^2)	>90	18.0	[135]
GaInP/GaInAs/Ge (0.31 cm^2)	2.23	4.5	Flow	Ni (0.31 cm^2)	Ag (0.31 cm^2)	99	19.1	[136]
a-Si (25 cm^2)	2.99	99.2	Flow	Ni foam (1 cm^2)	CoN$_4$-CB (1 cm^2)	92	4.9	[137]
Si (120 cm^2)	–	1100.0	Zero-gap	Fe-doped Co foam (10 cm^2)	W@AgD/C (10 cm^2)	99	12.1	[138]

2.2.5 PV-BE Devices

Photovoltaic-Bicarbonate Electrochemical devices (PV-BE) are an attractive and more challenging technology to both capture and convert CO$_2$ with the aid of solar

energy. The integration mechanism is identical with respect to PV-EC devices, but in this case bicarbonate electrolyzers are used instead of classic CO_2 reduction electrochemical cells. To the best of our current knowledge, there is no existing literature on such devices; therefore, this system is presented for the first time in the present work.

2.3 Numerical Modeling

In the field of eCO_2RR into valuable products, extensive research has focused on optimizing both reactor configurations and catalytic materials. The reactor design plays a crucial role in defining key electrical parameters such as energy efficiency, current density, and overall system performance. Different reactor configurations exhibit distinct characteristics that influence the electrical operation of the system. Meanwhile, the catalyst composition and structure largely determine the reaction kinetics and the selectivity toward specific desired products, directly impacting the feasibility and efficiency of CO_2 reduction.

Although the majority of advancements in this domain stem from experimental studies, computational modeling has emerged as an essential tool for predicting reactor performance and understanding the influence of critical operating parameters such as local pH variations, pressure effects and temperature dependencies. These models provide a theoretical framework that complements experimental investigations, helping researchers optimize operating conditions before implementing costly and time-consuming experimental setups.

Early modeling efforts focused on describing the diffusive boundary layer (DBL) that forms at the cathode-electrolyte interface. A significant contribution in this regard was made by Gupta et al. [139], who developed a model to evaluate the concentration profiles of protons, CO_2, bicarbonate and carbonate ions at the electrode surface, using a Cu-based catalyst in a $KHCO_3$ electrolyte. Despite limitations such as a lack of experimental validation and the consideration of only a narrow range of current densities, their study provided valuable insights into how electrolyte concentration and stirring conditions influence local reaction environments.

Building on this, Sacco et al. [140] explored the role of gas bubble dynamics in mass transport across the DBL. Their findings, which showed good agreement with experimental observations, highlighted the significant impact of gas bubbles on DBL

thickness, thereby altering the effective diffusion of reactants and products. These studies emphasized the importance of mass transport phenomena in electrochemical CO_2 reduction systems.

With the advent of advanced simulation tools such as COMSOL Multiphysics, more intricate and comprehensive reactor models have been developed. Wu et al. [141] designed a microfluidic electrochemical cell model to study CO_2 conversion into CO, validating their computational predictions with experimental data at varying flow rates. Their results demonstrated how CO_2 feed rates, channel length, and GDE porosity influence overall cell performance.

Similarly, Kotb et al. [142] introduced the first computational model of a microfluidic reactor aimed at converting CO_2 into alcohols, particularly methanol. While the simulation showed significant discrepancies compared to experimental findings, it provided crucial insights into the predominance of HER over CH_3OH production, highlighting the need for improved CO_2 transport to enhance selectivity toward alcohol formation.

Other modeling efforts have extended beyond microfluidic systems. Singh et al. [143] investigated a batch electrochemical reactor employing a $KHCO_3$ electrolyte and a CO_2 feed without electrolyte recirculation. Their work systematically analyzed factors contributing to polarization losses, which is vital for minimizing ohmic losses and improving the coupling efficiency between photovoltaic energy sources and the electrochemical reactor. However, their model lacked experimental validation and did not explicitly incorporate the competing HER process.

In another significant study, Luo et al. [144] developed a photoelectrochemical reactor model for formic acid production, simulating the system with a 0.5 M $NaHCO_3$ catholyte and a 0.5 M NaOH anolyte. Their model incorporated the Shockley–Queisser equation, fitted with a diode relation to simulate the photoanode's behavior under 100 mW/cm^2 illumination conditions. By validating their results against experimental current-voltage data under 1-sun illumination, they successfully examined how CO_2 flow rates impact current density and conversion efficiency.

High-pressure electrochemical CO_2 reduction has also been investigated computationally. Chinnathambi et al. [145] studied mass transport limitations across both the electrolyte and bipolar membranes during formic acid synthesis at pressures up to 40 bar. Their results, validated with experimental current density versus applied potential data, highlighted the crucial role of pressure-driven transport phenomena in improving conversion rates.

Advancements in two-phase flow modeling have further enriched our understanding of CO_2 electrolyzers. Yang et al. [146] developed a mathematical model for a bicarbonate electrolyzer, focusing on the complex interactions between two-phase flow, ion transport, and reactor performance. This work provided a detailed mechanistic description of gas-liquid interactions, which significantly influence electrochemical efficiency and reactant transport.

Finally, Obasanjo et al. [147] implemented a one-dimensional (1D) computational model for a bicarbonate-fed electrochemical reactor designed for CO_2-to-methane (CH_4) conversion. Their study aimed at optimizing system design to achieve higher methane yields and overall efficiency improvements.

Overall, the integration of computational modeling into electrochemical CO_2 reduction research has significantly enhanced the predictive capability of reactor performance, guiding the development of more efficient and selective conversion systems. While experimental validation remains a key challenge, these models provide a powerful framework for understanding reaction kinetics, mass transport phenomena, and system-level efficiency, ultimately contributing to the advancement of sustainable CO_2 conversion technologies.

Chapter 3

Materials and Methods

This chapter will be dedicated to the experimental methods exploited to create and characterize the device studied in the thesis. The Electrochemical Cell and the Photovoltaics will be treated separately.

3.1 Electrochemical Cell Design

The experimental system used in this study comprises a commercial batch-type electrochemical reactor (ElectroCell, Ringkoebing-Skjern, Denmark), specifically designed for performing electrochemical CO_2 reduction reactions. The reactor includes ethylene-propylene-diene monomer (EPDM) gaskets, strategically placed to establish and seal separate compartments for the anode and cathode, thus preventing the mixing of reaction products.
To ensure ionic conduction and compartmental isolation, a Nafion N117 proton-exchange membrane (Ion Power, New Castle, DE, USA) was installed as a separator between the anodic and cathodic chambers. The membrane permits selective proton transport, maintaining electrochemical continuity while avoiding physical electrolyte mixing.
The electrolyte solution employed for both compartments was an aqueous 0.1 M potassium bicarbonate ($KHCO_3$) solution, prepared by dissolving $KHCO_3$ with a purity of 99.7% (Sigma Aldrich, St. Louis, MO, USA) in distilled water. Electrolyte recirculation between the reactor and external reservoirs was continuously maintained using a peristaltic pump (model MCP ISM404B, Ismatec, Glattbrugg,

Switzerland), operated at a controlled and consistent flow rate of 1.547 mL/min.
A steady supply of CO_2 was directly introduced into the electrochemical reactor via two mass flow controllers (Bronkhorst, Ruurlo, The Netherlands), each calibrated to deliver a constant gas flow of 15 mL/min. This ensured stable CO_2 availability within the cathodic compartment.
Electrochemical reactions were facilitated by appropriate electrode materials chosen to optimize catalytic performance. The anodic electrode, facilitating the OER, was made from a commercial platinum foil (GoodFellow, Huntingdon, UK), having a geometric area of 9.9 cm^2. On the cathode side, silver nanoparticles were deposited onto a carbon paper substrate (28BC, provided by SGL Carbon, Wiesbaden, Germany) by employing a physical sputtering technique. The deposition procedure involved applying a deposition current (I_{dep}) of 50 mA for a duration (T_{dep}) of 300 s, achieving uniform nanoparticle coverage. Due to slight variations during the preparation, the resulting geometric area of the cathodic electrodes ranged between 1.2 and 1.9 cm^2 across different experimental runs.
Plastic meshes were positioned within both electrode compartments to mitigate gas bubble accumulation, enhancing the electrolyte distribution and ensuring consistent electrode-electrolyte contact.
Electrochemical performance was evaluated through chronoamperometric measurements using a potentiostat (model VSP, supplied by BioLogic, Seyssinet-Pariset, France). A two-electrode configuration was applied, controlling the voltage across the electrodes while recording the resulting current over an experimental duration typically of one hour per tested voltage.
The gaseous products generated at the cathode were identified and quantified using a Micro Gas Chromatograph (Micro-GC, model Fusion by Inficon, Bad Ragaz, Switzerland), equipped with two analytical modules: an Rt-Molsieve 5A and an Rt-Q-Bond column, each connected to a microthermal conductivity detector. Liquid products potentially formed during electrolysis were investigated using High-Performance Liquid Chromatography (HPLC, Shimadzu, Kyoto, Japan), employing: a ReproGel column (300 × 8 mm), a UV–Vis detector set to 210 nm, and a mobile phase consisted of 9.0 mM sulfuric acid (H_2SO_4). A schematic representation of the setup is depicted in Fig. 3.1.

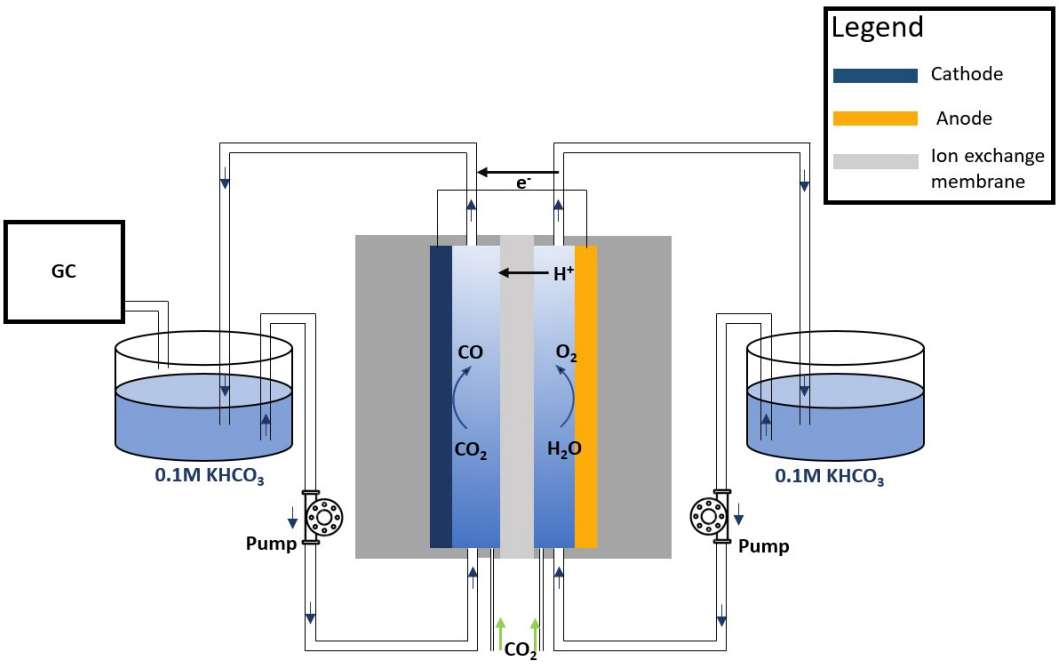

Fig. 3.1 Schematic illustration of the experimental setup used for electrochemical tests. The electrolyte is continuously recirculated between the cell and external reservoirs by two peristaltic pumps. The catholyte reservoir is sealed and directly connected to a gas chromatograph, enabling real-time analysis of gaseous reaction products. Reprinted with permissions under CCA 4.0, from [148].

3.2 Bicarbonate Electrolyzer Design

For what concerns the bicarbonate electrolyzer, it has been developed a home-made cell with a flow field of area 2 cm^2, to better match the current with the PV module for the integration [149]; both the metal plates are made of stainless steel 904 L, and designed with Solidworks (Fig. 3.2).

The anode catalyst is a Ni foam (from Goodfellow), with 0.9 width and 4-5 cm^2 of area. The membrane used is a bipolar membrane (from Fumasep), while the cathode catalyst is the same as previously reported in Section 3.1.

For the electrochemical test, the anolyte is a 1 M KOH solution (purchased from Supelco, 84%), and the catholyte is a 2M $KHCO_3$ solution. All the experimental setup is the same as reported in Fig. 3.1, with the difference that no CO_2 is fluxed: at the cathode, only N_2 is fluxed with a mass flow of 20 mL/min, which acts as carrier gas.

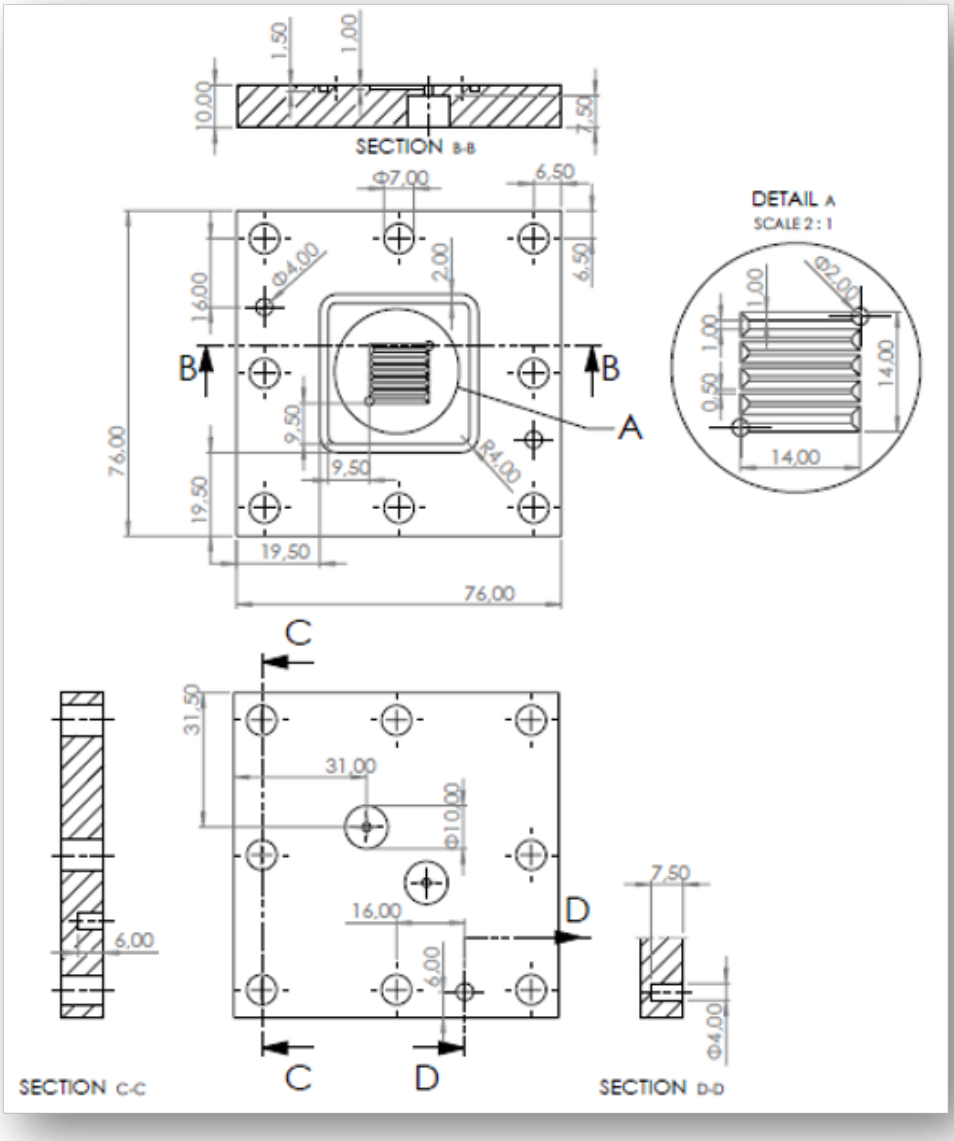

Fig. 3.2 Deisgn of the flow plates for the custom electrolyzer. Reprinted from [149].

3.3 DSSC Module Fabrication

The energy required to drive the electrochemical CO_2 reduction was provided by a photovoltaic module composed of six DSSCs electrically connected in series. The DSSC module employed in this study was prepared using a multi-step fabrication process. The cathodic electrode consisted of platinum films deposited onto FTO glass

substrates (TCO30-10, 3 mm thickness, 10 ohm/sq., supplied by Solaronix, Aubonne, Switzerland) through sputtering, applying a I_{dep} of 30 mA for T_{dep}= 20 seconds. The substrates were carefully masked to create uniform, rectangular platinum films with a defined active area of approximately 1 cm^2, and holes were drilled into the FTO substrates to facilitate electrolyte injection.

For the photoanodes, a layer of commercial TiO_2 paste (Ti-Nanoxide, from Solaronix, Aubonne, Switzerland) was uniformly deposited on FTO glass substrates using the doctor-blade technique. Following deposition, the substrates were dried on a hot plate at 100 °C to remove solvent residues, then annealed at 475 °C for 30 minutes to ensure proper sintering of the TiO_2 particles. Once annealed, the TiO_2 photoanodes were sensitized by immersion in an ethanol solution containing 0.3 mM of ruthenium-based dye (N719, Ruthenizer 535-bisTBA, Solaronix, Aubonne, Switzerland) for a minimum of 17 hours, ensuring adequate dye loading onto the semiconductor surface. The final DSSC cells were assembled by sealing the sensitized TiO_2 photoanodes and platinum counter-electrodes together with a thermoplastic sealant (Meltonix 1170-60, Solaronix, Aubonne, Switzerland). This sealing was conducted under pressure using a hot press operating at approximately 110 °C. Once sealed, the cells were filled with an electrolyte solution containing 0.45 M sodium iodide (NaI), 0.056 M iodine (I_2), and 0.55 M 4-tert-butylpyridine (TBP) dissolved in 3-methoxypropionitrile ($CH_3OCH_2CH_2CN$), purchased from Sigma-Aldrich (St. Louis, MO, USA).

The completed photovoltaic module, comprising six DSSCs interconnected using conductive silver paste, was characterized by recording current–voltage (I–V) curves under simulated solar irradiance conditions. These measurements were performed using a class ABA LED solar simulator (MiniSol LSH-7320, from Oriel, Irvine, CA, USA), enabling precise control and variation of the illumination intensity, expressed in units of suns (where 1 sun corresponds to 1 kW/m^2). The resulting I–V curves provided essential data to evaluate and optimize the module's electrical performance under realistic solar irradiation conditions. A diagram of the PV-EC device is depicted in Fig. 3.3.

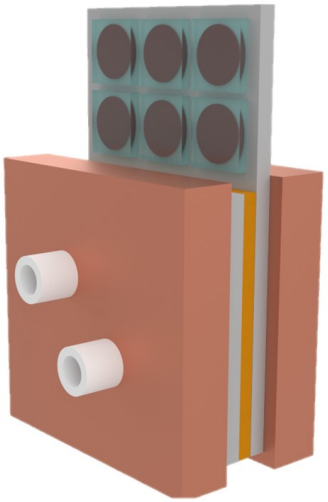

Fig. 3.3 Diagram of the integrated PV-EC system. Reprinted with permissions under CCA 4.0, from [148]

Chapter 4

PV-EC Mathematical Modeling

In this section, the mathematical model will be explained in depth, with all the constituting equations and approximations. At first, the model for the electrochemical CO_2 reduction is presented, with the parameters fitted with the experimental setup. Lastly, a suitable mathematical expression for the PV module is reported. Part of the work shown in this chapter has been previously published [150].

4.1 EC Model

The reactor is represented using a two-dimensional geometry, as shown in Figure 4.1, based on the assumption that key chemical and electrochemical properties—such as species concentrations, overall current density, individual partial current densities, and product selectivity remain uniform along the cell's depth (as demonstrated in Section 5.2). This 2D approach, implemented in COMSOL Multiphysics 6.1, simplifies the model without sacrificing essential details.

In the simulation, the electrodes are modeled as infinitesimally thin films: Ag nanoparticles represent the cathode and Pt foil the anode, each positioned at the boundaries of the simulation domain. The cathodic and anodic compartments are physically separated by a Nafion 117 proton exchange membrane (PEM), ensuring proper ion transport between the two regions.

Both compartments are filled with a 0.1 M aqueous $KHCO_3$ solution, which recirculates continuously. Before entering the reactor, the electrolyte is saturated with CO_2 in external reservoirs; after the electrochemical reactions occur, it exits the system

carrying the reaction products, which is to say CO, H_2 (at the cathode) and O_2 (at the anode). Although these products have low solubility at ambient pressure, they are assumed to remain in the liquid phase in order to avoid unnecessary model complexity. Furthermore, the system is treated as isothermal with a constant temperature of 298.15 K. Due to the diluted electrolyte and the relatively low current applied, any heat generation from electrical losses can be, in fact, considered negligible.
The following sections outline the core aspects of the mathematical model across the different domains of the simulation.

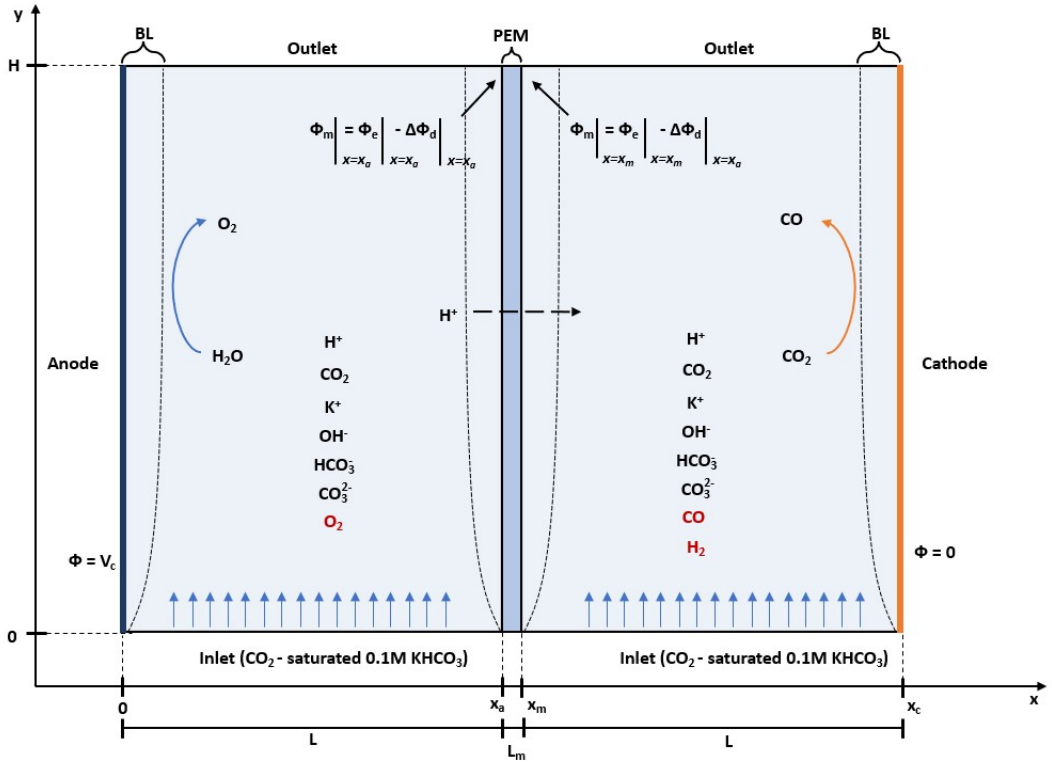

Fig. 4.1 Highlights of the 2D Model. In this schematic, ϕ_m denotes the potential across the membrane, while ϕ_e represents the electrolyte potential, and V_c is the voltage applied to the cell. Both compartments are characterized by identical dimensions, having a length L and height H, whereas the membrane extends over a length L_m. The x-coordinates corresponding to the boundaries of the anode, the membrane, and the cathode are labeled as x_a, x_m, and x_c, respectively. Reprinted with permissions under the CCA 4.0, from [150].

4.1.1 Electrolyte domain

In the electrolyte domain, the charge transport occurs primarily through the movement of ions, not electrons: this process is known as ionic conduction. Ions (both cations and anions), in fact, are the mobile charge carriers: when the cell operates, these ions move under the influence of an electric field and concentration gradients. This movement helps maintain charge balance, ensuring overall electrical neutrality and completing the internal circuit of the cell. To properly model the electrolyte domain, mathematical equations for the ionic current must be taken into account.
For what concerns the ionic current distribution, it has been retrieved by the sum of the ionic fluxes of the single ionic species present in the electrolyte:

$$J_e = F \sum_i z_i N_i \tag{4.1}$$

where J_e is the electrolyte current density, F the Faraday constant, z_i the charge number of the i-th species and N_i the ionic mass flux. As shown in Fig. 4.1, the species considered in the domain are CO_2, K^+, OH^-, H^+, HCO_3^- , CO_3^{2-} , H_2, CO, O_2. It is worth underlying that neutral species do not contribute to the overall current, due to null charge number.
The ionic mass flux N_i represents the quantity of ionic species transported per unit area per unit time within the electrolyte, due to a combination of three effects:

- **Diffusion**: movement driven by concentration gradients (species move from high to low concentration regions), described by Fick's law.
- **Migration**: transport of charged ionic species induced by an electric field. Ions migrate towards regions of opposite charge, driven by electric potential gradients within the electrolyte.
- **Convection**: movement resulting from bulk fluid flow of the electrolyte solution.

This combined transport phenomenon is mathematically described by the Nernst–Planck equation:

$$N_i = -\underbrace{D_i \nabla c_i}_{\text{diffusion}} - \underbrace{z_i u_{mob,i} F c_i \nabla \Phi_e}_{\text{migration}} + \underbrace{c_i u}_{\text{convection}} \tag{4.2}$$

where D_i is the diffusion coefficient and c_i indicates the concentration. Additionally, $u_{mob,i}$ represents the ionic mobility, F is the Faraday constant, Φ_e corresponds to the electrolyte potential, and u is the velocity vector of the electrolyte. The ionic mobility is linked to the diffusion coefficient via the Nernst–Einstein relation, which reads as follows:

$$u_{mob,i} = \frac{D_i}{RT} \tag{4.3}$$

with T the temperature, and R the molar gas constant.
Concerning mass conservation, species mass continuity is considered. It refers to the fundamental principle expressing the conservation of mass for each ionic and neutral species within the electrolyte domain: in other words, the total amount of any given species entering, leaving, reacting, or accumulating within a specific volume element of the system must remain balanced. Mathematically, this principle is expressed by the continuity equation for species i:

$$\nabla \cdot N_i + u \cdot \nabla c_i = R_i \tag{4.4}$$

In the above equation, the term $\nabla \cdot N_i$ describes the divergence of the ionic flux N_i, capturing how the spatial distribution of species flux varies within the electrolyte. A positive divergence indicates a net outward flux from the control volume, while a negative divergence corresponds to a net inward flux. The convective term, $u \cdot \nabla c_i$, represents changes in species concentration c_i due to bulk fluid flow, showing how fluid motion redistributes species concentrations throughout the electrolyte domain. Finally, the source term R_i indicates the rate of local production or consumption of species i. Typically, within the bulk electrolyte (where only equilibrium reactions occur) R_i is set to zero. At electrode surfaces or reaction interfaces, however, R_i becomes nonzero, reflecting electrochemical reactions that produce or consume species ($R_i > 0$ and $R_i < 0$, respectively). The charge conservation is considered as well:

$$\nabla \cdot J_e = 0 \tag{4.5}$$

The equation asserts that the divergence of the electrolyte current density must be zero throughout the domain, indicating there is no net accumulation or depletion of charge at any point within the electrolyte. In other words, electric currents entering a defined volume exactly equal those leaving it, thereby preserving electrical neutrality

over time. Finally, electroneutrality holds in the electrolyte domains:

$$\sum_i z_i c_i = 0 \tag{4.6}$$

This condition arises from the principle that significant electric charge imbalances are energetically unfavorable and quickly neutralized by ionic rearrangement within the solution. Following this hypothesis, any local excess of positive charges must be immediately compensated by an equivalent amount of negative charges, ensuring that large-scale electric fields do not develop spontaneously within the electrolyte [151].

When CO_2 dissolves in aqueous electrolytes, several chemical equilibria are rapidly established among various ionic and neutral species. These equilibrium reactions significantly influence the distribution of chemical species within the electrolyte, especially near electrode surfaces where reactions alter local concentrations. In the present electrochemical system, the following carbonate-bicarbonate equilibria, together with the self-ionization of water, are explicitly considered due to their rapid kinetics:

$$HCO_3^- + OH^- \rightleftharpoons CO_3^{2-} + H_2O \quad (K_1 = 4.66 \times 10^3\,M^{-1}) \tag{4.7}$$

$$CO_2 + OH^- \rightleftharpoons HCO_3^- \quad (K_2 = 4.44 \times 10^7\,M) \tag{4.8}$$

$$H_2O \rightleftharpoons H^+ + OH^- \quad (K_f = 10^{-14}\,M^2) \tag{4.9}$$

Here, the equilibrium constants K_1, K_2, and K_f define the strength of each reaction, determining the balance between reactants and products under equilibrium conditions (the values are taken from Sullivan et al. [152]). Due to the rapid reaction rates, these equilibria are modeled as instantaneous and thus remain continuously at equilibrium throughout the electrolyte domain. As a result, any localized perturbation in the concentration of one species (such as the consumption of CO_2 or H^+) at electrode surfaces will immediately trigger adjustments in concentrations of related species, restoring local chemical equilibrium.

Specifically, the consumption of CO_2 during the electrochemical reduction at the cathode leads to a reduction in local dissolved CO_2 concentration. Consequently, bicarbonate ions dissociate or recombine via equilibrium reactions to restore chemical balance, altering concentrations of carbonate ions, hydroxide ions and protons. Similarly, proton depletion at the cathode surface, induced by electrochemical reactions,

leads to an increase in local pH, shifting equilibrium concentrations accordingly. In this framework, equilibrium reactions play a crucial role in accurately modeling the electrolyte's chemical environment. Proper consideration of these equilibria is essential to capture realistic ionic distributions, particularly within diffusion boundary layers (DBLs) adjacent to reactive surfaces, and ensures accurate prediction of system performance and selectivity in the electrochemical reduction processes.
Lastly, the electrolyte recirculation within the model is implemented by setting the velocity field $\mathbf{u}$ in the electrolyte domain. Specifically, the y-component of the electrolyte velocity is fixed at a prescribed inflow velocity u_0, while the x-component is held at zero. This configuration establishes a controlled vertical flow, directing the electrolyte continuously from the inlet boundary toward the outlet boundary at the assigned velocity u_0.
At the inlet boundary, the concentrations of all ionic species are specified according to their equilibrium values, corresponding to conditions of CO_2 saturation. This approach ensures that the simulated electrolyte entering the reactor maintains chemical equilibrium conditions representative of a real CO_2-saturated solution. The equilibrium concentrations and corresponding diffusion coefficients utilized for each species in the simulations are detailed in Table 4.1.

Table 4.1 Diffusion coefficients at infinite dilution and initial equilibrium concentrations of ionic species at $T = 298.15\,\mathrm{K}$. Note that the concentrations of reaction products O_2, CO, and H_2 are initially set to zero. Proton concentration is calculated to achieve a bulk pH of 6.8. Reprinted with permissions under the CCA 4.0, from [150].

Species	**Diffusion coefficient** ($m^2\,s^{-1}$)	**Ref.**	**Initial equilibrium concentration** (M)	**Ref.**
CO_2	1.91×10^{-9}	[139]	0.0342	[139]
K^+	1.95×10^{-9}	[153]	0.1	–
OH^-	5.27×10^{-9}	[139]	6.6×10^{-8}	[139]
H^+	9.3×10^{-9}	[154]	1.5×10^{-7}	*Calc.*
HCO_3^-	1.10×10^{-9}	[153]	0.099	[139]
CO_3^{2-}	9.23×10^{-10}	[155]	3.1×10^{-5}	[139]
H_2	4.5×10^{-9}	[156]	0	–
CO	2.03×10^{-9}	[156]	0	–
O_2	2.10×10^{-9}	[156]	0	–

4.1.2 Membrane domain

The ion-exchange membrane used in this model, specifically Nafion 117, is represented as a porous structure characterized by fixed negative charges embedded within its polymeric matrix. This fixed-charge concentration (c_m) is significantly higher than the concentration of mobile ionic species, particularly protons. Due to these negative fixed charges, the membrane selectively allows H^+ to pass through from the anodic compartment towards the cathodic compartment, while negatively charged ions are excluded. Please note that, in the present model, the transport of K^+ through the membrane is neglected.

The selective permeability of the membrane, coupled with the fixed charge sites, results in the establishment of an electrochemical potential gradient across its thickness, known as the Donnan potential ($\Delta\Phi_d$). The Donnan potential arises specifically at the interface between the electrolyte and the membrane, where there is a discontinuity in ion concentration, and when high density of the membrane fixed charges is considered (here, c_m= 1 M) [157, 158]. This potential can be mathematically expressed by the Nernst equation as follows:

$$\Delta\Phi_d = \frac{RT}{F} \ln\left(\frac{[H^+]}{c_m}\right) \tag{4.10}$$

Subsequently, the total membrane potential Φ_m can be determined by accounting for this Donnan potential at both the anodic and cathodic interfaces of the membrane. The overall membrane potential is thus defined by the electrolyte potential (Φ_e) adjacent to each side of the membrane, corrected by subtracting the Donnan potential:

$$\Phi_m(x = x_a, x_m) = \Phi_e(x = x_a, x_m) - \Delta\Phi_d(x = x_a, x_m) \tag{4.11}$$

Here, the spatial coordinates x_a and x_m correspond to the positions of the anodic and membrane interfaces, respectively. Within the membrane domain itself, ionic current transport is modeled using Ohm's law, expressed by the relationship:

$$J_m = -\sigma_m \nabla\Phi_m \tag{4.12}$$

In this equation, J_m represents the current density passing through the membrane, and σ_m denotes the ionic conductivity of the membrane material, which in this case is taken as $12\,\mathrm{S\ m^{-1}}$ for Nafion 117. This ionic conductivity describes the ease with

which protons migrate across the membrane under the influence of the potential gradient.
Furthermore, proton transport across the membrane, which results from the imposed electric field, is directly related to the membrane current density through Faraday's law. This relationship links the molar flux of protons (N_{H^+}) through the membrane to the current density:

$$N_{H^+} = \frac{J_m}{F} \tag{4.13}$$

To ensure continuity and consistency in the mathematical formulation, boundary conditions at the membrane interfaces enforce equality between the membrane current density and the electrolyte current density normal to the membrane surface.

4.1.3 Electrodes boundaries

The electrochemical reactions within the modeled reactor take place exclusively at the electrode surfaces, specifically at the cathode and anode boundaries. The cathode catalyst is modeled as a porous cluster of Ag nanoparticles, selectively facilitating the electrochemical reduction of CO_2 into CO. Alongside this primary reaction (Eq. 4.14), the competing hydrogen evolution reaction also occurs and is incorporated within the model (Eq. 4.15). On the anodic side, only the oxygen evolution reaction is considered (Eq. 4.16), assuming that this reaction is kinetically fast enough to avoid limiting overall reactor performance. The modeled electrochemical reactions, along with their standard equilibrium potentials with respect to the RHE, are given by:

$$CO_2 + 2H^+ + 2e^- \rightleftharpoons CO + H_2O \quad (E^0 = -0.1\,\text{V vs. RHE}) \tag{4.14}$$

$$2H^+ + 2e^- \rightleftharpoons H_2 \quad (E^0 = 0\,\text{V vs. RHE}) \tag{4.15}$$

$$2H_2O \rightleftharpoons 4H^+ + 4e^- + O_2 \quad (E^0 = 1.23\,\text{V vs. RHE}) \tag{4.16}$$

Reaction selectivity towards a given product (CO or H_2) is quantified by the Faradaic efficiency, which expresses the fraction of the total electric current that contributes directly to a particular reaction. FE for the product k is mathematically defined as:

$$\text{FE}_k = \frac{j_{\text{par},k}}{J_{\text{tot}}} \times 100 \tag{4.17}$$

In this expression, $j_{\text{par},k}$ represents the partial current density related to the electrochemical reaction producing species k, while J_{tot} corresponds to the total current density passing through the reactor, obtained by summing all individual partial current densities involved:

$$J_{\text{tot}} = \sum_{k} j_{\text{par},k} \tag{4.18}$$

The partial current densities ($j_{\text{par},k}$) for each electrochemical reaction are determined using the Butler–Volmer kinetic equation, which is a set of equations widely adopted in electrochemical modeling to describe the rate of electrode reactions [159–161]. The concentration-dependent Butler–Volmer equation employed in this study is expressed as follows:

$$j_{\text{par}} = j_0 \left[C_R \exp\left(\frac{\alpha_a F}{RT}\eta\right) - C_{OX} \exp\left(-\frac{\alpha_c F}{RT}\eta\right) \right] \tag{4.19}$$

In this equation, j_0 is the exchange current density, representing the reaction's inherent kinetic activity at zero overpotential, while α_a and α_c are the anodic and cathodic charge transfer coefficients, respectively. The dimensionless terms C_R and C_{OX} represent normalized surface concentrations of the reduced and oxidized species. Specifically, for HER, both C_R and C_{OX} are unity; for OER, $C_R = 1$ and $C_{OX} = 0$; whereas for the CO_2 reduction reaction, the term C_{OX} accounts explicitly for CO_2 surface concentration as follows:

$$C_{OX} = \frac{C^s_{\text{CO}_2}}{C^*_{\text{CO}_2}} \tag{4.20}$$

Here, $C^s_{\text{CO}_2}$ denotes the surface concentration of CO_2 at the cathode, while $C^*_{\text{CO}_2}$ is its bulk equilibrium concentration. This representation enables the model to realistically capture mass-transport limitations that may occur when the consumption rate of CO_2 at the electrode surface surpasses its diffusion rate from the electrolyte bulk. The kinetic parameters applied in the model, such as exchange current densities (j_0) and charge transfer coefficients (α_a and α_c, respectively), are extracted from experimental Tafel plots and subsequently fine-tuned to match experimental observations. The resulting kinetic parameters for cell configurations with semi-cell lengths of $L = 0.6\,\text{cm}$ and $L = 0.25\,\text{cm}$ are presented in Tables 4.2 and 4.3, respectively. These slight variations highlight the dependency of electrode reaction kinetics on specific reactor geometries and configurations. Furthermore, the overpotential (η) for each

electrochemical reaction (r= eCO_2RR,HER,OER), a crucial parameter affecting the reaction rates, is defined as the deviation of the applied electrode potential (Φ_s) from the equilibrium potential of the reaction ($E_{0,r}$) and the adjacent electrolyte potential (Φ_e):

$$\eta_r = \Phi_s - E_{0,r} - \Phi_e \tag{4.21}$$

Finally, species production and consumption at the electrode surfaces are included as boundary conditions for species fluxes. These fluxes (N_i) at electrode boundaries are calculated by relating the partial current density and the species stoichiometry through Faraday's law, given as:

$$N_i = \frac{\nu_i j_{\text{par}}}{nF} \tag{4.22}$$

In this equation, ν_i denotes the stoichiometric coefficient of species i involved in the electrochemical reactions, and n represents the number of electrons transferred per reaction event, with $n = 2$ for CO and H_2 formation reactions and $n = 4$ for the O_2 evolution reaction.

Table 4.2 Kinetic parameters used for electrochemical reactions in the batch cell model at semi-cell length $L = 0.6\,\text{cm}$. Reprinted with permissions under the CCA 4.0, from [150].

Reaction	j_0 (A m^{-2})	α_c	α_a	C_R	C_{OX}
eCO_2RR	7.2×10^{-7}	0.25277	0.74723	1	$C^s_{CO_2}/C^*_{CO_2}$
HER	9.0×10^{-5}	0.14437	0.85563	1	1
OER	10.0	–	1	1	0

Table 4.3 Kinetic parameters used for electrochemical reactions in the batch cell model at semi-cell length $L = 0.25\,\text{cm}$. Reprinted with permissions under the CCA 4.0, from [150].

Reaction	j_0 (A m^{-2})	α_c	α_a	C_R	C_{OX}
CO_2RR	7.2×10^{-7}	0.23708	0.76292	1	$C^s_{CO_2}/C^*_{CO_2}$
HER	2.6×10^{-5}	0.15399	0.84601	1	1
OER	10.0	–	1	1	0

4.1.4 Time-Dependent simulation

The scope of the present model is to achieve the simulation of real-life conditions for the PV-EC device. Due to the nature of the experiment, a time-dependent simulation is necessary to reproduce the results coming from the chronoamperometry. In this case, moving from a stationary to a time-dependent domain, the species mass continuity must be rewritten, to inglobe the partial derivative of the species concentration c_i with respect to time. In particular:

$$\frac{\delta c_i}{\delta t} + \nabla \cdot J_i + u \cdot \nabla c_i = R_i \tag{4.23}$$

4.2 PV Model

The PV subsystem within the integrated PV–EC device is mathematically represented using the well-established one-diode equivalent circuit model [162]. This modeling framework provides a realistic and reliable description of the electrical behavior of solar cells under various illumination and operational conditions. The model captures both ideal photovoltaic behavior and non-ideal losses such as recombination, resistive drops, and leakage pathways.
The I-V relationship of the PV module is given by:

$$I = I_{\text{ph}} - I_0 \left[\exp\left(\frac{V + IR_s}{gV_T} \right) - 1 \right] - \frac{V + IR_s}{R_{\text{sh}}} \tag{4.24}$$

where the variables are defined as follows:

- I: output current from the PV module,
- V: voltage across the terminals of the PV module,
- I_{ph}: light-induced (photogenerated) current, directly dependent on the incident solar irradiance,
- I_0: diode saturation current, associated with minority carrier recombination,
- R_s: series resistance, which represents ohmic losses due to the internal resistance of cell materials and interconnections,

- R_{sh}: shunt resistance, modeling leakage currents through parasitic paths or defective junctions,
- g: ideality factor, describing how closely the diode behavior approximates an ideal diode (typically $1 < g < 2$),
- V_T: thermal voltage, given by $V_T = \frac{kT}{q}$, where k is Boltzmann's constant, T the absolute temperature, and q the elementary charge.

This equation encompasses two key non-ideal effects: voltage drops due to R_s and leakage currents governed by R_{sh}. Both significantly affect the maximum power point and fill factor of the PV device, and thus are crucial in predicting realistic behavior in device integration studies.

4.3 Numerical Processing

All equations presented in the previous sections were solved numerically using COMSOL Multiphysics 6.1, which employs the finite element method (FEM) to discretize and solve the governing partial differential equations across the defined computational domain. Specifically, the electrolyte region, along with the cathode and anode interfaces, was simulated using the tertiary current distribution (TCD) interface [163], which accounts comprehensively for electrochemical kinetics, concentration gradients, and electric potential distributions within the domain.
In contrast, due to the uniform concentration distribution anticipated within the ion-exchange membrane, the membrane domain was modeled using the secondary current distribution (SCD) interface [164]. The choice of mesh density and distribution was carefully validated by conducting a mesh sensitivity analysis, confirming numerical stability and ensuring that the solutions are independent of mesh discretization. To ensure numerical accuracy while maintaining computational efficiency, a structured, custom-generated mesh was employed (Fig. 4.2). Rectangular mesh elements were chosen due to their ability to precisely conform to the geometric layout of the reactor domains, allowing for optimized resolution. The mesh was refined near the critical regions such as electrode surfaces and membrane boundaries, where steep gradients in electric potential, ionic concentrations, and reaction rates are expected. Conversely, mesh elements were made coarser within the bulk regions of both cathodic and anodic compartments, where fewer variations occur, thereby

reducing computational overhead. The final computational mesh employed for simulations consisted of a total of 19,095 domain elements and 782 boundary elements.

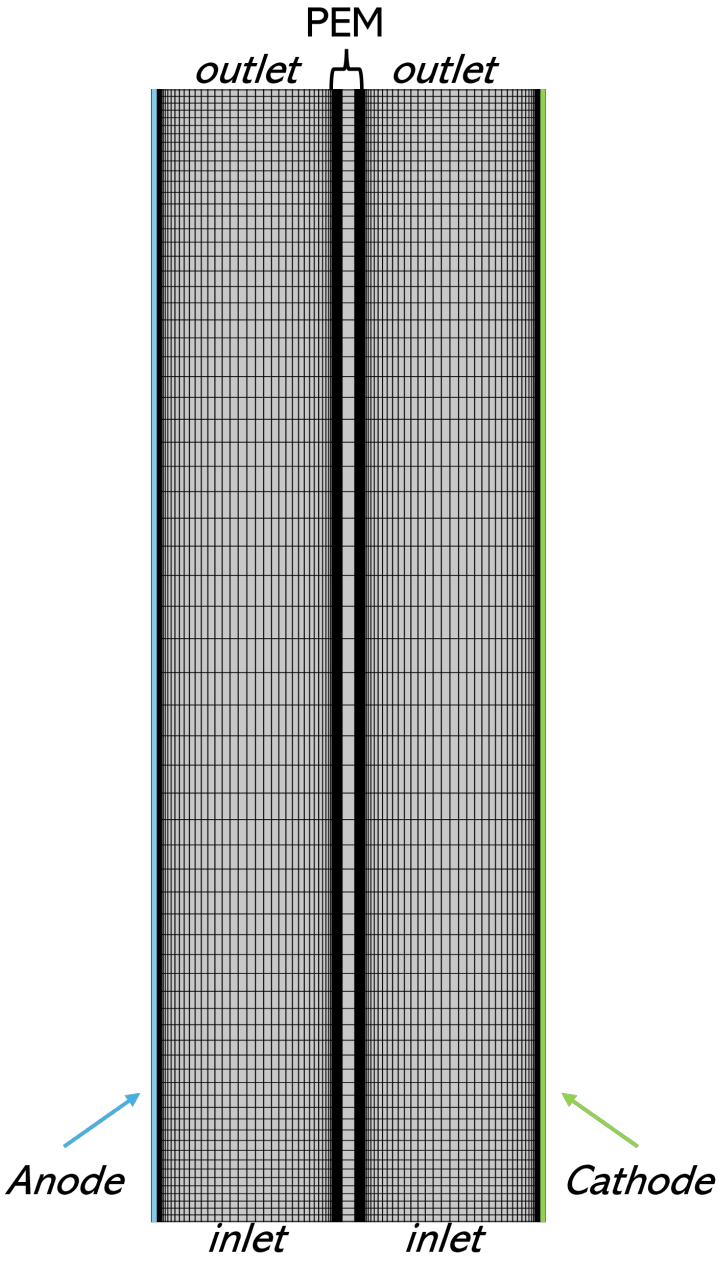

Fig. 4.2 Rectangular user-defined mesh grid of the domain for FEM solver.

Chapter 5

Results and Discussion

The main results will be described in this chapter. First of all, the CO_2 reduction and PV performance will be addressed and characterized; after that, the integration will be addressed experimentally. Finally, the model outputs will be inserted to give more useful insights on the eCO_2RR, and its applicability on the solar-driven CO_2 conversion will be demonstrated as well. Part of the work shown in this chapter has been previously published [148, 150].

5.1 Experimental Results

5.1.1 EC Characterization

The voltage-dependent selectivity towards CO production is clearly illustrated in Fig. 5.1. At relatively low applied voltages (below approximately $V_c \sim 2\,\mathrm{V}$), hydrogen evolution predominates due to the comparatively high activation overpotential required for the eCO_2RR, as shown from theoretical calculations in Section 5.2.1 (please notice that, at low voltages, it is difficult to retrieve partial current densities and FEs due to limitations in the sensitivity of the gas chromatographs and the low concentration of products). Conversely, at elevated voltages (above roughly $V_c \sim 4\,\mathrm{V}$), the system experiences limitations due to insufficient mass transport of CO_2 molecules to the cathode surface, which again promotes increased hydrogen generation. However, in the intermediate voltage range (approximately between 2 and 4 V), there is an optimal balance between the electrochemical reaction kinetics

and CO_2 diffusion to the electrode surface, thereby maximizing the efficiency of CO production. This observed trend, although sensitive to specific details of experimental configurations, aligns well with previously published studies and is broadly recognized within the scientific literature [128].

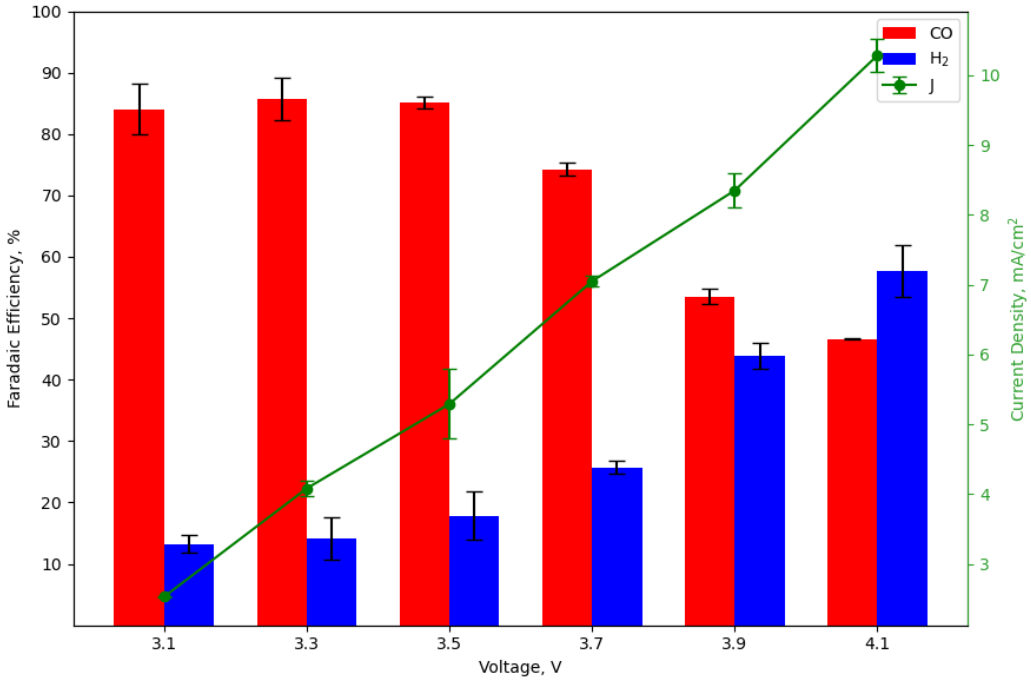

Fig. 5.1 Current density and Faradaic Efficiency for the batch cell reactor.

5.1.2 PV Characterization

As depicted in Fig. 5.2a, the I-V characteristics of the DSSC module exhibit a clear dependence on the incident light intensity. Consistent with observations reported in the literature [165], the curves systematically shift towards higher current and voltage values as the illumination intensity (expressed in SUN units) increases. Specifically, Figure 5.2b highlights the behavior of I_{SC} and V_{OC} as functions of varying incident irradiance. Both parameters increase steadily with enhanced illumination due to the intensified photogeneration of charge carriers [166]. The open-circuit voltage in DSSCs is fundamentally governed by the difference in electrochemical potential between the excited state of the dye and the conduction band of the TiO_2 semiconductor, relative to the electrolyte redox potential. When illumination inten-

sity rises, a greater number of photons are absorbed by the dye molecules, resulting in an increased population of electrons in the excited states. Consequently, more electrons are transferred from the dye into the TiO_2 conduction band, strengthening the electric field established at the interface between the semiconductor and electrolyte. This augmented electron injection elevates the electrochemical potential difference, thereby enhancing the observed open-circuit voltage.

Similarly, the short-circuit current is directly influenced by the number of electrons successfully injected into the conduction band of the TiO_2 following photon absorption by the sensitizing dye. Increased illumination leads to more absorbed photons, thus increasing the electron photogeneration rate and, consequently, the short-circuit current.

Finally, to precisely quantify and analyze the module's electrical response, the

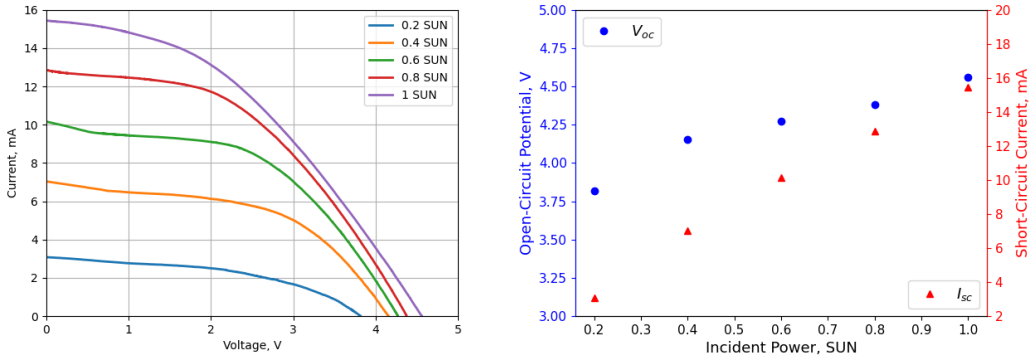

(a) (b)

Fig. 5.2 I-V characteristics (a) and short-circuit current (open-circuit potential) (b) of the DSSCs module. Reprinted with permissions under the CCA 4.0, from [148].

experimentally measured I–V curves shown in Fig. 5.2a were utilized to extract the parameters required by Equation (4.24). The resulting fitted curves, illustrated in Fig. 5.3, provide a robust and accurate mathematical representation of the DSSC module's electrical behavior under varying illumination conditions.

The obtained I–V characteristics clearly illustrate the dependency of the photovoltaic module's electrical performance on the incident illumination intensity. Notably, variations in both R_s and R_{sh} resistances as a function of illumination intensity were observed, aligning well with previously reported findings in the literature [167, 168]. Specifically, an increase in incident power leads to a notable decrease in the shunt resistance accompanied by a corresponding increase in the photogenerated current,

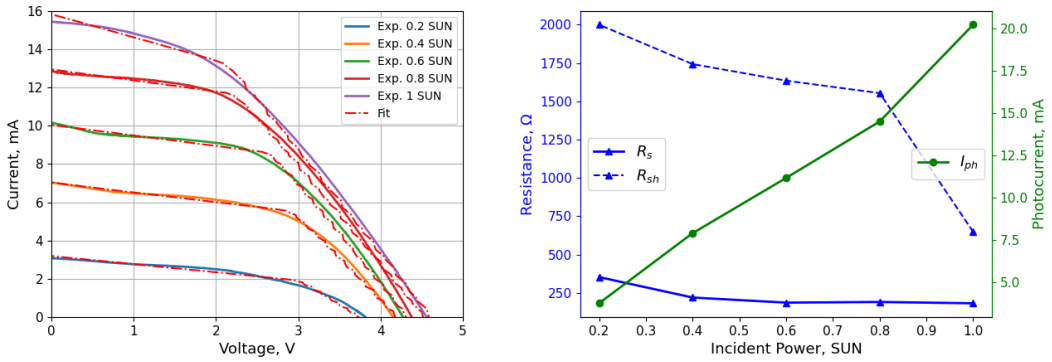

(a) (b)

Fig. 5.3 I-V characteristics fitting (a) and R_s, R_{sh}, I_{ph} trends vs. incident power (b). Reprinted with permissions under the CCA 4.0, from [148].

whereas the series resistance remains relatively stable across the examined illumination conditions.

The shunt resistance in DSSCs is predominantly influenced by recombination processes, particularly the recombination of electrons photogenerated at the photoanode with oxidized species in the electrolyte redox mediator. The observed reduction in R_{sh} at lower illumination intensities can be explained by a decreased density of photogenerated carriers within the TiO_2 semiconductor layer. Under such lower carrier densities, electrons generated in the photoanode can be more efficiently extracted and transported, reducing the overall recombination losses and thus lowering the effective shunt resistance. Additionally, the slightly reduced operating temperature of the photovoltaic module under lower illumination intensities may also contribute to diminished recombination activity, further reinforcing the observed decline in R_{sh}. Conversely, the series resistance, which primarily arises from intrinsic material properties, geometric parameters, and interconnections between individual DSSC units, shows negligible dependency on illumination levels. These series losses are primarily structural or contact-related and thus remain constant irrespective of changes in incident illumination.

Equation 4.24, completed with the numerical parameters extracted from the I-V curves fitting, was subsequently incorporated as the electrical boundary conditions within the COMSOL Multiphysics simulation environment. This integration enabled the model to accurately predict and evaluate the practical performance of the PV-EC system under realistic operational scenarios. Specifically, within the simulation, the

photovoltaic module provided the voltage and current input necessary for the electrochemical cell operation, allowing a thorough analysis of the system performance determined by the intersection between the PV module and the electrochemical cell characteristics.

5.1.3 PV-EC Integration

For the PV-EC integrated system, an essential initial step toward effective device engineering involves accurately determining the electrical operational point. Without externally imposed conditions, the operational characteristics naturally settle at the intersection of the I–V curves of the photovoltaic and electrochemical modules. As illustrated in Fig. 5.4, this intersection defines the operational point under standard illumination conditions (1 SUN) as approximately V_{op} = 3.1 V and I_{op} = 8.6 mA, corresponding to a current density of about 3.4 mA cm^{-2}. This self-equilibrating feature underscores the robustness and autonomous operation of the system, enabling it to adjust dynamically to environmental variations without the need for external electronic regulation.

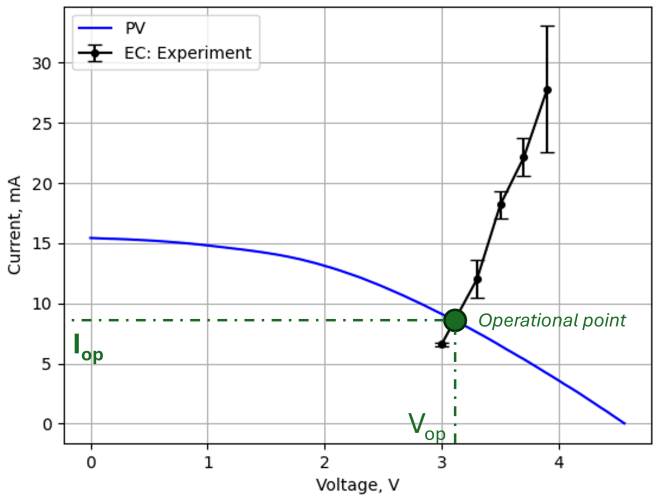

Fig. 5.4 Experimental photovoltaic (PV) cells and electrochemical cells (EC) characteristics, at a light intensity of 1 SUN.

Fig. 5.5 illustrates the solar-driven electrochemical reduction of CO_2 into CO under varying solar irradiance levels. The experimental results confirm the accurate

operational point at full solar intensity (1 SUN) and also highlight system behavior under lower irradiance conditions. At reduced illumination intensities, there is a noticeable decline in both current density and reaction selectivity toward CO_2RR (Fig. 5.5a). Interestingly, the operational voltage remains relatively stable, exhibiting only minor fluctuations within a narrow range (3.05–3.10 V) when the incident illumination decreases from 1 sun to 0.6 sun (Fig. 5.5b). This voltage stability likely arises due to the proximity of the system's operational point to the maximum power point of the photovoltaic cells, where the voltage variation is inherently minimal. Hence, even with considerable fluctuations in solar irradiance, the PV module consistently provides stable voltage output close to its optimal point.
Furthermore, the observed reduction in Faradaic efficiency at lower illumination intensities (Fig. 5.5a) indicates decreased availability of electrical energy, thus limiting electron flow and consequently diminishing the overall efficiency of the CO_2 reduction process. Notably, since no liquid-phase reaction products were detected during the experimental procedures, Faradaic efficiencies reported here exclusively reflect gaseous products, specifically H_2 and CO.

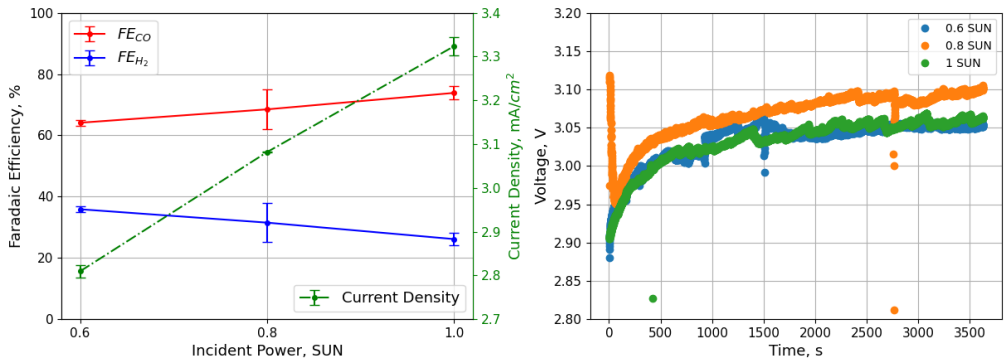

(a) (b)

Fig. 5.5 FE/current density (a) and total voltage (b) of the solar-driven CO_2 electroreduction through the PV-EC device.

5.1.4 PV-BE Characterization

The custom bicarbonate electrolyzer is characterized, and the results are reported in Fig. 5.6

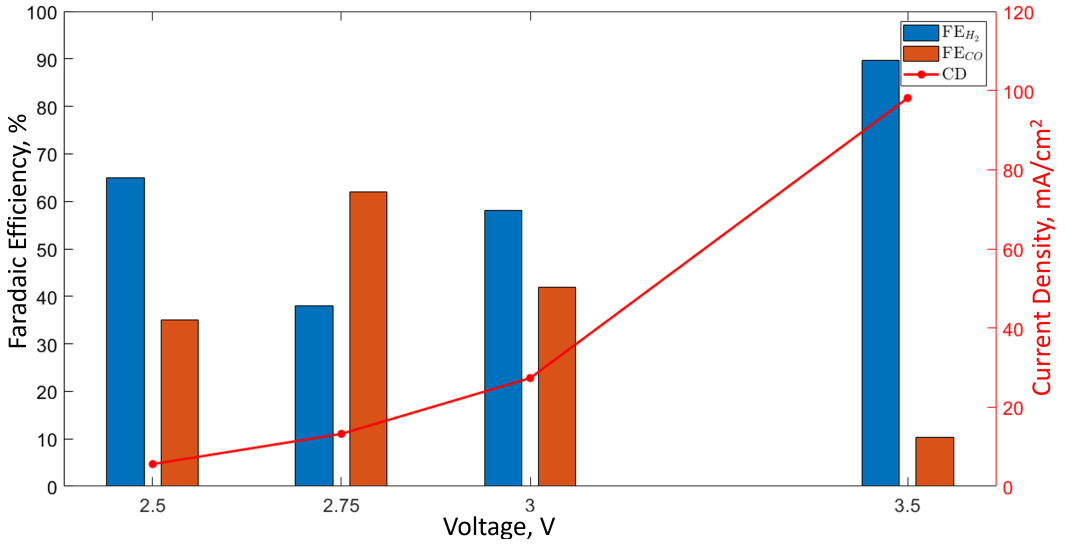

Fig. 5.6 Current density and Faradaic Efficiency for the bicarbonate electrolyzer. Reprinted from [149].

The trend indicate that intermediate overpotentials maximize CO yield, whereas both low and high voltages favor hydrogen evolution: this is likely because, at higher overpotentials and currents, competitive hydrogen evolution outpaces bicarbonate-to-CO_2 conversion and the local CO_2 supply becomes transport-limited. Consequently, operating at $\approx$ 2.75 V range offers the best compromise between rate and selectivity for CO production exploiting this bicarbonate electrolyzer.

As preliminary tests for this device, it has been studied the coupling between a module of DSSCs and the electrolyzer, without direct integration. The coupling with an ad-hoc module (different from the one previously used for the PV-EC system) shows that it is possible to obtain the point with highest efficiency from the device, as shown in Fig. 5.7.

The ideal operating point falls between 2.5 V and 2.75 V, corresponding to a current of roughly 7-8 mA. This confirms that the DSSC module can reliably power the electrolyzer under these conditions. Importantly, at 2.75 V the electrolyzer reaches its peak performance, achieving a CO Faradaic efficiency of 62%.

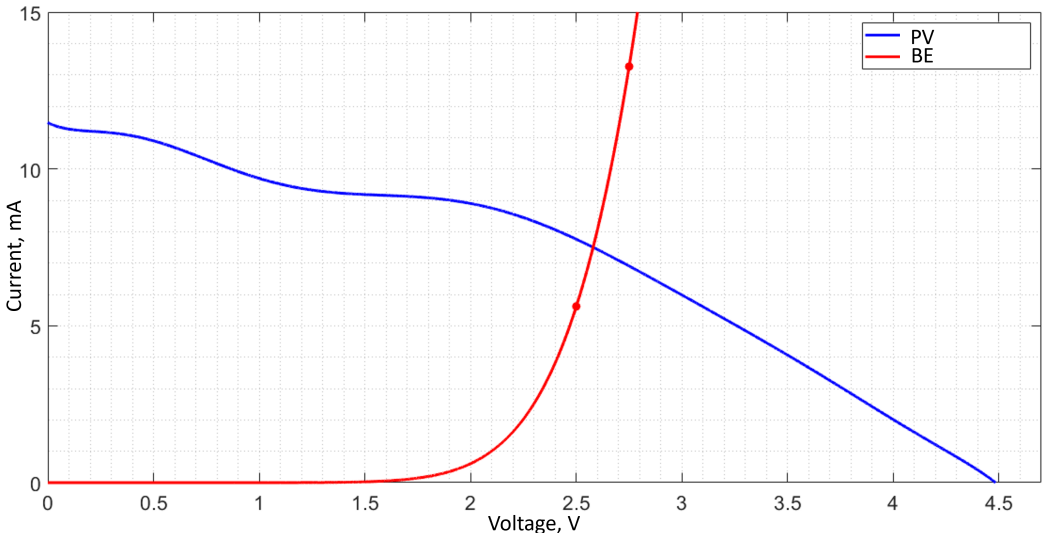

Fig. 5.7 Current density and Faradaic Efficiency for the bicarbonate electrolyzer. Reprinted from [149]

5.2 Numerical Model Results

The 2D computational model developed in this work generates results that inherently vary with both x and y spatial coordinates. To further investigate the impact of the vertical spatial coordinate, Fig. 5.8 illustrates an example of the partial current densities associated with CO and H_2 production along the y-axis. Additionally, the graph shows the corresponding average values for these current densities. In these simulations, the total height H of the cathode was consistently set to 2 cm, reflecting the actual electrode dimensions used during experimental investigations.

From Fig. 5.8, it is evident that the averaged partial current densities are generally representative of their local values along the vertical axis, with one notable exception at $y = 0$. At this position, the inlet boundary condition is imposed, causing the electrolyte solution to enter the computational domain. The instantaneous reactions occurring at this entry point cause localized increases in current density, deviating from the averaged trends observed throughout the rest of the electrode. Similar deviations near the inlet region were consistently observed for other modeled parameters, including Faradaic efficiencies, electric potentials, and concentrations of ionic species.

Despite the localized deviation observed at the electrolyte inlet boundary, the averaged values across the electrode height remain highly representative of overall system

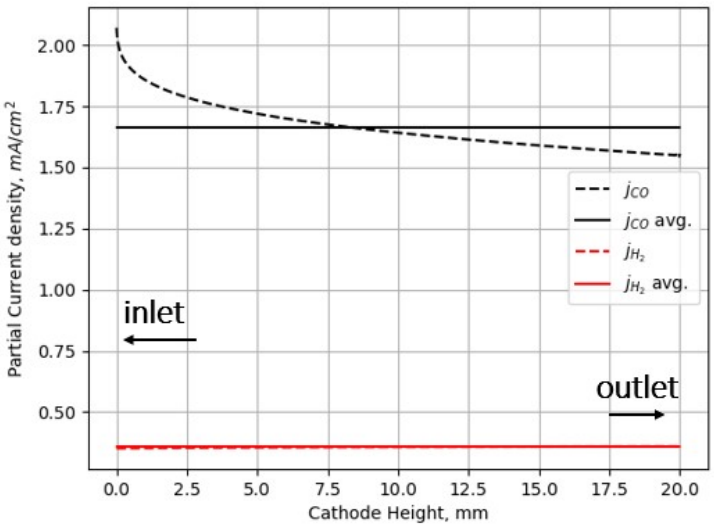

Fig. 5.8 Variation of the partial current densities of CO and H_2 on the y axis at the cathode surface, with voltage applied V_c= 3V. Straight lines report the average values, while in dashed lines the punctual values of the current densities on the cathode height are reported. Reprinted with permissions under the CCA 4.0, from [150].

behavior and effectively capture the essential trends. Consequently, in the following sections, average values across the y-axis are utilized exclusively to describe and analyze the simulation results comprehensively and succinctly.

5.2.1 Model validation

In order to verify the accuracy and reliability of the developed computational model, experimental tests on eCO_2RR were carried out and compared with the model results. Fig. 5.9 illustrates the comparison between experimentally measured and numerically simulated values for current densities and FEs for CO and H_2, presented as a function of the applied cell voltage. The analysis was performed at two distinct semi-cell lengths, specifically $L = 0.6$ cm (shown in Fig. 5.9a and 5.9c) and $L = 0.25$ cm (shown in Fig. 5.9b and 5.9d). For these experiments, the electrolyte flow velocities were set at $u_0 = 0.0057\,\mathrm{m\,s^{-1}}$ and $u_0 = 0.0067\,\mathrm{m\,s^{-1}}$ for the 0.6 cm and 0.25 cm cell configurations, respectively, corresponding in both cases to a constant volumetric flow rate of 15 mL $\mathrm{min^{-1}}$. The increased velocity in the smaller cell dimension results from maintaining a constant volumetric flow rate, where the reduced cross-sectional area inherently increases the fluid velocity entering the cell. The comparison

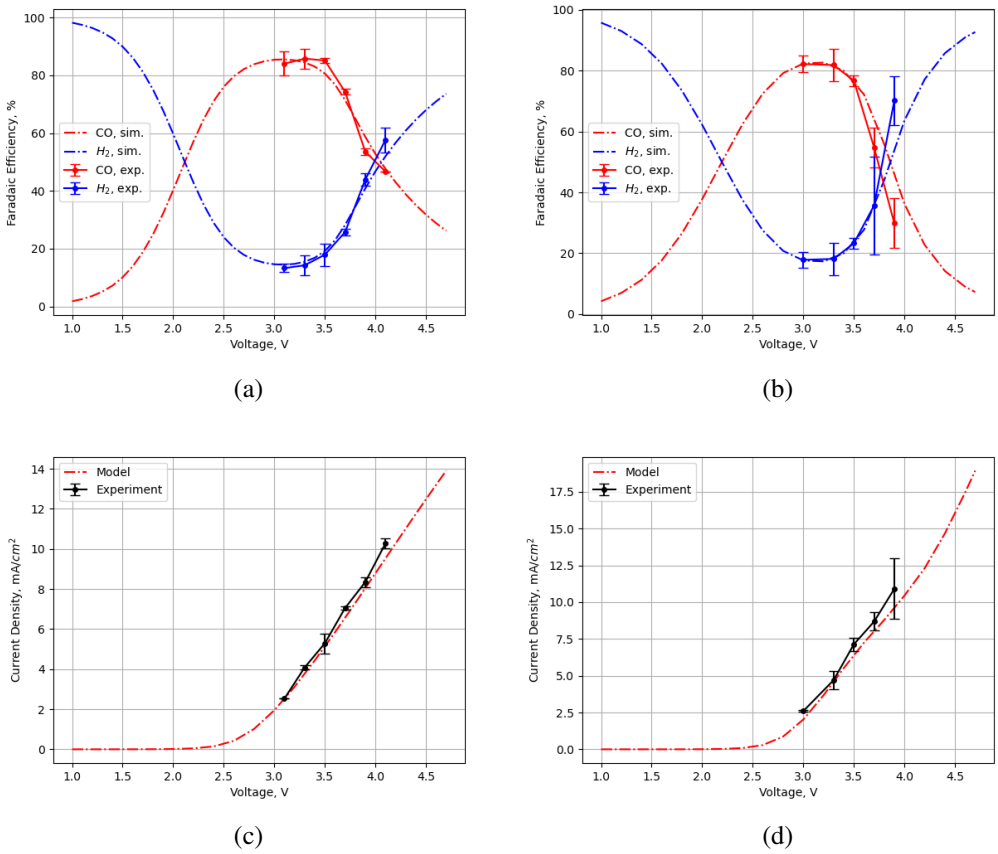

Fig. 5.9 Superimposition of model and experimental ouputs, in both Faradaic efficiencies and current densities with different semi-cell length: L = 0.6 cm (a,c) and L=0.25 cm (b,d). Reprinted with permissions under the CCA 4.0, from [150].

between experimental data and model predictions demonstrates excellent agreement across the tested voltage range. It should be noted that at lower voltages (below approximately $V_c = 3\,\text{V}$), the concentrations of reaction products become relatively low, making accurate quantification of selectivity challenging. Consequently, the presented analysis is focused primarily on experimental conditions with applied voltages of $V_c \geq 3\,\text{V}$, where the reliability of selectivity measurements is enhanced. Moreover, the computational model successfully captures variations arising from different cell lengths. For instance, as clearly depicted in Fig. 5.9d, the current density obtained with the shorter cell ($L = 0.25\,\text{cm}$) is notably higher than that of the longer cell ($L = 0.6\,\text{cm}$), as shown in Fig. 5.9c. This effect can be attributed to the reduced electrolyte resistance and enhanced ionic species migration in the shorter configuration, resulting from the shorter ionic transport pathway.

Additionally, the numerical simulations effectively reproduce the selectivity window for CO production. At relatively low applied voltages (below approximately $V_c \sim 2\,\mathrm{V}$), hydrogen evolution dominates due to the substantial activation overpotentials required to initiate eCO_2RR. At higher applied voltages (above approximately $V_c \sim 4\,\mathrm{V}$), limitations related to mass transport of CO_2 to the cathode become pronounced, once again favoring increased hydrogen generation. Conversely, an optimal region for CO production efficiency exists between about 2 and 4 V, where the reaction kinetics and the mass transport of CO_2 molecules to the cathode surface achieve a favorable balance. Although this optimal voltage window may slightly vary depending on specific experimental conditions, these observations align well with established findings reported extensively in previous literature studies [169].
Finally, it is worth noting that alterations in the cell dimension did not significantly affect the observed Faradaic efficiencies for CO and H_2, confirming the robustness of the selectivity toward CO production across different cell configurations. Given the strong correlation between experimental results and model predictions presented here, we consider our numerical model experimentally validated. Based on this validation, subsequent sections of this work utilize the validated model to explore various simulation scenarios and parameter sensitivities in greater detail.

5.2.2 Effect of the flow rate

In the computational model, to simplify the numerical treatment, all species are assumed to be dissolved in the liquid phase. Under this assumption, the rate at which CO_2 is delivered to the cathode surface can be effectively adjusted by modifying the electrolyte inflow velocity. Fig. 5.10 illustrates the impact of increasing electrolyte inflow velocities on the electrochemical cell performance, keeping the semi-cell length fixed at $L = 0.25\,\mathrm{cm}$. Consistent with previous observations reported by Wu et al. [141], a notable rise in the overall current density is observed at elevated electrolyte flow rates, as depicted in Fig. 5.10a. However, the most significant finding is the substantial widening of the voltage window wherein CO production becomes predominant, as shown clearly in Fig. 5.10b. Specifically, while the critical voltage at which Faradaic efficiency for CO production (FE_{CO}) surpasses that for hydrogen production (FE_{H_2}) remains unchanged (approximately 2.2 V), the enhancement of mass transport through increased electrolyte velocities effectively mitigates CO_2 depletion near the cathode surface. Consequently, the eCO_2RR remains kinetically

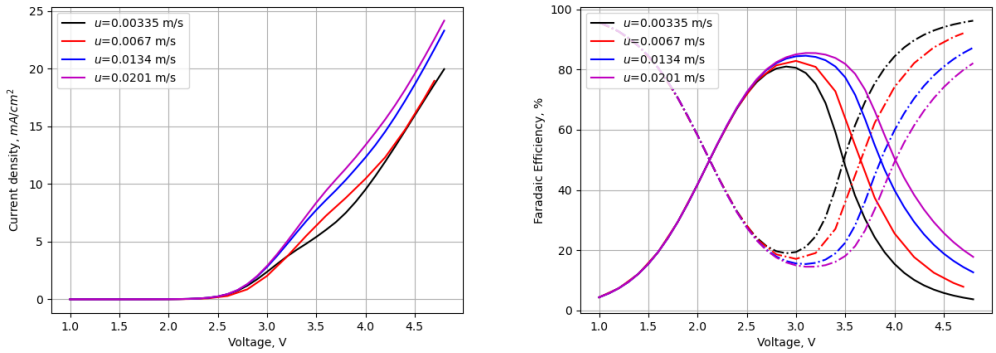

(a) (b)

Fig. 5.10 Model results of the (a) current densities and (b) faradaic efficiencies for four different inflow velocities u, as a function of the cell voltage applied, at semi-cell length of L = 0.25 cm. The dashed lines represent the FE related to HER, while straight lines represents the CO production. Reprinted with permissions under the CCA 4.0, from [150].

favored over a broader voltage range.

Further insights into this mass transport phenomenon are presented in Fig. 5.11, where the partial current densities associated with CO (j_{CO}) and H_2 (j_{H_2}) formation are plotted against varying electrolyte velocities at two representative cell voltages: $V_c = 3.0\,\text{V}$ and $V_c = 3.8\,\text{V}$.

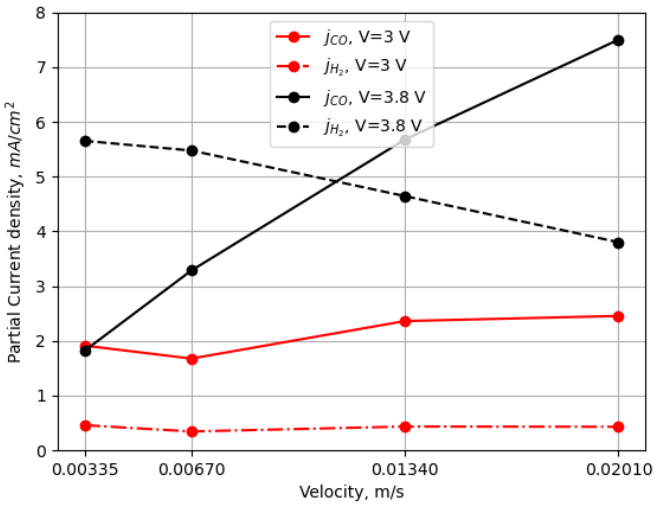

Fig. 5.11 Partial current densities of CO and H_2 production as a function of the inflow velocity, at V_c = 3 V (in red) and V_c = 4 V (in black). Reprinted with permissions under the CCA 4.0, from [150].

These plots demonstrate clearly that at higher voltages, an increased electrolyte inflow rate significantly elevates the partial current density for CO production. Concurrently, the partial current density for hydrogen evolution shows a noticeable decrease with rising electrolyte velocities. This result underscores the critical role of improved mass transport in promoting CO_2 availability at the cathode, which in turn enhances the selectivity and efficiency of the CO_2 electroreduction process.

5.2.3 Boundary Layer

Within the bulk electrolyte region, no significant variations or notable phenomena in the chemical species' concentrations are observed. Indeed, throughout most of the bulk region, the chemical environment closely matches the equilibrium conditions established at the electrolyte inlet boundary. Conversely, the boundary layer adjacent to the electrode surface, known as the diffusion boundary layer (DBL), exhibits distinct chemical behavior characterized by significant deviations from the bulk equilibrium concentrations. In this interfacial region, electrochemical reactions occur concurrently with rapid equilibrium chemical reactions, leading to substantial local concentration gradients. These concentration gradients subsequently induce diffusion-driven transport of ionic species within the boundary layer.
Fig. 5.12 presents detailed concentration profiles of various ionic species across the DBL, which extends approximately 100 µm from the electrode surface, alongside the corresponding pH variations: all data were generated at a fixed electrolyte flow velocity ($u_0 = 0.0067\,\mathrm{m\,s^{-1}}$).
At positions sufficiently distant from the cathode surface (for instance, at $x = 5.08\,\mathrm{mm}$), the electrolyte composition closely matches the initial equilibrium conditions characterized by a pH of approximately 6.8, and ionic species concentrations consistent with those specified at the domain inlet (see Table 4.1).
As the position approaches closer to the cathode surface, notable decreases in CO_2 concentration are observed (Fig. 5.12a), directly attributable to its consumption in the electrochemical reduction reaction occurring at the cathode surface. The depletion of CO_2 becomes increasingly pronounced at higher applied voltages due to elevated electrochemical reaction rates. The reduction in local CO_2 concentration at the interface triggers instantaneous adjustments of equilibrium chemical reactions described previously (reactions 4.7 - 4.9). These rapid equilibria shifts consequently alter concentrations of related ionic species, including bicarbonate (Fig. 5.12b)

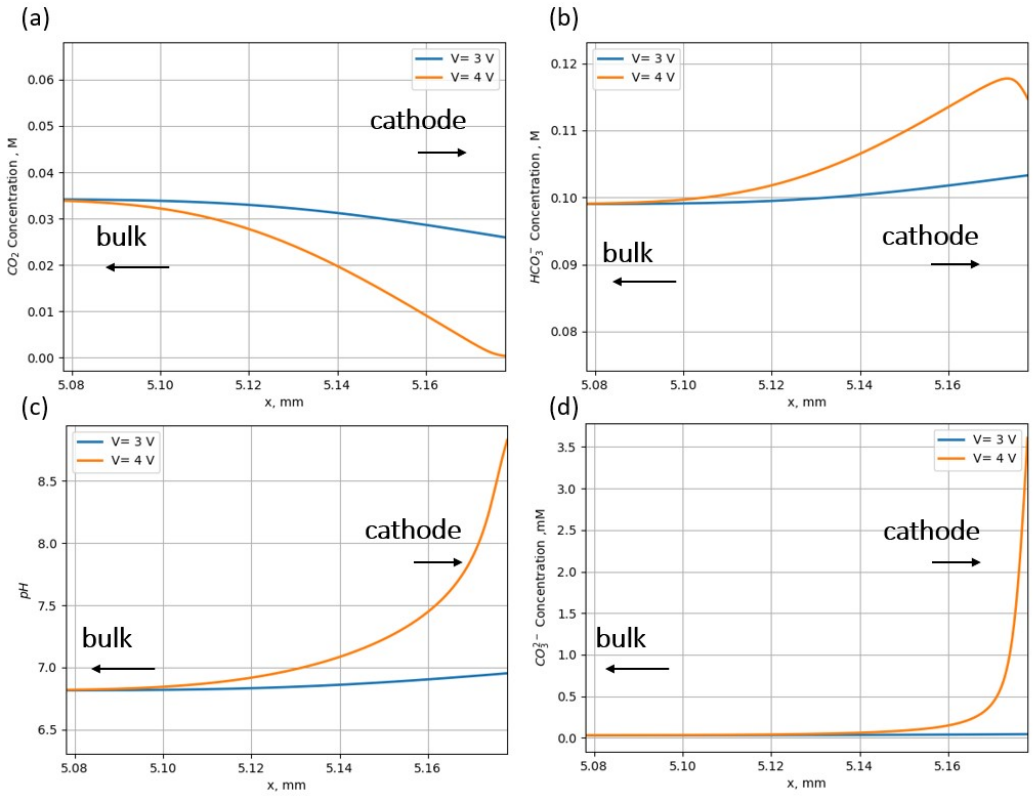

Fig. 5.12 Investigation of the local chemical environment within the diffusion boundary layer (DBL) near the cathode surface at two distinct applied voltages: $V_c = 3\,\mathrm{V}$ and $V_c = 4\,\mathrm{V}$. Reprinted with permissions under the CCA 4.0, from [150].

and carbonate ions (Fig. 5.12d), reflecting a dynamic re-equilibration to maintain chemical balance in response to CO_2 consumption.

Additionally, a notable increase in local pH is observed near the electrode interface (Fig. 5.12c), a phenomenon directly correlated with enhanced consumption of dissolved CO_2 [139, 170]. The observed rise in pH is consistent with a reduced local proton concentration and subsequent shifts in carbonate equilibrium equilibria as CO_2 is converted electrochemically to carbon monoxide.

Moreover, to further illustrate these local chemical variations at the cathode surface, Fig. 5.13a and 5.13b explicitly report the surface CO_2 concentration and the corresponding surface pH as a function of the applied cell voltage. These figures clearly demonstrate the progressive depletion of CO_2 concentration accompanied by an increase in pH at elevated voltages, confirming the significant interplay between electrochemical reactions and local chemical equilibria in the boundary-layer region.

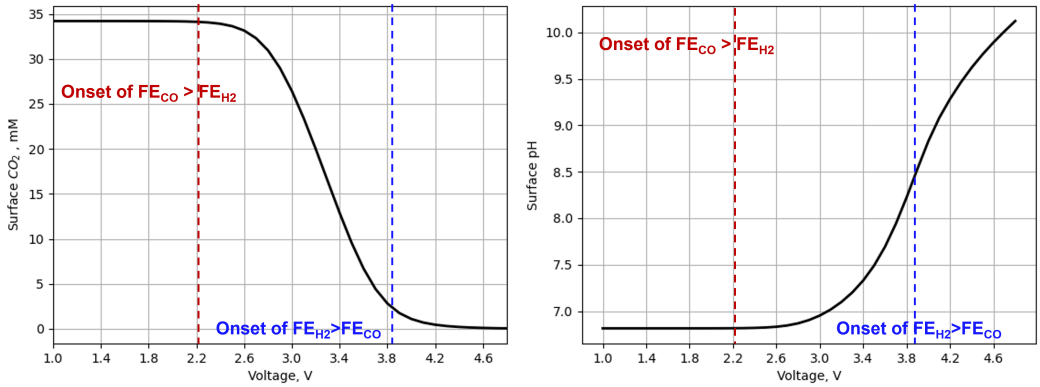

(a) (b)

Fig. 5.13 Surface concentration of CO_2 (a) and variation in surface pH (b) at the cathode as a function of the applied cell voltage. The dashed red and blue lines indicate the voltage thresholds beyond which the electrochemical reactor becomes predominantly selective towards CO and H_2 production, respectively. Reprinted with permissions under the CCA 4.0, from [150].

5.2.4 Membrane Potential

Finally, the membrane-related ohmic losses within the electrochemical cell were analyzed and characterized (Fig. 5.14). Consistent with previous modeling studies focusing on PEM fuel cells reported in the literature [171, 172], our simulations revealed a clear increase in membrane resistance(evidenced by greater voltage drops across the membrane) as both the current density and applied cell voltage increased. Interestingly, distinct differences in slopes of the membrane potential curves can be observed within voltage regions dominated either by CO or by H_2 production. It is postulated that the higher proton concentrations accumulating within membrane pores at elevated operating voltages may introduce capacitive effects. These effects potentially lead to electric field screening phenomena, thereby amplifying the observed ohmic losses in the membrane under such conditions. However, these hypotheses require additional detailed investigations and experimental validation to fully elucidate the underlying mechanisms responsible for these observed behaviors.

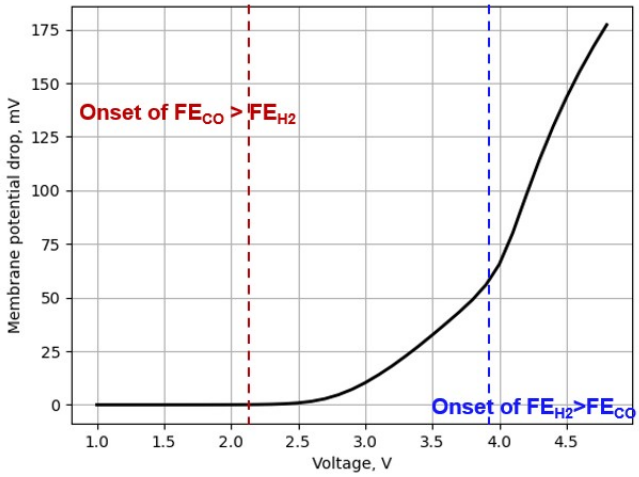

Fig. 5.14 Reprinted with permissions under the CCA 4.0, from [150].

5.2.5 Effect of Anion Exchange Membrane

It is important to highlight that significant research efforts within the scientific community have been directed towards integrating AEMs into electrochemical reactors designed for CO_2 reduction. In particular, the AEM-based reactors benefit from the transport of OH^- from the cathode to the anode compartment. This OH^- transport creates an alkaline environment near the cathode surface, effectively lowering the local proton concentration. Such alkaline conditions are advantageous for enhancing the selectivity toward the CO_2 reduction reaction by suppressing the undesired HER [69].

However, in the numerical simulations performed in this study, replacing the PEM with an AEM did not produce significant changes in reactor performance. Both current densities and Faradaic efficiencies calculated with AEMs closely matched those obtained with PEMs under identical operating conditions. These simulation outcomes align with the limited experimental data available in the literature; although a few studies have investigated the application of AEMs in batch cell configurations [173–175], none have explicitly demonstrated notable performance advantages.

This absence of measurable differences between AEM and PEM configurations in batch reactors is primarily attributable to the considerable spatial separation between the electrode surfaces and the membrane. Under such conditions, and considering that the diffusion coefficients of H^+ and OH^- are comparable, the local chemical environment near the cathode catalyst surface remains largely unaffected by the

type of ion-exchange membrane used. Consequently, the distinctive advantages of AEMs (particularly the establishment of an alkaline environment) are significantly less pronounced in batch-cell reactors.
For these reasons, the benefits of using AEMs are predominantly realized in zero-gap electrochemical cells, where electrodes are directly pressed against the membrane surface, minimizing the ionic transport distance and maximizing the influence of membrane properties on local reaction conditions at the catalyst interface.

5.2.6 PV-EC Model

The mathematical model developed in this study was validated by direct comparison with experimental results, as clearly illustrated in Fig. 5.15. A transient, time-dependent simulation was conducted to reproduce chronoamperometric behavior of the integrated PV-EC device under illumination at an intensity of 1 sun. Despite the inability of the simulation to precisely replicate the experimental transient duration and the presence of typical experimental noise, the simulated current density stabilized effectively at approximately 3.45 mA cm^{-2}. This steady-state current density showed excellent agreement with the experimentally measured value, exhibiting only a minor deviation of about 3%.
The observed discrepancy between simulated and experimental transient behaviors can be attributed to several factors. Primarily, the simplifications inherent in the mathematical model likely omit some complexities inherent to the real system. Additionally, experimental variations such as instrumental noise and measurement uncertainties inherently introduce deviations between simulated and experimental results. Furthermore, real electrochemical systems typically exhibit more intricate dynamic behaviors, including complexities related to charge-transfer kinetics, ion diffusion dynamics within the electrolyte, and various system-related delays.
Specifically, the transient response in electrochemical cells is often significantly influenced by charge-transfer phenomena at electrode interfaces and the diffusion limitations of ionic species in the electrolyte solution. Such processes inherently introduce characteristic time delays and shifts in the measured current density profiles, particularly when the system undergoes transitions from one operational state to another. The computational model employed here may not fully capture the intricate interactions between these phenomena, including the precise stabilization time required for electrochemical reactions to reach equilibrium or the characteristic

diffusion time scales associated with ionic transport. Consequently, these factors collectively explain the slight mismatch observed between experimental and simulated transient current density curves.

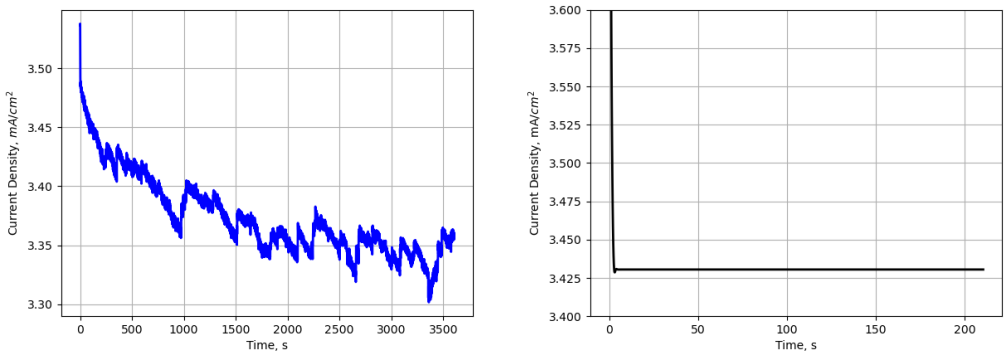

(a) (b)

Fig. 5.15 Chronoamperometric analysis of the integrated PV-EC system under an illumination intensity of 1 sun: (a) experimentally measured response, and (b) simulated response. Reprinted with permissions under the CCA 4.0, from [148].

From a modeling perspective, future implementations could incorporate additional physicochemical processes to better reproduce the experimentally observed transient behavior. In particular, accounting for gas evolution dynamics (such as bubble nucleation, growth, and detachment [176]) could be essential in systems where gaseous products (e.g., CO, H_2) form during electrochemical reactions. These phenomena are known to locally alter mass transport, reduce the effective electrode area, and induce time-dependent perturbations in the current response [177].
Moreover, integrating a dynamic surface coverage model or implementing a time-dependent effective rate constant could simulate catalyst surface restructuring, poisoning, or partial deactivation, which are plausible under sustained electrolysis conditions.
Finally, full resolution of the electric double layer and local ohmic potential variations through a Poisson–Nernst–Planck (PNP) formulation (possibly including non-equilibrium charging effects) could improve the prediction of early-time current transients [178]. Collectively, these additions would allow for a more comprehensive and physically realistic representation of transient phenomena in electrochemical CO_2 reduction systems. However, these enhancements would considerably increase the computational cost of the simulations, potentially limiting their feasibility for multidimensional (e.g., 2D or 3D) geometries or long-time dynamics.

5.3 Discussion and Outlook

An important context for evaluating the originality of this work is the long-standing debate in the solar-driven CO_2 conversion literature between two broad strategies: (i) decoupled PV-EC systems, where an external photovoltaic module supplies the electrical bias to a separately optimized electrochemical cell, and (ii) photoelectrochemical (PEC) / photocatalytic (PC) approaches, where light absorption and electrochemical conversion are combined in a single device or intimately coupled photoelectrode. PV-EC configurations offer modularity and technological maturity: the PV and electrochemical units can be designed and optimized independently, yielding robust electrical matching strategies and straightforward scaling routes (e.g., series-connection to reach the required bias). This modular approach has been explored extensively and summarized in the literature (see Section 2.2).
By contrast, PEC/PC concepts promise system-level simplification and potentially lower balance-of-system costs by merging light capture and catalysis in the same component [179]; however, PEC/PC devices still face significant challenges in materials integration and achieving high selectivity at industrially relevant current densities.
In this broader context, the present thesis wants to propose a PV-EC system in which the integration between the photovoltaic module and electrochemical cell (through the sharing of one common electrode) paves the way for scalable PV-EC devices which also benefit from the compactness of PEC systems. Moreover, the thesis wants to take a clear position in this debate: the numerics-driven evidence favors PV-EC modularity, while also probing PEC-like compactness. The trade-off, in this case, is limited by the ability to manufacture a big and efficient PV module: by increasing its active area, in fact, it can produce higher currents, enabling the use of EC modules with higher current density and productivity. In a practical real-world application, the PV-EC system could be seen as a decentralized energy-independent plant for fuel production (through CO_2 conversion), serving small energy communities.
Concerning the numerical model, its strong validation with the proposed setup makes it practical for fine tuning all the different operational parameters, and suitable for predictions also. As an example, a different electrolyte could be inserted, to check how the equilibrium reactions perform and/or the electrochemical reactions as consequence. For this purpose, it is acknowledged that a lot of experimental work must be addressed in the future, such that the model could be expanded and

reinforced with more datasets. The model and the experiments should be regarded as complementary, in a continuous exchange where one informs and strengthens the other. For instance, testing different electrochemical cell configurations would provide additional datasets to refine and validate the model, while, conversely, the model could be exploited to predict the cell behavior upon scaling up, thus guiding the design of future experiments. As a concrete example, the management of the electrolyte flow represents a crucial parameter that can be predicted by the model, together with the inlet CO_2 flow rate. On the material perspective, the model does not take into account physical properties, but it rather simplifies the catalyst to its kinetic behavior with respect to the reactions taking place. In this view, it may be seen as an engineering tool to exploit after a catalyst material has been already characterized fully, to address its integration into the overall setup.

Chapter 6

Conclusions and Future Perspectives

This thesis has explored the integration of photovoltaic systems with electrochemical CO_2 reduction devices, combining experimental investigations with mathematical modeling to evaluate and optimize solar-driven CO_2 conversion. The experimental work validated the feasibility of integrating DSSCs with an electrochemical cell for CO production, achieving promising performance under simulated solar irradiance. Complementarily, the developed mathematical model provided predictive insights into key parameters, including the influence of electrolyte flow rate, membrane properties, and system dimensions on current density and Faradaic efficiency. The close agreement between experimental results and simulation outputs underscores the robustness of the modeling approach and its potential as a tool for guiding system optimization.

The integration of renewable energy harvesting and carbon utilization demonstrated in this study contributes to the growing field of sustainable chemical production, offering a pathway toward carbon-neutral energy systems. By establishing a synergistic relationship between photovoltaic and electrochemical technologies, this work highlights the viability of decentralized, solar-driven CO_2 conversion units for distributed chemical synthesis.

Furthermore, a preliminary study has been conducted to study the feasibility of PV-BE systems, in which the CO_2 is not fluxed directly inside but rather introduced as dissolved bicarbonate in the catholyte, allowing in situ generation of CO_2 at the Ag catalyst surface and subsequent reduction to CO under the bias supplied by the photovoltaic module. In this case, the bicarbonate solution is the same one used for the CO_2 capture, avoiding the separation costs of the inlet flue gas in view of

industrialization techno-economical studies.

Despite these advancements, several challenges and opportunities remain for future exploration. At the material level, further improvements in catalyst selectivity and stability are critical to enhance CO_2 conversion efficiency and reduce competing side reactions such as the hydrogen evolution reaction. Furthermore, the employment of novel catalysts could access to more valuable products, thus making the PV-EC system an efficient Solar-to-C_+ platform. In this context, copper-based or bimetallic systems could unlock multi-carbon products, including ethylene, ethanol, or acetate. These pathways, however, would necessitate tailored designs (e.g. optimization of the local pH environment) which can be led by the numerical findings of the modeling proposed, and techno-economic studies to assess the economical feasibility of the product. Similarly, optimizing the photoabsorber components (whether through advanced DSSC designs or alternative photovoltaic technologies) could improve overall energy conversion efficiency and reduce system costs.

From a systems engineering perspective, scaling the PV-EC and PV-BE integrations from laboratory-scale to industrial relevance involves several engineering and economic challenges. These include ensuring long-term stability under continuous operation, mitigating catalyst degradation, and maintaining electrolyte balance over extended periods. The cost-effectiveness of key components (such as catalysts, membranes, and photoabsorbers) remains a decisive factor for commercialization. In parallel, the inherent intermittency of solar energy input calls for reliable energy storage or buffer systems (e.g., batteries, hydrogen storage, or capacitive storage) and smart control strategies to manage dynamic operation while maintaining steady conversion performance.

Future research could also benefit from expanding the mathematical modeling framework to incorporate multi-physics interactions, including thermal management, gas-liquid mass transfer, and long-term degradation phenomena. Such comprehensive models could facilitate techno-economic analyses, supporting the identification of optimal design configurations and operational strategies for large-scale deployment.

In conclusion, this work lays the groundwork for the development of integrated photovoltaic-electrochemical platforms for sustainable CO_2 conversion. Continued interdisciplinary efforts across materials science, electrochemical engineering, and systems modeling will be essential to advance these technologies from proof-of-concept toward practical implementation, contributing to global decarbonization and the transition to a circular carbon economy.

References

[1] John Houghton. Global warming. *Reports on Progress in Physics*, 68(6):1343, may 2005.

[2] Hermann Harde. Scrutinizing the carbon cycle and CO_2 residence time in the atmosphere. *Global and Planetary Change*, 152:19–26, 2017.

[3] John Cook, Dana Nuccitelli, Sarah A Green, Mark Richardson, Bärbel Winkler, Rob Painting, Robert Way, Peter Jacobs, and Andrew Skuce. Quantifying the consensus on anthropogenic global warming in the scientific literature. *Environmental Research Letters*, 8(2):024024, may 2013.

[4] European Commission. 2030 climate and energy framework, 2020.

[5] European Commission. Cop26 conclusion, 2021.

[6] Huiwen Lin, Shunqin Luo, Huabin Zhang, and Jinhua Ye. Toward solar-driven carbon recycling. *Joule*, 6(2):294–314, 2022.

[7] Francisco W. S. Lucas, R. Gary Grim, Sean A. Tacey, Courtney A. Downes, Joseph Hasse, Alex M. Roman, Carrie A. Farberow, Joshua A. Schaidle, and Adam Holewinski. Electrochemical routes for the valorization of biomass-derived feedstocks: From chemistry to application. *ACS Energy Letters*, 6(4):1205–1270, 2021.

[8] Chi Chen, Juliet F. Khosrowabadi Kotyk, and Stafford W. Sheehan. Progress toward commercial application of electrochemical carbon dioxide reduction. *Chem*, 4(11):2571–2586, 2018.

[9] Qi Lu and Feng Jiao. Electrochemical CO_2 reduction: Electrocatalyst, reaction mechanism, and process engineering. *Nano Energy*, 29:439–456, 2016. Electrocatalysis.

[10] Canan Karakaya and James Parks. Thermochemical processes for CO_2 hydrogenation to fuels and chemicals: Challenges and opportunities. *Applications in Energy and Combustion Science*, 15:100171, 2023.

[11] Nikhil Dhabarde, Josephine Selvaraj, Afdhal Yuda, Anand Kumar, and Vaidyanathan Ravi Subramanian. Review of photocatalytic and photo-electrocatalytic reduction of CO_2 on carbon supported films. *International*

Journal of Hydrogen Energy, 47(72):30908–30936, 2022. Advanced Technologies for Hydrogen Production Towards Green Applications.

[12] Josep Albero, Yong Peng, and Hermenegildo García. Photocatalytic CO_2 reduction to c2+ products. *ACS Catalysis*, 10(10):5734–5749, 2020.

[13] S. R. Lingampalli, Mohd Monis Ayyub, and C. N. R. Rao. Recent progress in the photocatalytic reduction of carbon dioxide. *ACS Omega*, 2(6):2740–2748, 2017. PMID: 31457612.

[14] Ayesha Nisar, Sawar Khan, Muddassar Hameed, Alisha Nisar, Habib Ahmad, and Sardar Azhar Mehmood. Bio-conversion of CO_2 into biofuels and other value-added chemicals via metabolic engineering. *Microbiological Research*, 251:126813, 2021.

[15] Kyuhyun Kim, Donghyun Kim, Yoonsu Na, Youngsoo Song, and Jihoon Wang. A review of carbon mineralization mechanism during geological CO_2 storage. *Heliyon*, 9(12):e23135, 2023.

[16] Debjyoti Ray, Pengxian Ye, Jimmy C. Yu, and Chunshan Song. Recent progress in plasma-catalytic conversion of CO_2 to chemicals and fuels. *Catalysis Today*, 423:113973, 2023.

[17] Annemie Bogaerts and Gabriele Centi. Plasma technology for CO_2 conversion: A personal perspective on prospects and gaps. *Frontiers in Energy Research*, 8, 2020.

[18] Matthew Jouny, Wesley Luc, and Feng Jiao. General techno-economic analysis of CO_2 electrolysis systems. *Industrial & Engineering Chemistry Research*, 57(6):2165–2177, 2018.

[19] Md Golam Kibria, Jonathan P. Edwards, Christine M. Gabardo, Cao-Thang Dinh, Ali Seifitokaldani, David Sinton, and Edward H. Sargent. Electrochemical CO_2 reduction into chemical feedstocks: From mechanistic electrocatalysis models to system design. *Advanced Materials*, 31(31):1807166, 2019.

[20] Jürgen Bierhals. *Carbon Monoxide*. John Wiley and Sons, Ltd, 2001.

[21] P. Biloen and W.M.H. Sachtler. Mechanism of hydrocarbon synthesis over fischer-tropsch catalysts. volume 30 of *Advances in Catalysis*, pages 165–216. Academic Press, 1981.

[22] Ftwi Yohaness Hagos, A. Rashid A. Aziz, and Shaharin Anwar Sulaiman. Trends of syngas as a fuel in internal combustion engines. *Advances in Mechanical Engineering*, 6:401587, 2014.

[23] Song Lu, Fengliu Lou, and Zhixin Yu. Recent progress in two-dimensional materials for electrocatalytic CO_2 reduction. *Catalysts*, 12(2), 2022.

[24] Wenjun Zhang, Yi Hu, Lianbo Ma, Guoyin Zhu, Yanrong Wang, Xiaolan Xue, Renpeng Chen, Songyuan Yang, and Zhong Jin. Progress and perspective of electrocatalytic CO_2 reduction for renewable carbonaceous fuels and chemicals. *Advanced Science*, 5(1):1700275, 2018.

[25] Xin Zhao, Lijie Du, Bo You, and Yujie Sun. Integrated design for electrocatalytic carbon dioxide reduction. *Catal. Sci. Technol.*, 10:2711–2720, 2020.

[26] Sujat Sen, Steven M Brown, Mclain Leonard, and Fikile R Brushett. Electroreduction of carbon dioxide to formate at high current densities using tin and tin oxide gas diffusion electrodes. *Journal of Applied Electrochemistry*, 49(9):917–928, sep 2019.

[27] Md Golam Kibria, Jonathan P. Edwards, Christine M. Gabardo, Cao-Thang Dinh, Ali Seifitokaldani, David Sinton, and Edward H. Sargent. Electrochemical CO_2 reduction into chemical feedstocks: From mechanistic electrocatalysis models to system design. *Advanced Materials*, 31(31):1807166, 2019.

[28] Allen J. Bard and Larry R. Faulkner. *Electrochemical Methods: Fundamentals and Applications, 2nd Edition*. Wiley, 2000.

[29] Wonhee Lee Hyungseob Lim Youngkook Kwon Mi-Young Lee, Ki Tae Park and Seoktae Kang. Current achievements and the future direction of electrochemical CO_2 reduction: A short review. *Critical Reviews in Environmental Science and Technology*, 50(8):769–815, 2020.

[30] D. Masheder M. N. Mahmood and C. J. Harty. Use of gas-diffusion electrodes for high-rate electrochemical reduction of carbon dioxide. i. reduction at lead, indium- and tin-impregnated electrodes. *Journal of Applied Electrochemistry*, 17(6):1159–1170, nov 1987.

[31] Jacob Schneider, Hongfei Jia, James T. Muckerman, and Etsuko Fujita. Thermodynamics and kinetics of CO_2, co, and h+ binding to the metal centre of CO_2 reduction catalysts. *Chem. Soc. Rev.*, 41:2036–2051, 2012.

[32] Jeremy T. Feaster, Chuan Shi, Etosha R. Cave, Toru Hatsukade, David N. Abram, Kendra P. Kuhl, Christopher Hahn, Jens K. Nørskov, and Thomas F. Jaramillo. Understanding selectivity for the electrochemical reduction of carbon dioxide to formic acid and carbon monoxide on metal electrodes. *ACS Catalysis*, 7(7):4822–4827, 2017.

[33] Xiaodong Li, Shumin Wang, Li Li, Yongfu Sun, and Yi Xie. Progress and perspective for in situ studies of CO_2 reduction. *Journal of the American Chemical Society*, 142(21):9567–9581, 2020. PMID: 32357008.

[34] Esperanza Sedano Varo, Rikke Egeberg Tankard, Joakim Kryger-Baggesen, Joerg Jinschek, Stig Helveg, Ib Chorkendorff, Christian Danvad Damsgaard, and Jakob Kibsgaard. Gold nanoparticles for CO_2 electroreduction: An

optimum defined by size and shape. *Journal of the American Chemical Society*, 146(3):2015–2023, 2024. PMID: 38196113.

[35] Xinwei Zhu, Jun Huang, and Michael Eikerling. Electrochemical CO_2 reduction at silver from a local perspective. *ACS Catalysis*, 11(23):14521–14532, 2021.

[36] Maor F. Baruch, James E. III Pander, James L. White, and Andrew B. Bocarsly. Mechanistic insights into the reduction of CO_2 on tin electrodes using in situ atr-ir spectroscopy. *ACS Catalysis*, 5(5):3148–3156, 2015.

[37] Stephanie Nitopi, Erlend Bertheussen, Soren B. Scott, Xinyan Liu, Albert K. Engstfeld, Sebastian Horch, Brian Seger, Ifan E. L. Stephens, Karen Chan, Christopher Hahn, Jens K. Nørskov, Thomas F. Jaramillo, and Ib Chorkendorff. Progress and perspectives of electrochemical CO_2 reduction on copper in aqueous electrolyte. *Chemical Reviews*, 119(12):7610–7672, 2019. PMID: 31117420.

[38] Seo Young Yang, Ju Young Maeng, Seon Young Hwang, Go Eun Park, Choong Kyun Rhee, and Youngku Sohn. Electrochemical CO_2 reduction on tin and its alloys: Insights from depth-profiling x-ray photoelectron spectroscopy. *Journal of Alloys and Compounds*, 960:170903, 2023.

[39] N.S. Shaikh, J.S. Shaikh, V. Márquez, S.C. Pathan, S.S. Mali, J.V. Patil, C.K. Hong, P. Kanjanaboos, O. Fontaine, A. Tiwari, S. Praserthdam, and P. Praserthdam. New perspectives, rational designs, and engineering of tin (sn)-based materials for electrochemical CO_2 reduction. *Materials Today Sustainability*, 22:100384, 2023.

[40] Wangxiang Ye, Xiaolin Guo, and Tingli Ma. A review on electrochemical synthesized copper-based catalysts for electrochemical reduction of CO_2 to c2+ products. *Chemical Engineering Journal*, 414:128825, 2021.

[41] Da Li, Linlin Huang, Yan Tian, Tongtong Liu, Liang Zhen, and Yujie Feng. Facile synthesis of porous cu-sn alloy electrode with prior selectivity of formate in a wide potential range for CO_2 electrochemical reduction. *Applied Catalysis B: Environmental*, 292:120119, 2021.

[42] Kuan-Guan Liu, Fahime Bigdeli, Akram Panjehpour, Afsanehsadat Larimi, Ali Morsali, Amarajothi Dhakshinamoorthy, and Hermenegildo Garcia. Metal organic framework composites for reduction of CO_2. *Coordination Chemistry Reviews*, 493:215257, 2023.

[43] Denise Narváez-Celada and Ana Sofia Varela. CO_2 electrochemical reduction on metal–organic framework catalysts: current status and future directions. *J. Mater. Chem. A*, 10:5899–5917, 2022.

[44] Hani Taleshi Ahangari, Thibault Portail, and Aaron T. Marshall. Comparing the electrocatalytic reduction of CO_2 to co on gold cathodes in batch and

continuous flow electrochemical cells. *Electrochemistry Communications*, 101:78–81, 2019.

[45] David Raciti, Mark Mao, Jun Ha Park, and Chao Wang. Local ph effect in the CO_2 reduction reaction on high-surface-area copper electrocatalysts. *Journal of The Electrochemical Society*, 165(10):F799, jul 2018.

[46] Dunfeng Gao, Jing Wang, Haihua Wu, Xiaole Jiang, Shu Miao, Guoxiong Wang, and Xinhe Bao. ph effect on electrocatalytic reduction of CO_2 over pd and pt nanoparticles. *Electrochemistry Communications*, 55:1–5, 2015.

[47] Ana Sofia Varela. The importance of ph in controlling the selectivity of the electrochemical CO_2 reduction. *Current Opinion in Green and Sustainable Chemistry*, 26:100371, 2020.

[48] Qiu Jianping, Tang Juntao, Shen Jie, Wu Cuiwei, Qian Mengqian, He Zhiqiao, Chen Jianmeng, and Shuang Song. Preparation of a silver electrode with a three-dimensional surface and its performance in the electrochemical reduction of carbon dioxide. *Electrochimica Acta*, 203:99–108, 2016.

[49] Y. Hori, H. Konishi, T. Futamura, A. Murata, O. Koga, H. Sakurai, and K. Oguma. "deactivation of copper electrode" in electrochemical reduction of CO_2. *Electrochimica Acta*, 50(27):5354–5369, 2005.

[50] R. Kostecki and J. Augustynski. Electrochemical reduction of CO_2 at an activated silver electrode. *Berichte der Bunsengesellschaft für physikalische Chemie*, 98(12):1510–1515, 1994.

[51] Marilia Moura de Salles Pupo and Ruud Kortlever. Electrolyte effects on the electrochemical reduction of CO_2. *ChemPhysChem*, 20(22):2926–2935, 2019.

[52] E. Irtem, T. Andreu, A. Parra, M. D. Hernández-Alonso, S. García-Rodríguez, J. M. Riesco-García, G. Penelas-Pérez, and J. R. Morante. Low-energy formate production from CO_2 electroreduction using electrodeposited tin on gde. *J. Mater. Chem. A*, 4:13582–13588, 2016.

[53] Yoshio Hori. *CO_2 Reduction Using Electrochemical Approach*, pages 191–211. Springer International Publishing, Cha, 2016.

[54] Maximilian König, Jan Vaes, Elias Klemm, and Deepak Pant. Solvents and supporting electrolytes in the electrocatalytic reduction of CO_2. *iScience*, 19:135–160, 2019.

[55] Giulia Marcandalli, Matias Villalba, and Marc T. M. Koper. The importance of acid–base equilibria in bicarbonate electrolytes for CO_2 electrochemical reduction and co reoxidation studied on au(hkl) electrodes. *Langmuir*, 37(18):5707–5716, 2021. PMID: 33913319.

[56] Ana Sofia Varela, Matthias Kroschel, Tobias Reier, and Peter Strasser. Controlling the selectivity of CO_2 electroreduction on copper: The effect of the electrolyte concentration and the importance of the local ph. *Catalysis Today*, 260:8–13, 2016. Surface Analysis and Dynamics (SAND).

[57] Ryszard Pohorecki and Wadysaw Moniuk. Kinetics of reaction between carbon dioxide and hydroxyl ions in aqueous electrolyte solutions. *Chemical Engineering Science*, 43(7):1677–1684, 1988.

[58] Sumit Verma, Xun Lu, Sichao Ma, Richard I. Masel, and Paul J. A. Kenis. The effect of electrolyte composition on the electroreduction of CO_2 to co on ag based gas diffusion electrode. *Phys. Chem. Chem. Phys.*, 18:7075–7084, 2016.

[59] Maria Rodrigues Pinto, Rafaël E. Vos, Raphael Nagao, and Marc T. M. Koper. Electrolyte effects on electrochemical CO_2 reduction reaction at sn metallic electrode. *The Journal of Physical Chemistry C*, 128(50):21421–21429, 2024.

[60] Eduardo Arizono dos Reis, Gelson T. S. T. da Silva, Elisabete I. Santiago, and Caue Ribeiro. Revisiting electrocatalytic CO_2 reduction in nonaqueous media: Promoting CO_2 recycling in organic molecules by controlling h2 evolution. *Energy Technology*, 11(6):2201367, 2023.

[61] Maximilian König, Jan Vaes, Elias Klemm, and Deepak Pant. Solvents and supporting electrolytes in the electrocatalytic reduction of CO_2. *iScience*, 19:135–160, 2019.

[62] Padmanabh B. Joshi, Nawaraj Karki, and Andrew J. Wilson. Electrocatalytic CO_2 reduction in acetonitrile enhanced by the local environment and mass transport of h2o. *ACS Energy Letters*, 7(2):602–609, 2022.

[63] Ashok Kumar, Rohit Gupta, Vasudevan Subramaniyan, and Ganesan Mani. Dmso-catalyzed CO_2 reduction with 9-bbn: selective formation of either formoxy- or methoxyborane under mild conditions and c-methylenation of indoles. *Catal. Sci. Technol.*, 15:678–688, 2025.

[64] Orest Kuntyi, Galyna Zozulya, and Mariana Shepida. CO_2 electroreduction in organic aprotic solvents: A mini review. *Journal of Chemistry*, 2022(1):1306688, 2022.

[65] Fangfang Li, Francesca Mocci, Xiangping Zhang, Xiaoyan Ji, and Aatto Laaksonen. Ionic liquids for CO_2 electrochemical reduction. *Chinese Journal of Chemical Engineering*, 31:75–93, 2021. Frontiers of Chemical Engineering Thermodynamics.

[66] Brian A. Rosen, Amin Salehi-Khojin, Michael R. Thorson, Wei Zhu, Devin T. Whipple, Paul J. A. Kenis, and Richard I. Masel. Ionic liquid-mediated selective conversion of CO_2 to co at low overpotentials. *Science*, 334(6056):643–644, 2011.

[67] Rachael J Barla, Smita Raghuvanshi, and Suresh Gupta. Chapter 10 - process integration for the biodiesel production from biomitigation of flue gases. In Bhaskar Singh and Abhishek Guldhe, editors, *Waste and Biodiesel*, pages 191–215. Elsevier, 2022.

[68] Qian Sun, Yong Zhao, Wenhao Ren, and Chuan Zhao. Electroreduction of low concentration CO_2 at atomically dispersed ni-n-c catalysts with nanoconfined ionic liquids. *Applied Catalysis B: Environmental*, 304:120963, 2022.

[69] Faezeh Habibzadeh, Peter Mardle, Nana Zhao, Harry D Riley, Danielle A Salvatore, Curtis P Berlinguette, Steven Holdcroft, and Zhiqing Shi. Ion exchange membranes in electrochemical CO_2 reduction processes. *Electrochemical Energy Reviews*, 6(1):26, jul 2023.

[70] Joaquin Resasco, Leanne D. Chen, Ezra Clark, Charlie Tsai, Christopher Hahn, Thomas F. Jaramillo, Karen Chan, and Alexis T. Bell. Promoter effects of alkali metal cations on the electrochemical reduction of carbon dioxide. *Journal of the American Chemical Society*, 139(32):11277–11287, 2017. PMID: 28738673.

[71] Stefan Ringe, Ezra L. Clark, Joaquin Resasco, Amber Walton, Brian Seger, Alexis T. Bell, and Karen Chan. Understanding cation effects in electrochemical CO_2 reduction. *Energy Environ. Sci.*, 12:3001–3014, 2019.

[72] Ning Wang, Rui Kai Miao, Geonhui Lee, Alberto Vomiero, David Sinton, Alexander H. Ip, Hongyan Liang, and Edward H. Sargent. Suppressing the liquid product crossover in electrochemical CO_2 reduction. *SmartMat*, 2(1):12–16, 2021.

[73] T Tschinder, T Schaffer, S D Fraser, and V Hacker. Electro-osmotic drag of methanol in proton exchange membranes. *Journal of Applied Electrochemistry*, 37(6):711–716, jun 2007.

[74] S.A. Grigoriev, K.A. Dzhus, D.G. Bessarabov, and P. Millet. Failure of pem water electrolysis cells: Case study involving anode dissolution and membrane thinning. *International Journal of Hydrogen Energy*, 39(35):20440–20446, 2014.

[75] Emmanuel Ogungbemi, Oluwatosin Ijaodola, F.N. Khatib, Tabbi Wilberforce, Zaki El Hassan, James Thompson, Mohamad Ramadan, and A.G. Olabi. Fuel cell membranes – pros and cons. *Energy*, 172:155–172, 2019.

[76] Ying Hou, Yu-Lin Liang, Peng-Chao Shi, Yuan-Biao Huang, and Rong Cao. Atomically dispersed ni species on n-doped carbon nanotubes for electroreduction of CO_2 with nearly 100% co selectivity. *Applied Catalysis B: Environmental*, 271:118929, 2020.

[77] Yuan Zhou, Rui Zhou, Xiaorong Zhu, Na Han, Bin Song, Tongchao Liu, Guangzhi Hu, Yafei Li, Jun Lu, and Yanguang Li. Mesoporous pdag

nanospheres for stable electrochemical CO_2 reduction to formate. *Advanced Materials*, 32(30):2000992, 2020.

[78] Tiehuai Li and Minhua Shao. A minireview on electrochemical CO_2 conversion based on carbonate/bicarbonate media. *EES Catal.*, 2:564–572, 2024.

[79] Dongguo Li, Andrew R. Motz, Chulsung Bae, Cy Fujimoto, Gaoqiang Yang, Feng-Yuan Zhang, Katherine E. Ayers, and Yu Seung Kim. Durability of anion exchange membrane water electrolyzers. *Energy Environ. Sci.*, 14:3393–3419, 2021.

[80] Peter Mardle, Simon Cassegrain, Faezeh Habibzadeh, Zhiqing Shi, and Steven Holdcroft. Carbonate ion crossover in zero-gap, koh anolyte CO_2 electrolysis. *The Journal of Physical Chemistry C*, 125(46):25446–25454, 2021.

[81] Ming Ma, Sangkuk Kim, Ib Chorkendorff, and Brian Seger. Role of ion-selective membranes in the carbon balance for co2 electroreduction via gas diffusion electrode reactor designs. *Chem. Sci.*, 11:8854–8861, 2020.

[82] Hongzhou Yang, Jerry J. Kaczur, Syed D. Sajjad, and Richard I. Masel. Co2 conversion to formic acid in a three compartment cell with sustainion™ membranes. *ECS Transactions*, 77(11):1425, jul 2017.

[83] Helene Rehberger, Mohammad Rezaei, and Abdalaziz Aljabour. Challenges and opportunities of choosing a membrane for electrochemical CO_2 reduction. *Membranes*, 15(2), 2025.

[84] Björn Eriksson, Tristan Asset, Francesco Spanu, Frédéric Lecoeur, Marc Dupont, Felipe A. Garcés-Pineda, José Ramón Galán-Mascarós, Sara Cavaliere, Jacques Rozière, and Frédéric Jaouen. Mitigation of carbon crossover in CO_2 electrolysis by use of bipolar membranes. *Journal of The Electrochemical Society*, 169(3):034508, mar 2022.

[85] R. Pärnamäe, S. Mareev, V. Nikonenko, S. Melnikov, N. Sheldeshov, V. Zabolotskii, H.V.M. Hamelers, and M. Tedesco. Bipolar membranes: A review on principles, latest developments, and applications. *Journal of Membrane Science*, 617:118538, 2021.

[86] Ádám Vass, Attila Kormányos, Zsófia Kószó, Balázs Endrődi, and Csaba Janáky. Anode catalysts in CO_2 electrolysis: Challenges and untapped opportunities. *ACS Catalysis*, 12(2):1037–1051, 2022.

[87] Yunlong Ding, Wenwen Liu, Zirui Xu, and Zhiyao Duan. The origin of high electrochemical stability of iridium oxides for oxygen evolution. *J. Mater. Chem. A*, 12:20317–20326, 2024.

[88] Mahya Salmanion and Mohammad Mahdi Najafpour. Oxygen-evolution reaction performance of nickel (hydr)oxide in alkaline media: Iron and nickel impurities. *The Journal of Physical Chemistry C*, 127(37):18340–18349, 2023.

[89] Ádám Vass, Balázs Endrődi, Gergely Ferenc Samu, Ádám Balog, Attila Kormányos, Serhiy Cherevko, and Csaba Janáky. Local chemical environment governs anode processes in CO_2 electrolyzers. *ACS Energy Letters*, 6(11):3801–3808, 2021.

[90] M. Favaro, C. Valero-Vidal, J. Eichhorn, F. M. Toma, P. N. Ross, J. Yano, Z. Liu, and E. J. Crumlin. Elucidating the alkaline oxygen evolution reaction mechanism on platinum. *J. Mater. Chem. A*, 5:11634–11643, 2017.

[91] Jianbo Wu and Hong Yang. Platinum-based oxygen reduction electrocatalysts. *Accounts of Chemical Research*, 46(8):1848–1857, 2013. PMID: 23808919.

[92] Bo You and Yujie Sun. Innovative strategies for electrocatalytic water splitting. *Accounts of Chemical Research*, 51(7):1571–1580, 2018. PMID: 29537825.

[93] Wanyi Liao, Qin Zhao, Shanshan Wang, Yiling Ran, Hong Su, Rong Gan, Shun Lu, and Yan Zhang. Insights into mechanisms on electrochemical oxygen evolution substitution reactions. *Journal of Catalysis*, 428:115161, 2023.

[94] Lei Fan, Chuan Xia, Fangqi Yang, Jun Wang, Haotian Wang, and Yingying Lu. Strategies in catalysts and electrolyzer design for electrochemical CO_2 reduction toward C_{2+} products. *Science Advances*, 6(8):eaay3111, 2020.

[95] Ramato Ashu Tufa, Debabrata Chanda, Ming Ma, David Aili, Taye Beyene Demissie, Jan Vaes, Qingfeng Li, Shanhu Liu, and Deepak Pant. Towards highly efficient electrochemical CO_2 reduction: Cell designs, membranes and electrocatalysts. *Applied Energy*, 277:115557, 2020.

[96] Roger Lin, Jiaxun Guo, Xiaojia Li, Poojan Patel, and Ali Seifitokaldani. Electrochemical reactors for CO_2 conversion. *Catalysts*, 10(5), 2020.

[97] Matteo Agliuzza, Alessio Mezza, and Adriano. Solar-driven integrated carbon capture and utilization: Coupling CO_2 electroreduction toward CO with capture or photovoltaic systems. *Applied Energy*, 334:120649, 2023.

[98] Hesamoddin Rabiee, Lei Ge, Xueqin Zhang, Shihu Hu, Mengran Li, and Zhiguo Yuan. Gas diffusion electrodes (GDEs) for electrochemical reduction of carbon dioxide, carbon monoxide, and dinitrogen to value-added products: a review. *Energy Environ. Sci.*, 14:1959–2008, 2021.

[99] Mariana C O Monteiro, Matthew F Philips, Klaas Jan P Schouten, and Marc T M Koper. Efficiency and selectivity of CO_2 reduction to CO on gold gas diffusion electrodes in acidic media. *Nature Communications*, 12(1):4943, aug 2021.

[100] H. Yu and C. Hebling. Fuel cells: Microsystems. In K.H. Jürgen Buschow, Robert W. Cahn, Merton C. Flemings, Bernhard Ilschner, Edward J. Kramer, Subhash Mahajan, and Patrick Veyssière, editors, *Encyclopedia of Materials: Science and Technology*, pages 1–13. Elsevier, Oxford, 2005.

[101] Hesamoddin Rabiee, Beibei Ma, Yu Yang, Fengwang Li, Penghui Yan, Yuming Wu, Xueqin Zhang, Shihu Hu, Hao Wang, Lei Ge, and Zhonghua Zhu. Advances and challenges of carbon-free gas-diffusion electrodes (gdes) for electrochemical CO_2 reduction. *Advanced Functional Materials*, 35(1):2411195, 2025.

[102] Angelika Anita Samu, Imre Szenti, Ákos Kukovecz, Balázs Endrődi, and Csaba Janáky. Systematic screening of gas diffusion layers for high performance CO_2 electrolysis. *Communications Chemistry*, 6(1):41, feb 2023.

[103] Yuming Wu, Hesamoddin Rabiee, Xiu Song Zhao, Geoff Wang, and Yijiao Jiang. Insights into electrolyte flooding in flexible gas diffusion electrodes for CO_2 electrolysis: from mechanisms to effective mitigation strategies. *J. Mater. Chem. A*, 12:14206–14228, 2024.

[104] Lei Ge, Hesamoddin Rabiee, Mengran Li, Siddhartha Subramanian, Yao Zheng, Joong Hee Lee, Thomas Burdyny, and Hao Wang. Electrochemical CO_2 reduction in membrane-electrode assemblies. *Chem*, 8(3):663–692, 2022.

[105] Lucas Hoof, Niklas Thissen, Kevinjeorjios Pellumbi, Kai junge Puring, Daniel Siegmund, Anna K. Mechler, and Ulf-Peter Apfel. Hidden parameters for electrochemical carbon dioxide reduction in zero-gap electrolyzers. *Cell Reports Physical Science*, 3(4):100825, 2022.

[106] Bjørt Óladóttir Joensen, José A. Zamora Zeledón, Lena Trotochaud, Andrea Sartori, Marta Mirolo, Asger Barkholt Moss, Sahil Garg, Ib Chorkendorff, Jakub Drnec, Brian Seger, and Qiucheng Xu. Unveiling transport mechanisms of cesium and water in operando zero-gap CO_2 electrolyzers. *Joule*, 8(6):1754–1771, 2024.

[107] Bert De Mot, Mahinder Ramdin, Jonas Hereijgers, Thijs J. H. Vlugt, and Tom Breugelmans. Direct water injection in catholyte-free zero-gap carbon dioxide electrolyzers. *ChemElectroChem*, 7(18):3839–3843, 2020.

[108] Mark Sassenburg, Maria Kelly, Siddhartha Subramanian, Wilson A. Smith, and Thomas Burdyny. Zero-gap electrochemical CO_2 reduction cells: Challenges and operational strategies for prevention of salt precipitation. *ACS Energy Letters*, 8(1):321–331, 2023.

[109] Tiehuai Li and Minhua Shao. A minireview on electrochemical CO2 conversion based on carbonate/bicarbonate media, journal =EES Catal., year =2024, volume =2, issue =2, pages =564-572, publisher =RSC, doi =10.1039/D3EY00287J, url =http://dx.doi.org/10.1039/D3EY00287J,.

[110] Tengfei Li, Eric W. Lees, Maxwell Goldman, Danielle A. Salvatore, David M. Weekes, and Curtis P. Berlinguette. Electrolytic Conversion of Bicarbonate into CO in a Flow Cell. *Joule*, 3(6):1487–1497, 2019.

[111] James R. McKone, Nathan S. Lewis, and Harry B. Gray. Will solar-driven water-splitting devices see the light of day? *Chemistry of Materials*, 26(1):407–414, 2014.

[112] S. R. Wenham and M. A. Green. Silicon solar cells. *Progress in Photovoltaics: Research and Applications*, 4(1):3–33, 1996.

[113] Darren M. Bagnall and Matt Boreland. Photovoltaic technologies. *Energy Policy*, 36(12):4390–4396, 2008. Foresight Sustainable Energy Management and the Built Environment Project.

[114] Taesoo D. Lee and Abasifreke U. Ebong. A review of thin film solar cell technologies and challenges. *Renewable and Sustainable Energy Reviews*, 70:1286–1297, 2017.

[115] Jiawei Gong, K. Sumathy, Qiquan Qiao, and Zhengping Zhou. Review on dye-sensitized solar cells (DSSCs): Advanced techniques and research trends. *Renewable and Sustainable Energy Reviews*, 68:234–246, 2017.

[116] S. Shalini, R. Balasundaraprabhu, T. Satish Kumar, N. Prabavathy, S. Senthilarasu, and S. Prasanna. Status and outlook of sensitizers/dyes used in dye sensitized solar cells (DSSC): a review. *International Journal of Energy Research*, 40(10):1303–1320, 2016.

[117] Muhammad Shakeel Ahmad, A.K. Pandey, and Nasrudin Abd Rahim. Advancements in the development of TiO_2 photoanodes and its fabrication methods for dye sensitized solar cell (DSSC) applications. a review. *Renewable and Sustainable Energy Reviews*, 77:89–108, 2017.

[118] Wenjing Yu, Xiaoran Sun, Mu Xiao, Tian Hou, Xu Liu, Bolin Zheng, Hua Yu, Meng Zhang, Yuelong Huang, and Xiaojing Hao. Recent advances on interface engineering of perovskite solar cells. *Nano Research*, 15(1):85–103, jan 2022.

[119] Nam-Gyu Park. Perovskite solar cells: an emerging photovoltaic technology. *Materials Today*, 18(2):65–72, 2015.

[120] Martin A Green, Anita Ho-Baillie, and Henry J Snaith. The emergence of perovskite solar cells. *Nature Photonics*, 8(7):506–514, jul 2014.

[121] National Renewable Energy Laboratory. Best Research-Cell Efficiency Chart — nrel.gov. https://www.nrel.gov/pv/cell-efficiency.html. [Accessed 27-02-2025].

[122] Mark T. Winkler, Casandra R. Cox, Daniel G. Nocera, and Tonio Buonassisi. Modeling integrated photovoltaic–electrochemical devices using steady-state equivalent circuits. *Proceedings of the National Academy of Sciences*, 110(12):E1076–E1082, 2013.

[123] Gurudayal, James Bullock, Dávid F. Srankó, Clarissa M. Towle, Yanwei Lum, Mark Hettick, M. C. Scott, Ali Javey, and Joel Ager. Efficient solar-driven electrochemical CO_2 reduction to hydrocarbons and oxygenates. *Energy Environ. Sci.*, 10:2222–2230, 2017.

[124] M Klein, R Pankiewicz, M Zalas, and W Stampor. Magnetic field effects in dye-sensitized solar cells controlled by different cell architecture. *Scientific Reports*, 6(1):30077, jul 2016.

[125] Marcel Schreier, Laura Curvat, Fabrizio Giordano, Ludmilla Steier, Antonio Abate, Shaik M Zakeeruddin, Jingshan Luo, Matthew T Mayer, and Michael Grätzel. Efficient photosynthesis of carbon monoxide from CO_2 using perovskite photovoltaics. *Nature Communications*, 6(1):7326, jun 2015.

[126] Takeo Arai, Shunsuke Sato, Keita Sekizawa, Tomiko M. Suzuki, and Takeshi Morikawa. Solar-driven CO_2 to CO reduction utilizing H_2O as an electron donor by earth-abundant Mn–bipyridine complex and Ni-modified Fe-oxyhydroxide catalysts activated in a single-compartment reactor. *Chem. Commun.*, 55:237–240, 2019.

[127] Teppei Nishi, Shunsuke Sato, Keita Sekizawa, Tomiko M. Suzuki, Keiichiro Oh-ishi, Naoko Takahashi, Yoriko Matsuoka, and Takeshi Morikawa. Carbon Nanohorn Support for Solar driven CO_2 reduction to CO catalyzed by Mn-complex in an All Earth-abundant System. *ChemNanoMat*, 7(6):596–599, 2021.

[128] Adriano Sacco, Roberto Speranza, Umberto Savino, Juqin Zeng, M. Amin Farkhondehfal, Andrea Lamberti, Angelica Chiodoni, and Candido F. Pirri. An Integrated Device for the Solar-Driven Electrochemical Conversion of CO_2 to CO. *ACS Sustainable Chemistry & Engineering*, 8(20):7563–7568, 2020.

[129] Marcel Schreier, Florent Héroguel, Ludmilla Steier, Shahzada Ahmad, Jeremy S Luterbacher, Matthew T Mayer, Jingshan Luo, and Michael Grätzel. Solar conversion of CO_2 to CO using Earth-abundant electrocatalysts prepared by atomic layer modification of CuO. *Nature Energy*, 2(7):17087, jun 2017.

[130] Jaehoon Chung, Nam Joong Jeon, and Jun Hong Noh. Solar-Driven Simultaneous Electrochemical CO_2 Reduction and Water Oxidation Using Perovskite Solar Cells. *Energies*, 15(1), 2022.

[131] Hyojung Bae, Chaewon Seong, Vishal Burungale, Myeongheon Seol, Chul Oh Yoon, Soon Hyung Kang, Wan-Gil Jung, Bong-Joong Kim, and Jun-Seok Ha. Nanostructured Au Electrode with 100 h Stability for Solar-Driven Electrochemical Reduction of Carbon Dioxide to Carbon Monoxide. *ACS Omega*, 7(11):9422–9429, 2022.

[132] Wenjun Zhang, Yuren Xia, Shuangming Chen, Yi Hu, Songyuan Yang, Zuoxiu Tie, and Zhong Jin. Single-Atom Metal Anchored Zr_6-Cluster-Porphyrin

Framework Hollow Nanocapsules with Ultrahigh Active-Center Density for Electrocatalytic CO_2 Reduction. *Nano Letters*, 22(8):3340–3348, 2022. PMID: 35412833.

[133] Yuhang Wang, Junlang Liu, Yifei Wang, Yonggang Wang, and Gengfeng Zheng. Efficient solar-driven electrocatalytic CO_2 reduction in a redox-medium-assisted system. *Nature Communications*, 9(1):5003, nov 2018.

[134] Weiguang Ma, Hong Wang, Wei Yu, Xiaomei Wang, Zhiqiang Xu, Xu Zong, and Can Li. Achieving Simultaneous CO_2 and H_2S Conversion via a Coupled Solar-Driven Electrochemical Approach on Non-Precious-Metal Catalysts. *Angewandte Chemie International Edition*, 57(13):3473–3477, 2018.

[135] Beomil Kim, Hoeun Seong, Jun Tae Song, Kyuju Kwak, Hakhyeon Song, Ying Chuan Tan, Gibeom Park, Dongil Lee, and Jihun Oh. Over a 15.9% Solar-to-CO Conversion from Dilute CO_2 Streams Catalyzed by Gold Nanoclusters Exhibiting a High CO_2 Binding Affinity. *ACS Energy Letters*, 5(3):749–757, 2020.

[136] Wen-Hui Cheng, Matthias H. Richter, Ian Sullivan, David M. Larson, Chengxiang Xiang, Bruce S. Brunschwig, and Harry A. Atwater. CO_2 Reduction to CO with 19% Efficiency in a Solar-Driven Gas Diffusion Electrode Flow Cell under Outdoor Solar Illumination. *ACS Energy Letters*, 5(2):470–476, 2020.

[137] Cai Wang, Houan Ren, Zihao Wang, Qingxin Guan, Yuping Liu, and Wei Li. A promising single-atom Co-N-C catalyst for efficient CO_2 electroreduction and high-current solar conversion of CO_2 to CO. *Applied Catalysis B: Environmental*, 304:120958, 2022.

[138] Woong Hee Lee, Chulwan Lim, Eunseo Ban, Soohyun Bae, Jongwon Ko, Hae-Seok Lee, Byoung Koun Min, Kwan-Young Lee, Jae Su Yu, and Hyung-Suk Oh. W@Ag dendrites as efficient and durable electrocatalyst for solar-to-CO conversion using scalable photovoltaic-electrochemical system. *Applied Catalysis B: Environmental*, 297:120427, 2021.

[139] N Gupta, M Gattrell, and B MacDougall. Calculation for the cathode surface concentrations in the electrochemical reduction of CO_2 in $KHCO_3$ solutions. *Journal of Applied Electrochemistry*, 36(2):161–172, feb 2006.

[140] Adriano Sacco, Juqin Zeng, Katarzyna Bejtka, and Angelica Chiodoni. Modeling of gas bubble-induced mass transport in the electrochemical reduction of carbon dioxide on nanostructured electrodes. *Journal of Catalysis*, 372:39–48, 2019.

[141] Kunna Wu, Erik Birgersson, Byoungsu Kim, Paul J. A. Kenis, and Iftekhar A. Karimi. Modeling and Experimental Validation of Electrochemical Reduction of CO_2 to CO in a Microfluidic Cell. *Journal of The Electrochemical Society*, 162(1):F23, nov 2014.

[142] Yosra Kotb, Seif-Eddeen K. Fateen, Jonathan Albo, and Ibrahim Ismail. Modeling of a Microfluidic Electrochemical Cell for the Electro-Reduction of CO_2 to CH_3OH. *Journal of The Electrochemical Society*, 164(13):E391, oct 2017.

[143] Meenesh R. Singh, Ezra L. Clark, and Alexis T. Bell. Effects of electrolyte, catalyst, and membrane composition and operating conditions on the performance of solar-driven electrochemical reduction of carbon dioxide. *Phys. Chem. Chem. Phys.*, 17:18924–18936, 2015.

[144] Xiaojiao Luo, Jin Xuan, Eva Sanchez Fernandez, and M. Mercedes Maroto-Valer. Modeling and simulation for photoelectrochemical CO_2 utilization. *Energy Procedia*, 158:809–815, 2019. Innovative Solutions for Energy Transitions.

[145] Selvaraj Chinnathambi, Mahinder Ramdin, and Thijs J. H. Vlugt. Mass Transport Limitations in Electrochemical Conversion of CO_2 to Formic Acid at High Pressure. *Electrochem*, 3(3):549–569, 2022.

[146] Wei Yang, Licheng Sun, Jingjing Bao, Zhengyu Mo, Min Du, Jun Li, and Jun Zhang. Two-Phase Flow Model to Define the Mass Transport in a Bicarbonate Electrolyzer for a CO_2 Reduction Reaction. *Industrial & Engineering Chemistry Research*, 62(40):16469–16480, 2023.

[147] Cornelius A Obasanjo, Guorui Gao, Jackson Crane, Viktoria Golovanova, F Pelayo García de Arquer, and Cao-Thang Dinh. High-rate and selective conversion of CO_2 from aqueous solutions to hydrocarbons. *Nature Communications*, 14(1):3176, jun 2023.

[148] Matteo Agliuzza, Roberto Speranza, Andrea Lamberti, Candido Fabrizio Pirri, and Adriano Sacco. Experimental and Modeling Study for the Solar-Driven CO_2 Electrochemical Reduction to CO. *Applied Sciences*, 15(2), 2025.

[149] Diego Mariano. Ottimizzazione dei componenti di un sistema elettrochimico integrato per la valorizzazione della co2 alimentato ad energia solare = component optimization of an integrated electrochemical system for solar-powered co2 valorization. Novembre 2023.

[150] Matteo Agliuzza, Candido Fabrizio Pirri, and Adriano Sacco. A comprehensive modeling for the CO_2 electroreduction to CO. *J. Phys. Energy*, 6(1):015004, jan 2024.

[151] Allen J Bard, Larry R Faulkner, and Henry S White. *Electrochemical methods: fundamentals and applications*. John Wiley & Sons, 2022.

[152] F. Richard Keene. Chapter 1 - THERMODYNAMIC, KINETIC, AND PRODUCT CONSIDERATIONS IN CARBON DIOXIDE REACTIVITY. In B.P. Sullivan, editor, *Electrochemical and Electrocatalytic Reactions of Carbon Dioxide*, pages 1–18. Elsevier, Amsterdam, 1993.

[153] John Newman and Nitash P Balsara. *Electrochemical systems*. John Wiley & Sons, 2021.

[154] Noam Agmon. The grotthuss mechanism. *Chemical Physics Letters*, 244(5):456–462, 1995.

[155] Yann A. Le Gouellec and Menachem Elimelech. Control of calcium sulfate (gypsum) scale in nanofiltration of saline agricultural drainage water. *Environmental Engineering Science*, 19(6):387–397, 2002.

[156] Edward Lansing Cussler. *Diffusion: mass transfer in fluid systems*. Cambridge university press, 2009.

[157] Hiroyuki Ohshima and Tamotsu Kondo. Relationship among the surface potential, Donnan potential and charge density of ion-penetrable membranes. *Biophysical Chemistry*, 38(1):117–122, 1990.

[158] Hiroyuki Ohshima and Tamotsu Kondo. Membrane potential and Donnan potential. *Biophysical Chemistry*, 29(3):277–281, 1988.

[159] Edmund J.F. Dickinson and Andrew J. Wain. The Butler-Volmer equation in electrochemical theory: Origins, value, and practical application. *Journal of Electroanalytical Chemistry*, 872:114145, 2020. Dr. Richard Compton 65th birthday Special issue.

[160] Wolfgang Dreyer, Clemens Guhlke, and Rüdiger Müller. A new perspective on the electron transfer: recovering the Butler–Volmer equation in non-equilibrium thermodynamics. *Phys. Chem. Chem. Phys.*, 18:24966–24983, 2016.

[161] R.F. Mann, J.C. Amphlett, B.A. Peppley, and C.P. Thurgood. Application of Butler–Volmer equations in the modelling of activation polarization for PEM fuel cells. *Journal of Power Sources*, 161(2):775–781, 2006.

[162] B. Goss, I.R. Cole, E. Koubli, D. Palmer, T.R. Betts, and R. Gottschalg. 4 - modelling and prediction of pv module energy yield. In Nicola Pearsall, editor, *The Performance of Photovoltaic (PV) Systems*, pages 103–132. Woodhead Publishing, 2017.

[163] Edmund J.F. Dickinson, Henrik Ekström, and Ed Fontes. COMSOL Multiphysics®: Finite element software for electrochemical analysis. A mini-review. *Electrochemistry Communications*, 40:71–74, 2014.

[164] Peter Horsman, Brian E Conway, and E Yeager. *Comprehensive Treatise of Electrochemistry: Electrodics: Transport*. Springer Science & Business Media, 2013.

[165] Alaa A. Zaky, Peter Sergeant, Elias Stathatos, Polycarpos Falaras, and Mohamed N. Ibrahim. Employing Dye-Sensitized Solar Arrays and Synchronous Reluctance Motors to Improve the Total Cost and Energy Efficiency of Solar Water-Pumping Systems. *Machines*, 10(10), 2022.

[166] Xiao-Zhi Guo, Yan-Hong Luo, Chun-Hui Li, Da Qin, Dong-Mei Li, and Qing-Bo Meng. Can the incident photo-to-electron conversion efficiency be used to calculate short-circuit current density of dye-sensitized solar cells. *Current Applied Physics*, 12:e54–e58, 2012. International Workshop on Flexible & Printable Electronics.

[167] M. Chegaar, A. Hamzaoui, A. Namoda, P. Petit, M. Aillerie, and A. Herguth. Effect of Illumination Intensity on Solar Cells Parameters. *Energy Procedia*, 36:722–729, 2013. TerraGreen 13 International Conference 2013 - Advancements in Renewable Energy and Clean Environment.

[168] A. Kassis and M. Saad. Analysis of multi-crystalline silicon solar cells at low illumination levels using a modified two-diode model. *Solar Energy Materials and Solar Cells*, 94(12):2108–2112, 2010.

[169] Toru Hatsukade, Kendra P. Kuhl, Etosha R. Cave, David N. Abram, and Thomas F. Jaramillo. Insights into the electrocatalytic reduction of CO_2 on metallic silver surfaces. *Phys. Chem. Chem. Phys.*, 16:13814–13819, 2014.

[170] Xianlong Zhou, Hao Liu, Bao Yu Xia, Kostya (Ken) Ostrikov, Yao Zheng, and Shi-Zhang Qiao. Customizing the microenvironment of CO_2 electrocatalysis via three-phase interface engineering. *SmartMat*, 3(1):111–129, 2022.

[171] T. E. Springer, T. A. Zawodzinski, and S. Gottesfeld. Polymer Electrolyte Fuel Cell Model. *Journal of The Electrochemical Society*, 138(8):2334, aug 1991.

[172] S. Rakhshanpouri and S. Rowshanzamir. Water transport through a PEM (proton exchange membrane) fuel cell in a seven-layer model. *Energy*, 50:220–231, 2013.

[173] Jia-Kang Tang, Chen-Yuan Zhu, Tian-Wen Jiang, Lei Wei, Hui Wang, Ke Yu, Chun-Lei Yang, Yue-Biao Zhang, Chen Chen, Zhan-Ting Li, Dan-Wei Zhang, and Li-Ming Zhang. Anion exchange-induced single-molecule dispersion of cobalt porphyrins in a cationic porous organic polymer for enhanced electrochemical CO_2 reduction via secondary-coordination sphere interactions. *J. Mater. Chem. A*, 8:18677–18686, 2020.

[174] Yuanxing Wang, Cailing Niu, Yachuan Zhu, Da He, and Weixin Huang. Tunable Syngas Formation from Electrochemical CO_2 Reduction on Copper Nanowire Arrays. *ACS Applied Energy Materials*, 3(10):9841–9847, 2020.

[175] Ming He, Chunsong Li, Haochen Zhang, Xiaoxia Chang, Jingguang G Chen, William A Goddard, Mu-Jeng Cheng, Bingjun Xu, and Qi Lu. Oxygen induced promotion of electrochemical reduction of CO_2 via co-electrolysis. *Nature Communications*, 11(1):3844, jul 2020.

[176] Yikai Chen and Nathan S. Lewis. Numerical Simulation and Modeling of Hydrogen Gas Evolution on Planar and Microwire Array Electrodes. *Journal of The Electrochemical Society*, 169(6):066510, jun 2022.

[177] Byron Ross, Sophia Haussener, and Katharina Brinkert. Impact of Gas Bubble Evolution Dynamics on Electrochemical Reaction Overpotentials in Water Electrolyser Systems. *The Journal of Physical Chemistry C*, 129(9):4383–4397, 2025.

[178] Juan Manuel Paz-García, Björn Johannesson, Lisbeth M. Ottosen, Alexandra B. Ribeiro, and José Miguel Rodríguez-Maroto. Modeling of electrokinetic processes by finite element integration of the Nernst–Planck–Poisson system of equations. *Separation and Purification Technology*, 79(2):183–192, 2011. Scientific Advances and Innovative Applications in Electrokinetic Remediation.

[179] Haijiao Lu and Lianzhou Wang. Unbiased photoelectrochemical carbon dioxide reduction shaping the future of solar fuels. *Applied Catalysis B: Environment and Energy*, 345:123707, 2024.

[180] Jozef H. Meessen. *Urea*. John Wiley & Sons, Ltd, 2010.

[181] V Mane, A Ranveer, and Mahesh Suryawanshi. Improvement reactor efficiency of urea. *Int J Technol Manag*, 5:291–8, 2016.

[182] Max Appl. *Ammonia*. John Wiley & Sons, Ltd, 2000.

[183] Xin Liu, Yan Jiao, Yao Zheng, Mietek Jaroniec, and Shi-Zhang Qiao. Mechanism of C-N bonds formation in electrocatalytic urea production revealed by ab initio molecular dynamics simulation. *Nature Communications*, 13(1):5471, sep 2022.

[184] Laura C. Green, David A. Wagner, Joseph Glogowski, Paul L. Skipper, John S. Wishnok, and Steven R. Tannenbaum. Analysis of nitrate, nitrite, and [15N]nitrate in biological fluids. *Analytical Biochemistry*, 126(1):131–138, 1982.

[185] Gao-Feng Chen, Yifei Yuan, Haifeng Jiang, Shi-Yu Ren, Liang-Xin Ding, Lu Ma, Tianpin Wu, Jun Lu, and Haihui Wang. Electrochemical reduction of nitrate to ammonia via direct eight-electron transfer using a copper–molecular solid catalyst. *Nature Energy*, 5(8):605–613, aug 2020.

[186] H. Verdouw, C.J.A. Van Echteld, and E.M.J. Dekkers. Ammonia determination based on indophenol formation with sodium salicylate. *Water Research*, 12(6):399–402, 1978.

[187] Mohammed Rahmatullah and T.R.C. Boyde. Improvements in the determination of urea using diacetyl monoxime; methods with and without deproteinisation. *Clinica Chimica Acta*, 107(1):3–9, 1980.

[188] Sibo Chen, Shuting Lin, Liang-Xin Ding, and Haihui Wang. Modified diacetylmonoxime-thiosemicarbazide detection protocol for accurate quantification of urea. *Small Methods*, 7(9):2300003, 2023.

[189] Tiange Yuan and Oleksandr Voznyy. Guidelines for reliable urea detection in electrocatalysis. *Cell Reports Physical Science*, 4(8):101521, 2023.

[190] Yan Zhang, Gefei Huang, Haichuan Zhang, Xiaoyi Qiu, Guimei Liu, Yinuo Wang, Juhee Jang, Yian Wang, Zidong Wei, Zongwei Cai, and Minhua Shao. Reliable and accessible methods for urea quantification in co-reduction of carbon-dioxide- and nitrogen-containing species. *Chem Catalysis*, 5(3):101234, 2025.

[191] Michele Ferri. Ureality check: Approaching the rising field of electrofertilizers. *ACS Energy Letters*, 9(5):2394–2400, 2024.

[192] Blaž Tomc, Marjan Bele, Mohammed Azeezulla Nazrulla, Primož Šket, Matjaž Finšgar, Angelja Kjara Surca, Ana Rebeka Kamšek, Martin Šala, Jan Šiler Hudoklin, Matej Huš, Blaž Likozar, and Nejc Hodnik. Deactivation of copper electrocatalysts during CO_2 reduction occurs via dissolution and selective redeposition mechanism. *J. Mater. Chem. A*, 13:4119–4128, 2025.

Appendix A

Electrochemical Urea Production from Nitrate and CO_2

In this supplemental study, it has been explored in preliminar studies the electrochemical co-reduction of nitrogen oxides (NO_x) and CO_2 toward urea formation, alongside the development and validation of a colorimetric assay for reliable urea quantification. Urea ($CO(NH_2)_2$) is an attractive target molecule in electrochemical nitrogen valorization due to its high hydrogen and nitrogen content, established industrial applications, and role as a fertilizer precursor [180]. Traditional industrial urea synthesis relies on high-pressure, high-temperature fossil fuel-based routes that couple ammonia and carbon dioxide, which is to say the Bosch-Meiser process [181, 182]. In contrast, the direct electrochemical coupling of nitrate (NO_3^-) and CO_2 at ambient conditions promises a more sustainable and decentralized pathway. Moreover, this process aims also to close the nitrate loop, a common pollutant discharged in wastewaters or emitted in industrial effluents alongside CO_2.
However, accurately monitoring low-concentration urea in complex electrolytes poses significant analytical challenges. By integrating a robust, low-cost colorimetric detection platform with electrochemical coreduction experiments, this appendix establishes a practical framework for urea quantification in future reactor designs. It also underscores the importance of analytical method development in advancing novel electrochemical routes to value-added, nitrogen-rich chemicals.

Theory

In the electrocatalytic synthesis of urea from CO_2 and NO_3^-, the central challenge is the formation of C–N bonds under applied potential in an aqueous environment. Ab initio molecular dynamics simulations that explicitly account for water dynamics and electrode potential reveal that C–N coupling proceeds via two consecutive steps involving the surface-bound intermediates $*CO$ and $*NH$, rather than by direct coupling of more oxidized nitrogen species [183]. The overall reaction network can be described as:

$$*NH \xrightarrow{\text{C–N coupling}} *NH{-}CO \xrightarrow{\text{C–N coupling}} *NH{-}CO{-}NH \xrightarrow{\text{protonation}} CO(NH_2)_2\,.$$

First, under mildly negative potentials (approximately –0.75 V vs SHE), nitrate/nitrite is rapidly reduced to ammonia via pathways such as $*NO \rightarrow *NOH \rightarrow *N \rightarrow *NH$ or $*HNO \rightarrow *NHOH \rightarrow *NH$. The low barrier for $*N$ protonation ($\approx$0.21 eV) suppresses competing N–N coupling and leads to accumulation of $*NH$ on the surface. Concurrently, CO_2 reduction yields $*CO$ due to slow protonation of CO. The coupling of $*CO$ with $*NH$ to form $*NH{-}CO$ has an activation barrier of $\approx$0.66 eV, which is lower than competing protonation steps. More oxidized nitrogen species (e.g. $*NO, *HNO, *N, *NH_2$) either protonate more readily or face prohibitively high coupling barriers, rendering them inactive for C–N bond formation.

After the first C–N bond is established, coupling of $*NH{-}CO$ with a second $*NH$ occurs with a barrier of $\approx$0.51 eV, again lower than competing protonation ($\approx$0.85 eV). The resulting $*NH{-}CO{-}NH$ intermediate then undergoes facile protonation ($\approx$0.50–0.52 eV) to yield surface-bound urea, which subsequently desorbs as $CO(NH_2)_2$.

At more cathodic potentials (around –1.5 V vs SHE), enhanced protonation kinetics and altered interfacial water orientation accelerate both NO_3^- reduction to NH_3 and CO_2 reduction to CO/HCOOH, diminishing $*NH$ coverage and overall urea selectivity. Under these conditions, direct surface coupling of $*NH$ and $*CO$ becomes kinetically blocked (barrier $\approx$1.25 eV), but solution-phase CO can still couple with surface $*NH$ (barrier $\approx$0.62 eV), allowing for residual urea formation via a distinct mechanistic pathway.

By elucidating these potential-dependent C–N coupling steps (anchored on the critical roles of $*NH$ and $*CO$ intermediates) this framework provides a molecular-level

understanding for the design of catalysts and operating conditions that maximize urea selectivity from CO_2 and nitrate feedstocks.

Methods

The main liquid products coming from the NO_3^- and CO_2 electrochemical co-reduction are nitrite (NO_2^-), ammonia (NH_3) and urea. For these chemical species, it is important to validate a reliable and efficient method of detection which brings fast and sensitive analysis. For these reasons, standard colorimetric test have been used already present in literature.

A.0.1 Griess Reagent Method

The Griess reagent method is a simple colorimetric assay used to detect and quantify nitrite in aqueous solutions [184, 185], by converting nitrite under acidic conditions first into a diazonium salt (through reaction with sulfanilamide) and then coupling that intermediate with N-(1-naphthyl)ethylenediamine to form a deeply colored azo dye whose intensity, measured spectrophotometrically (usually at about 540 nm), is related to the nitrite concentration. In the context of electrochemical urea production (where nitrite can arise as an undesired by-product or intermediate during the reduction of nitrogen species) this method allows to monitor how much nitrite accumulates in the electrolyte, and calculate its FE.
The Griess reagent is prepared by dissolving 1.0 g of sulfanilamide, 0.1 g of N-(1-naphthyl)ethyldiamine dihydrochloride (NED) and 2.94 ml of phosphoric acid (H_3PO_4) in 50 ml deionized water. Then, 1 ml of Griess reagent is mixed with 1 ml of the nitrite-containing electrolyte solution and 2 ml of water, and let react at room temperature for 10 minutes. The absorbance at 540 nm is measured with UV-visible spectroscopy to assess the NO_2^- concentration (Fig. A.1).

A.0.2 Salicylate Method

The salicylate (or “phenate”) method for ammonia determination is a modern colorimetric assay that builds on the classic indophenol-blue reaction but replaces phenol with sodium salicylate [186]. Under alkaline conditions, ammonia reacts

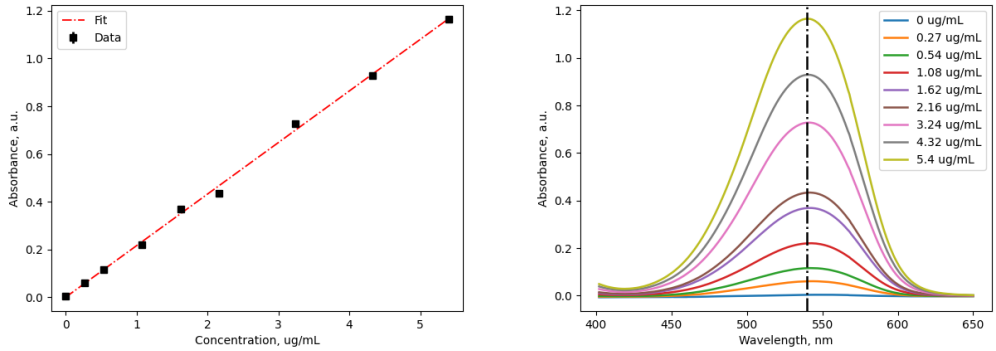

(a) (b)

Fig. A.1 Calibration curve (a) and absorbance spectra (b) of samples with increasing concentration of nitrite, with Griess reagent technique. The nitrite is diluted in a CO_2-saturated 0.1 M $KHCO_3$ + 0.1 M KNO_3 solution, to mimic the electrolysis environment.

with hypochlorite to form monochloramine, which then couples with salicylate in the presence of a nitroprusside catalyst to yield a green-blue indophenol dye. This salicylate-based assay is widely used instead of the older "indophenol blue" methods because it improves stability and avoids highly toxic compounds.
For this method, three solutions are prepared: 1 M NaOH solution with 5% wt. of salicylic acid and 5% wt. of sodium citrate (solution A), a 0.05 M solution of NaClO (solution B), and a 5% wt. of sodium nitroferricyanide (solution C). A mixture of 2 ml of solution A, 1 ml of solution B, 0.2 ml of solution C and 2 ml of ammonia-containing electrolyte solution is prepared, and stored for 2 hours at room temperature in dark conditions. The absorbance at 655 nm is then measured to assess the NH_3 concentration (Fig. A.2)

A.0.3 Diacetyl-Monoxime Method

The diacetyl monoxime (DAMO) method is the standard colorimetric assay specifically designed for the quantitative determination of urea, and the most frequently used in literature [187]. In this reaction, urea in an acidic medium reacts with diacetyl monoxime (2,3-butanedione monoxime) to form a yellowish "diazine" complex; this process is typically accelerated by heating and occurs in the presence of a strong acid (often sulfuric acid) and an oxidant (such as ferric chloride) to ensure complete conversion. To enhance color stability and sensitivity, thiosemicarbazide (TSC) is

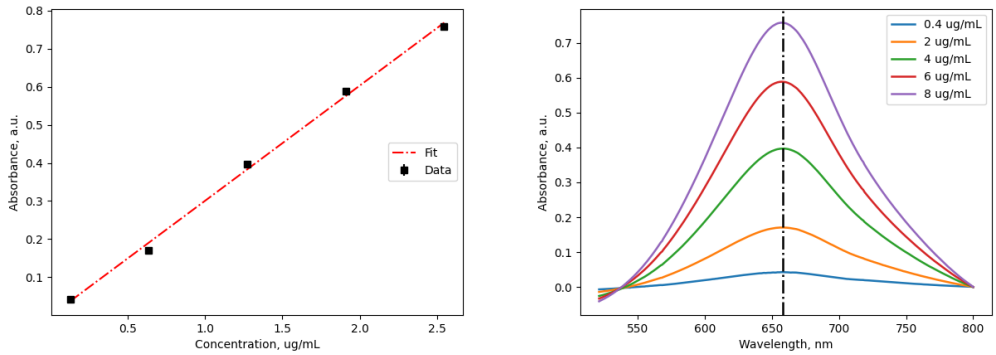

(a) (b)

Fig. A.2 Calibration curve (a) and absorbance spectra (b) of samples with increasing concentration of ammonia, with the salicylate method. The ammonia is diluted in a CO_2-saturated 0.1 M $KHCO_3$ + 0.1 M KNO_3 solution, to mimic the electrolysis environment.

frequently added as a coupling reagent, producing a stable pink-colored chromogen whose absorbance is measured spectrophotometrically. The intensity of the color is directly proportional to the urea concentration, allowing for detection down to low micromolar levels.

An acidic solution is prepared (solution A), by mixing 100 ml of H_3PO_4, 300 ml of sulfuric acid (H_3SO_4) and 100 mg of ferric chloride ($FeCl_3$) in 600 ml of deionized water. A chromogenic solution (solution B) is also prepared, in which 500 mg of DAMO and 10 mg of TSC are added in 100 ml of H_2O. After that, a mixture consisting of 2 ml of solution A, 1 ml of solution B and 1 ml of urea-containing electrolyte solution is prepared and let react in a water bath at 100°C for 20 minutes. The absorbance and calibration curve are reported in Fig. A.3.

A.0.4 Modified Diacetyl-Monoxime Method

The modified diacetyl monoxime–thiosemicarbazide (M-DAMO-TSC) method introduces a preliminary nitrite-consumption step to the classic DAMO-TSC assay in order to eliminate nitrite interference before urea quantification. In practice, a small volume of sulfamic acid (4 wt%) and dilute HCl (1 M) is added to the sample, converting any nitrite into harmless nitrogen gas; the solution is then treated exactly as in the traditional DAMO-TSC protocol, where diacetyl monoxime hydrolyzes under strong acid to react with urea, and the resulting diazine intermediate couples with

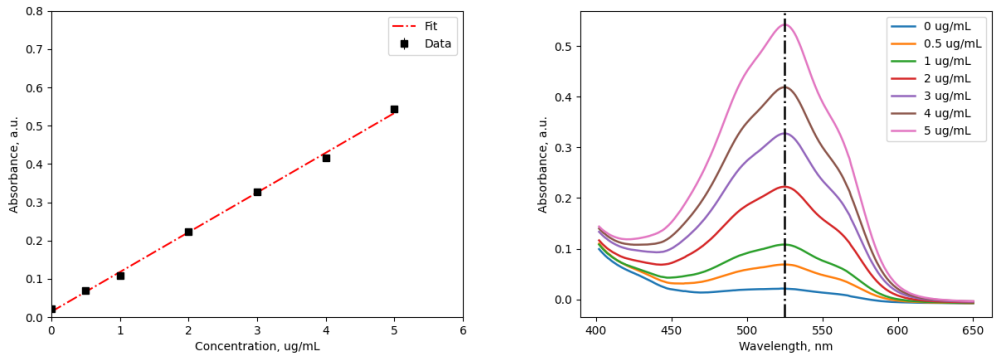

(a) (b)

Fig. A.3 Calibration curve (a) and absorbance spectra (b) of samples with increasing concentration of urea, with DAMO method. The urea is diluted in a CO_2-saturated 0.1 M $KHCO_3$ + 0.1 M KNO_3 solution, to mimic the electrolysis environment.

thiosemicarbazide to form a stable chromogen measured at 525 nm. By consuming nitrite up front, the M-DAMO-TSC method keeps quantification errors within ±3% for nitrite concentrations up to 30 ppm while preserving a low limit of quantification and high accuracy for urea down to sub-ppm levels [188].
In this case, 1 ml of urea-containing electrolyte solution is mixed with 100 μl of sulfamic acid and 300 μl of HCl, and let react at room temperature for 16 minutes (solution D). Then the standard DAMO procedure is carried out, using this solution D instead of the pure electrolyte (as explained in the previous section A.0.3): the calibration curves are reported in Fig. A.4.

A.0.5 Urease Decomposition Method

The urease decomposition method for urea quantification is an enzymatic assay in which the enzyme urease catalyzes the hydrolysis of urea into ammonia and carbon dioxide. In practice, a known volume of sample is incubated with an excess of urease (typically at controlled pH and temperature), allowing essentially complete conversion of urea to NH_3. The liberated ammonia is then measured, and the delta of NH_3 detected after and before the urease decomposition process is directly proportional to the original urea concentration. Despite being a slower and more laborious process with respect to DAMO method, the enzymatic process is highly selective toward urea and avoids false-positive results with great accuracy.

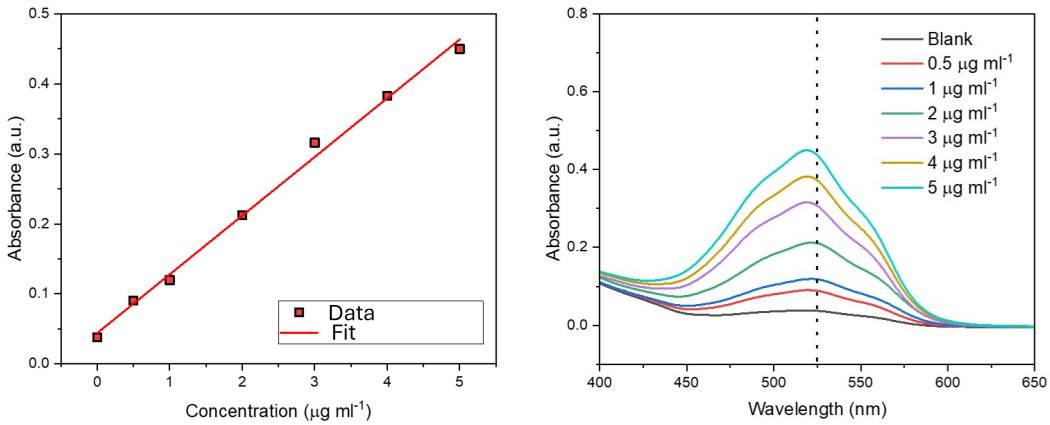

(a) (b)

Fig. A.4 Calibration curve (a) and absorbance spectra (b) of samples with increasing concentration of urea, with modified DAMO technique. The urea is diluted in a CO_2-saturated 0.1 M $KHCO_3$ + 0.1 M KNO_3 solution, to mimic the electrolysis environment.

In the urease-driven decomposition protocol, 0.5 mL of urease solution (5 mg mL^{-1}) was combined with 4.5 ml of the electrolyte and incubated at 40 °C for 40 minutes. The urease preparation itself was formulated by adding 0.1 g of ethylenediaminetetraacetic (EDTA) disodium salt and 0.49 g of K_2HPO_4 in every 100 mL of solution. After that, urea can be calculated by the amount of ammonia pre and post decomposition:

$$(NH_2)_2CO + H_2O \rightarrow 2NH_3 + CO_2 \tag{A.1}$$

$$m_{urea} = \frac{m_{urease} - m_{ammonia}}{2} \tag{A.2}$$

where m_{urea} is the final concentration of the urea inside the electrolyte, and m_{urease} ($m_{ammonia}$) is the concentration of ammonia after (before) the decomposition. In Fig. A.5 it is depicted the calibration curve for the urease decomposition method.

Results

For what concerns the electrochemical tests, the conditions are the same as previously reported in Section 3.1.The only difference lies in the electrolyte used, which now is an aqueous solution of 0.1M $KHCO_3$ + 0.1M KNO_3. The calculation for the FEs of

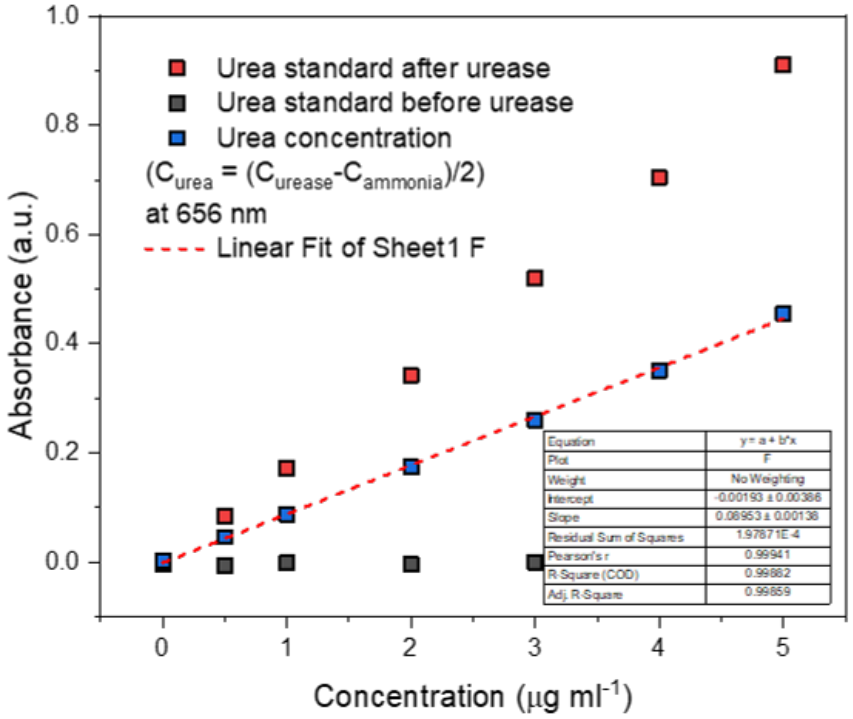

Fig. A.5 Calibration curve of samples with increasing concentration of urea, with urease decomposition technique. The urea is diluted in a CO_2-saturated 0.1 M $KHCO_3$ + 0.1 M KNO_3 solution, to mimic the electrolysis environment.

the liquid products are calculated with the following formula:

$$FE_{urea} = \frac{(16 \times V_{sol} \times F \times m_{urea})}{60.06(g/mol) \times Q} \tag{A.3}$$

$$FE_{NO_2^-} = \frac{(2 \times V_{sol} \times F \times m_{NO_2^-})}{46(g/mol) \times Q} \tag{A.4}$$

$$FE_{NH_3} = \frac{(8 \times V_{sol} \times F \times m_{NH_3})}{17(g/mol) \times Q} \tag{A.5}$$

where V_{sol} is the total volume of the electrolyte, Q the charge (calculated as the current times the time of the experiment, which is to say 1 hour), and m the concentrations calculated by means of UV-vis spectra.

A.0.6 DAMO vs. modified DAMO methods

In the field of urea production from nitrate and carbon dioxide co-reduction, DAMO method is the most widely used technique to detect urea in the electrolyte samples. On the other hand, the data are difficult to replicate and recent studies have shown limitations of such colorimetric techniques [189].
A first initial screening of DAMO (Section A.0.3) and modified DAMO (Section A.0.4) methods are reported in this present study. Please note that Griess reagent (Section A.0.1) and Salicylate (Section A.0.2) methods are used for the detection of nitrite and ammonia, respectively. The electrochemical tests are performed in three electrode configuration, with an Ag/AgCl reference electrode, with a commercial Pt foil as anode and commercial electropolished Cu foil as cathode. After 1 hour of electrolysis (at V= -0.8 V and V= -0.9 V vs. Ag/AgCl), in presence of a CO_2-saturated 0.1M $KHCO_3$ + 0.1M KNO_3 electrolyte, the electrolyte is studied under UV-vis irradiation following DAMO and modified DAMO methodologies (Fig. A.6).

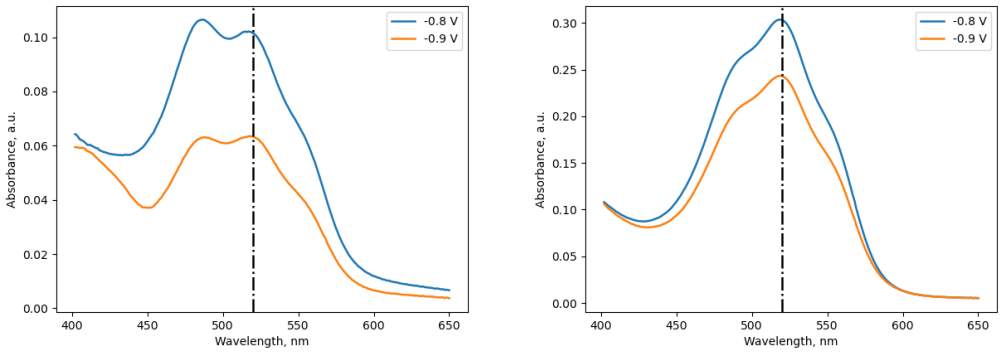

(a) (b)

Fig. A.6 Absorbance spectra of the electrolyte with DAMO (a) and modified DAMO (b) methods.

It can be appreciated the difference between the results of the two colorimetric techniques by the absorbance spectra. The DAMO method (Fig. A.6a) seems to be interfered by a second peak at ≈480 nm (probably given by residual nitrite/nitrate, and subsequent chromogen formation), while the modified DAMO technique (A.6b) retrieves higher and clear absorbance spectra. Following these results, the FE for urea production can be calculated, and are reported in Fig. A.7.
Although promising, the FEs and urea concentrations are not validated with urease

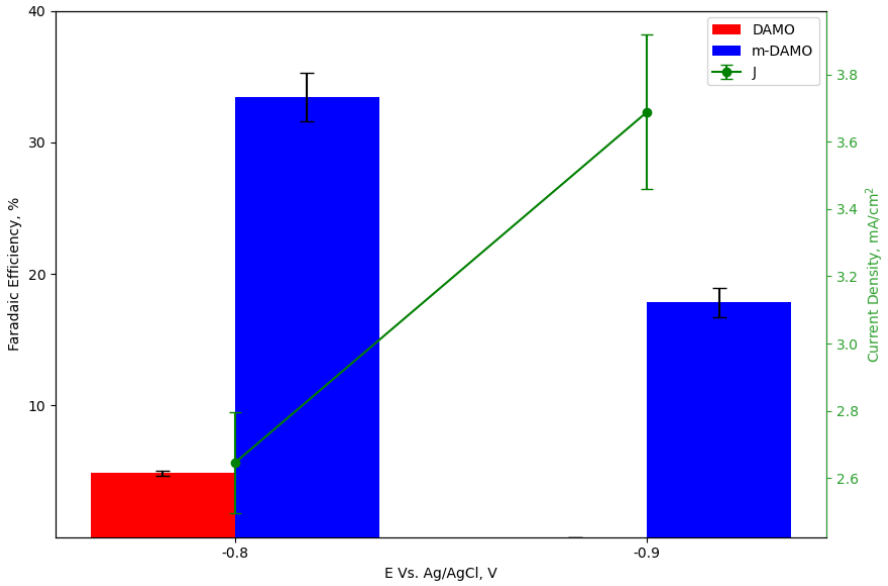

Fig. A.7 FEs for urea production with DAMO and modified DAMO techniques, along with the current density retrieved for a commercial Cu foil.

and NMR technique results, both giving small and undetectable traces of urea in the sample. In this case, the detections are most certainly caused by false positives due to interferents rather than real urea [189–191]. First, even tiny amounts of nitrite or nitrate (left over after the acid pretreatment) can react under the hot, acidic DAMO conditions to form colored chromogens, and the sulfamic-acid step in m-DAMO isn't perfectly efficient at removing nitrite at sub-ppm levels. Second, any ammonia produced on the copper surface can also undergo condensation reactions (though less efficiently than urea) when thiosemicarbazide is present, adding to the apparent urea signal. Third, small carbonyl-bearing molecules such as glyoxal or formaldehyde (common partial CO_2-reduction by-products) can form their own colored adducts with diacetyl monoxime or thiosemicarbazide under acidic, heated conditions. Finally, dissolved copper ions leached into the assay mix [192] can catalyze additional oxidative condensations of these reagents with non-urea substrates, further boosting background color even though no urea is present.

A.0.7 Urea production on silver nanoparticles

Once stated that urease method is the most reliable, it has been applied to understand the performance of silver nanoparticles for urea production: the results are depicted

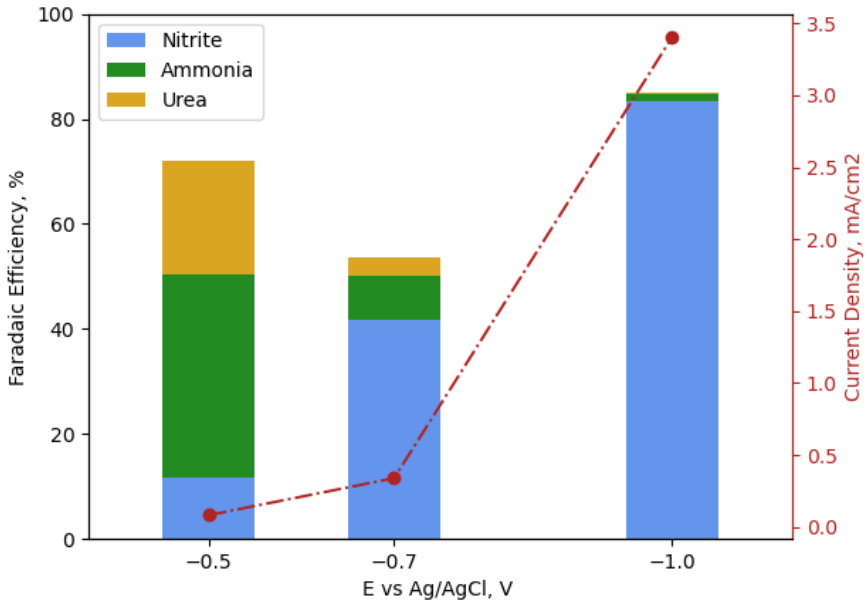

Fig. A.8 FEs for urea production with urease decomposition technique, along with the current density retrieved with Ag NPs catalyst.

in Fig. A.8.

Under Ag-NP catalysis in 0.1 M $KHCO_3$ + 0.1 M KNO_3 saturated with CO_2, the distribution of products shifts dramatically as the applied potential is made more negative. At –0.50 V vs. Ag/AgCl, ammonia is the dominant nitrogen product (FE ≈ 38.6 %), urea formation is significant (FE ≈21.5 %), and nitrite accounts for only ≈11.8 % of the charge. This potential window appears to balance the kinetics of two-electron reduction to NH_3 with the more complex multi-electron, C–N coupling pathway required for urea synthesis, while keeping hydrogen evolution relatively moderate. When the potential is stepped to –0.70 V, the FE for nitrite rises sharply to ≈ 41.8 %, ammonia drops to ≈ 8.2 %, and urea falls to ≈ 3.5 %, indicating that deeper reduction of nitrate to nitrite becomes kinetically favored at higher overpotential whereas further reduction steps lag behind. At –1.00 V, nitrite formation overwhelms all other paths (FE ≈ 83.5 %), urea formation collapses below 0.5 %, and ammonia is nearly extinguished (FE ≈ 1.2 %), reflecting the dominance of simple two-electron processes and rapid hydrogen evolution under strong cathodic bias.

These results illustrate that urea electrosynthesis on silver nanoparticles is only viable

within a narrow overpotential regime. Increasing the applied potential accelerates overall current density (from 0.083 to 3.40 mA/cm^2) and drives vigorous hydrogen evolution, which both lowers the local pH at the electrode surface and competes for surface adsorption sites, thereby suppressing the delicate sequence of steps needed for C–N bond formation. Meanwhile, partial reduction of nitrate to nitrite becomes increasingly facile, leading to its accumulation and further diverting charge away from urea. For practical applications, these findings suggest that one must carefully optimize the operating potential (staying near –0.50 V vs. Ag/AgCl) to maximize urea selectivity, and consider strategies such as mass-transport control of nitrate, catalyst surface modifiers to inhibit hydrogen evolution, or pulsed-potential schemes to preserve active sites for C–N coupling. In summary, the competitive kinetics of hydrogen evolution, nitrite formation, and multi-electron C–N coupling dictate that only a narrow window of cathodic bias supports efficient urea production on Ag nanoparticles in $KHCO_3$/KNO_3 electrolytes.

A.1 Conclusions

In this study, the comparison of colorimetric assays (classic DAMO-TSC and modified M-DAMO-TSC) against structural methods (urease-based enzymatic hydrolysis and NMR spectroscopy) exposed significant inconsistencies. Both DAMO and M-DAMO yielded apparent urea concentrations that were not corroborated by urease assays or NMR, indicating false positives driven by residual nitrite, ammonia, carbonyl by-products, and potential leached Cu catalysis. This underscores the necessity of orthogonal validation (particularly isotopic labeling coupled with NMR or chromatographic-mass spectrometric analysis) to confirm genuine urea production in complex electrolytic matrices. From the catalysis point of view, precise control of the cathodic potential to balance hydrogen evolution, nitrite accumulation, and C-N coupling kinetics must be addressed.

Future work should explore catalyst surface modifications, pulsed-potential operation, and improved mass-transport designs to broaden the effective potential window for urea formation, while standardizing validation approaches (such as isotope labeling with NMR) to establish robust, reproducible benchmarks for urea electrosynthesis.